Linear and non-linear FE-analysis of cracking behavior of wing walls in integral bridges

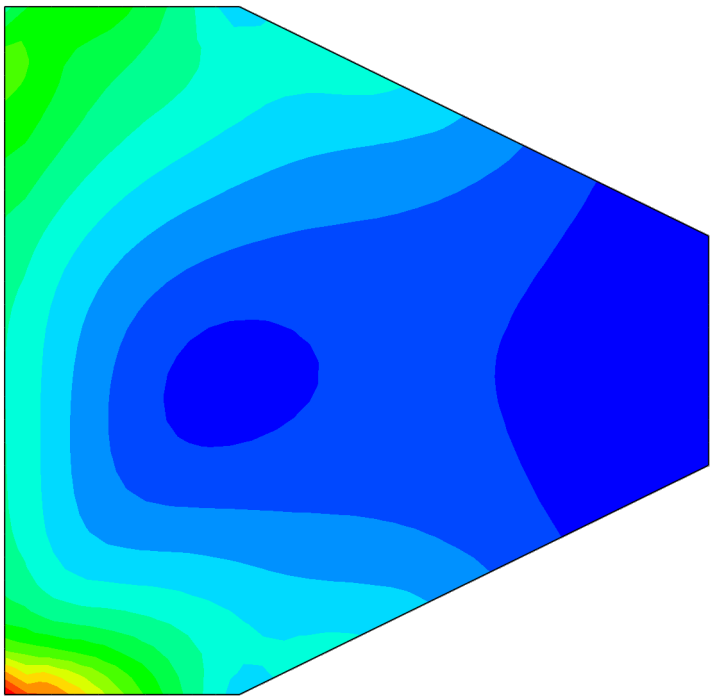

Andreas Ekman och Christoffer Sandin

Avdelningen för Konstruktionsteknik
Lunds Tekniska Högskola
Lunds Universitet, 2018

Avdelningen för Konstruktionsteknik
Lunds Tekniska Högskola
Box 118
221 00 LUND

Division of Structural Engineering
Faculty of Engineering, LTH
P.O. Box 118
S-221 00 LUND
Sweden

Linear and non-linear FE-analysis of cracking behavior of wing walls in integral bridges

Linjär och icke-linjär FE-analys av sprickbildning i vingmurar i plattrambroar

Andreas Ekman & Christoffer Sandin
2018

Rapport TVBK-5266
ISSN 0349-4969
ISRN: LUTVDG/TVBK-18/2566 (98)

Examensarbete
Handledare: Erik Gottsäter (LTH), Henrik Nilsson (ELU Konsult), Christoffer Svedholm (ELU Konsult)
Juni 2018

Abstract

Wing walls on slab frame integral bridges have traditionally been designed for mainly earth pressure and self-weight. It has also been designed separately from the rest of the bridge. Traditionally no 3D effects have been considered in the design of the wing walls.

The Swedish Transport Administration (Trafikverket) have recently introduced regulations stating that 3D effects must be considered when designing wing walls, which means that the wing wall no longer can be designed separately from the rest of the bridge. This leads to an introduction of membrane forces in the wing wall which in turn leads to an increase of the required amount of reinforcement.

This master's thesis investigates the governing parameters that affect the magnitude of these membrane forces and where they arise in the wing wall. A parametric study is conducted where the goal is to present a relationship between the magnitude of the membrane forces and the height and length of the wing wall. This part is analyzed using linear FE modeling. Furthermore, the master's thesis also investigates how the membrane forces affects the crack width in the Service Limit State (SLS) of the wing wall. Wing walls that are designed according to the traditional procedure are analyzed together with applied membrane forces acting on the wing wall.

The cracking behavior of the wing wall is checked for long-term loading with an established non-linear FE model considering bond-slip and crack propagation in reinforced concrete. The model is validated against an experiment of a deep beam and shows sufficient accuracy regarding crack spacing and conservative crack widths for lower loads.

The results from the linear analysis states that membrane forces cause an extra amount of longitudinal reinforcement in the corner of the wing walls. The parametric study indicates a tendency for a higher amount of reinforcement needed due to the membrane forces for smaller wing walls. The parametric study also indicates that for smaller wing walls the membrane forces are of greater importance since they constitute a greater part of the total applied load. For larger wing walls the earth pressure and the self weight gets more dominant and hence the membrane forces constitute for a lesser part of the total applied load.

The result of the non-linear analysis is in some way contradictory. It indicates that the membrane forces for short and low wing walls are of lesser problem in SLS, but for short and high wing walls the membrane forces are of higher importance. The opposite was found in the linear design.

Sammanfattning

Vingmurar på plattrambroar har traditionellt sett dimensionerats för mestadels jordtryck och egenvikt. De har också dimensionerats separat från resten av bron. Traditionellt sett har inga 3D-effekter beaktats vid dimensionering av vingmurar.

Trafikverket har nyligen introducerat regler som fastslår att 3D-effekter ska beaktas vid dimensionering av vingmurar, vilket betyder att vingmuren inte längre kan betraktas som separat från resten av bron. Detta leder till en uppkomst av membrankrafter i vingmuren vilket i sin tur leder till en ökad mängd armering.

Detta examensarbete undersöker de styrande parametrar som påverkar storleken på membrankrafterna och var i vingmuren de uppstår. En parameterstudie är utförd vars mål är att beskriva ett samband mellan storleken på membrankrafterna samt höjden och längden på vingmuren. Detta är gjort med linjär FE-modellering. Vidare ämnar sig examensarbetet också att utvärdera hur membrankrafterna påverkar sprickvidderna i bruksgränstillståndet. Vingmurar som är dimensionerade enligt det traditionella sättet analyseras tillsammans med pålagda membrankrafter.

Sprickbeteendet i vingmuren är kontrollerad för långtidslast med en FE-modell som beaktar bond-slip och sprickbildning i armerad betong. Modellen är validerad mot ett experiment med en hög balk och visar en tillräcklig noggrannhet för sprickavstånd samt sprickvidder som är på säkra sidan för låga laster.

Det konstateras att membrankrafterna leder till ökad horisontell armering främst i hörnen på vingmurarna. Parameterstudien indikerar på att det finns tendenser för ökad mängd armering orsakad av membrankrafterna i mindre vingmurar. Parameterstudien indikerar också att för mindre vingmurar så är membrankrafterna viktigare då det utgör en stor del av den totala pålagda lasten. För större vingmurar är jordtrycket och egenvikten mer dominant och därav utgör membrankrafterna en mindre del av den totalt pålagda lasten.

Resultaten från den icke-linjära analysen är i viss mån motsägelsefulla. Det indikeras att membrankrafterna för korta och låga vingmurar är ett mindre problem i bruksgränstillståndet, men för korta och höga vingmurarna utgör det ett större problem. Motsatt resultat konstaterades i den linjära analysen.

Preface

This master's thesis has been carried out during the spring 2018 as a cooperation between the Division of Structural Engineering at Lund's Faculty of Engineering, LTH, and ELU Konsult AB. The master's thesis comprises 30 credits (ECTS) and accomplishes the five year studies for the Master of Science in civil engineering. Most of the work has been done at ELU Konsult's office in Malmö.

We would like to sincerely thank our supervisor Henrik Nilsson at ELU Konsult, for his useful guidance and patience during the entire work. We are also grateful to have had Christoffer Svedholm as supervisor, with his expertise and dedication for the thesis. Finally, we are thankful for the valuable comments on the report from our supervisor at LTH, Erik Gottsäter.

We appreciate the initiative to this master's thesis from ELU Konsult and the opportunity to write this thesis at their office in Malmö, where the colleagues at the office made the time very joyful.

Lund, June 2018

Andreas Ekman & Christoffer Sandin

Contents

List of Figures

List of Tables

Notations

Roman letters

A	Area of cross section	m^2
A_s	Area of reinforcement bar	m^2
c_{nom}	Nominal concrete cover	m
E_s	Young's modulus for steel	Pa
E_c	Young's modulus for concrete	Pa
F	Force	N
f_t	Tensile strength	Pa
f_{yk}	Characteristic yield stress	Pa
G_f	Fracture energy	J
L	Length	m
$l_{t,max}$	Maximal transmission length	m
N	Normal force	N
s	Bond slip	m
w	Width	m
w_c	Crack width	m

Greek letters

ε	Strain	$-$
μ	Viscosity	m^2/s
ν	Poissons' ratio	$-$
ρ	Density	kg/m^3
σ	Stress	Pa
τ	Shear stress	Pa
ϕ	Diameter	m
ψ	Dilation angle	$-$

Abbreviations

FE	**F**inite **E**lement
FEA	**F**inite **E**lement **A**nalysis
2D	**2D**imensional
3D	**3D**imensional
SLS	**S**erviceability **L**imit **S**tate
CDPM	**C**oncrete **D**amaged **P**lasticity **M**odel
SF	**S**ection **F**orce
SM	**S**ection **M**oment

1 Introduction

Bridges are mainly built for carrying traffic and other loads across a hindrance and are often optimized for its load bearing function. Therefore, it is relevant from an economical and sustainable perspective to find an effective design procedure which also minimizes the material usage. This thesis is focusing on the cracking behavior of wing walls in integral bridges and the design due to 3D effects.

In this chapter the background to the problem is presented along with the objectives of this master's thesis. The scope and limitations are described and lastly the method of this thesis is explained.

1.1 Background

An integral bridge or slab frame bridge is the most common bridge type in Sweden, especially for shorter spans up to 25 m with reinforced concrete (Trafikverket, 2008). A typical single-span slab frame bridge is shown in Figure 1.1. The wing walls can either be parallel to the bridge's length or have some rotation outwards.

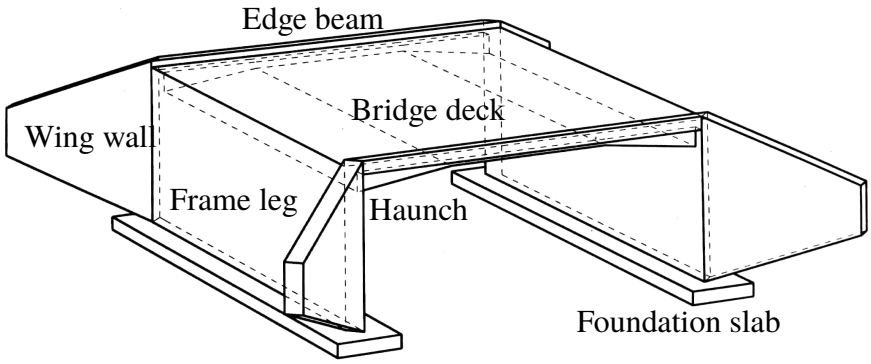

Figure 1.1: Typical single-span slab frame bridge. Reproduction from Sundquist (2008).

The purpose of the wing walls is to overcome the difference in level from the ground surface to the top surface of the embankment. This leads to earth pressure acting on the wing walls and is the main load for the design of wing walls. Traditionally the wing walls and the rest of the frame bridge are treated separate from each other. The wing walls are then designed for the loads acting on only the wing wall, e.g. earth pressure, surcharge and self weight.

The wing walls are normally continuously fixed in the abutments of the concrete frame bridge. This is also the case for the reinforcement, which is also continuous over the joint between the wing wall and the frame leg. The extra stiffness to the frame leg provided by the wing wall has been studied by Myrefelt and Roswall (1994), who concluded that the stiffness effect is local and mainly affects the frame corner and the edge towards the wing wall. This means that the wing walls will be affected by the loads acting on the rest of the bridge. The biggest effect is seen for wing walls constructed perpendicular to the frame leg (Myrefelt and Roswall, 1994).

The regulations concerning bridges and road constructions is in Sweden handled by the Swedish transport administration (Trafikverket). They have recently made the regulations stricter and now require that all new constructed bridges should take 3D-effects into consideration with finite element (FE) models. The wing walls and the rest of the frame bridge should not be treated separately as in the traditional design. This has the consequence that the deformation of the bridge deck and frame leg, which will deform the wing wall, leads to formation of membrane forces in the wing walls' planes. These membrane forces originating from the deformation of the wing wall have not been considered earlier when designing the wing wall separately. Since this thesis' focus is on cracking behavior, long term loads are considered. These loads in the serviceability limit state (SLS), which deform the frame leg and thereby the wing walls, are self weight and surfacing on the bridge deck, shrinkage for the whole bridge, uniform and uneven temperature differences, support yielding and also earth pressure, residual earth pressure and overburden on the frame legs.

For linear design of the wing walls, a model with the 3D-effects leads to a high amount of reinforcement. This amount is considerably higher than that found for the 2D-design, where the membrane forces are omitted. The linear design does not consider that the stiffness of the concrete decreases when cracking occurs and hence the wing walls will take less force.

The purpose of this thesis is to investigate the higher amount of reinforcement for design procedure when 3D effects are considered and find a relationship between the geometry of the wing wall and the increased amount of reinforcement that is required. The purpose of this thesis is also to investigate the crack propagation in wing walls when 3D-effects are considered. This is done with nonlinear FE.

1.2 Objective

The main objective for this thesis is to investigate the reason for the increased reinforcement in the corners of wing walls when designing using linear models. In order to reach this main objective, a number of sub-objectives have to be achieved.

The sub-objectives of the thesis can be summarized in the following:

- What is the relationship between the geometry of the wing walls and the magnitude and distribution of the required amount of reinforcement that the membrane forces generate?
- When is it relevant to include the membrane forces in the design procedure?
- How does crack propagation behave in a FE model?
- In what way is the reinforcement interacting with the concrete while it cracks and how is this considered in the FE model?
- In what way is the crack propagation affected by the geometry of the wing walls?

1.3 Scope & limitations

The scope of this thesis is limited to single-span integral bridges of reinforced concrete. The analysis is limited to the serviceability limit state, where only long-term loads will be considered. The study covers different heights and lengths of the wing wall for one integral bridge with an angle of 45 degrees between the extension of the frame leg's plane to the wing wall's plane. Both a linear design and a non-linear finite element analysis (FEA) is performed. Also, the implementation of the non-linear FEA is within the thesis' scope.

1.4 Method

To give a better understanding of the problem, a literature review is made for the cracking behavior of concrete, interaction between reinforcement and concrete and how to model this with nonlinear FEA.

The FEA is done with Brigade/Plus, which is a FEA software for bridge design from Scanscot Technology AB in Lund and uses Abaqus FEA solver from Simulia. A 3D model is used for the global analysis of the slab frame bridge together with linear elastic theory to obtain the actions on the wing walls. The wing walls are then designed according to the European standard, Eurocode (CEN, 2004), with the Swedish national annex, TRVFS 2011:12, from Trafikverket (2011a).

The wing walls are designed for two cases. One case where only earth pressure is considered and one with all loads including membrane forces. A comparison is then made between the cases. Then a nonlinear analysis for the cracking behavior is performed. The nonlinear model considers the interaction between concrete and reinforcement and also the behavior when cracks propagate in the concrete. From the comparison of the different linear models a recommendation for the design procedure is proposed.

Different geometries of the slab frame bridge and the wing walls are analyzed. In order to get reasonable dimensions and load cases, values and dimensions from an already built bridge, shown in Appendix A, will be used.

1.5 Outline of the thesis

Chapter 2 is the outcome from the literature study, answering the sub-objectives concerning cracking behavior in reinforced concrete. Chapter 3 describes how the theory is implemented in a non-linear FEA. In Chapter 4 the verification process of the FE model is described. Chapter 5 presents the parametric study regarding the wing walls. Chapter 6 presents the results from the parametric study along with some comments to the result. The chapter includes the results from the linear and non-linear FE analysis. In Chapter 7 the discussion is presented with comments regarding potential improvements in the FE model and the parametric study. Lastly, Chapter 8 presents the conclusions and the final remarks. The chapter also presents further studies.

2 Theory

2.1 Material behavior

In this section the material properties of concrete and steel are described. The focus of this chapter is to give a basic understanding of the concrete and steel material behavior and what is relevant for the implementation in numerical calculations.

2.1.1 Concrete

Concrete is a widely used material in the constructing sector. Its good properties regarding compression and its beneficial price per weight makes it a popular material.

Tension

When brittle materials such as concrete are subjected to a displacement controlled tensile test, micro-cracks start to occur. This happens before the stress, σ, in the concrete has reached the tensile strength, f_t, see b) in Figure 2.1. At this stage the micro cracks have not been localized but are spread over the entire specimen. When increasing the displacement so that the stress is equal to the tensile strength, micro-cracks grow in size and number, see c). There is still no traction free crack in the concrete, but the micro-cracks start to localize within a region called the fracture process zone. It is in this zone that the material will undergo non-linear behavior for increased deformation. When increasing the displacement further the concrete starts to strain-soften and the stress starts to decrease. At this stage a traction free crack starts to propagate within the fracture process zone. Increasing the displacement further will cause the traction free crack to grow in width and will finally cause rupture. (Arne Hillerborg, 1983)

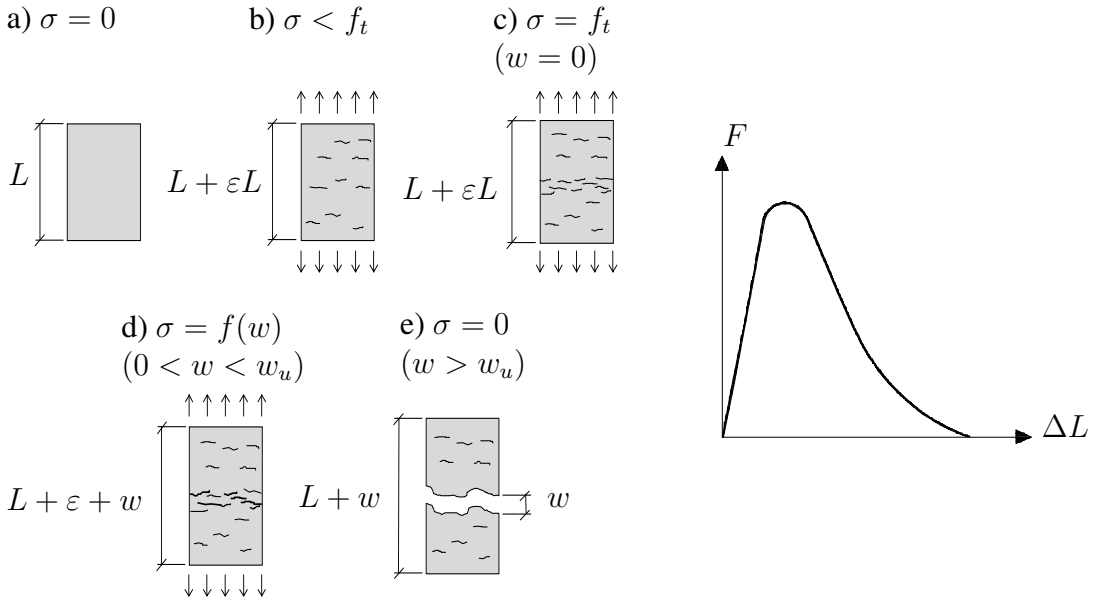

FIGURE 2.1: Response under uniaxial tension for concrete. Reproduction from Björnström, Ekström, and Hassanzadeh (2006).

Compression

When concrete is subjected to compression, strain hardening will occur. This is a fundamental difference to when concrete is subjected to tension and the occurrence of strain softening. At compression concrete behaves linearly up to approximately 30 % of its total strength and thereafter it behaves non-linear. After this point the curve increases up to approximately 70-90 % of the ultimate compressive strain. After the peak value of the compressive strength, the curve starts to descend and there, strain softening occurs. (Bangash, 2001)

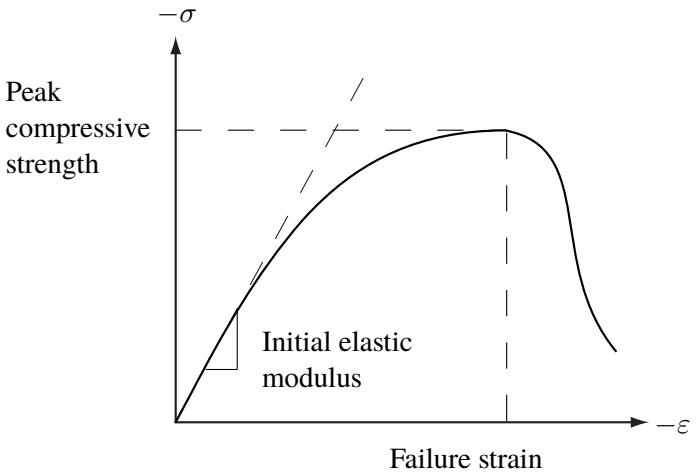

FIGURE 2.2: Response under uniaxial compression for concrete. Reproduction from Bangash (2001).

Biaxial stress

There is a difference in the behavior of concrete subjected to uniaxial and biaxial stresses. In Figure 2.3 the failure envelope is illustrated with the principal stresses, σ_1 and σ_2 on the axis. Tensile cracking will occur in the first, second and fourth quadrant while the third quadrant will be subjected to crushing. It can be seen, that the strength at equal biaxial compression is increased by approximately 16 % and for $\sigma_1 = 0.5\sigma_2$ it is increased by almost 25 %. On the other hand, lateral compressive stress decreases the tensile strength. (Malm, 2006)

The definition of the yield surface originates from the biaxial stress states and will be discussed later in the thesis.

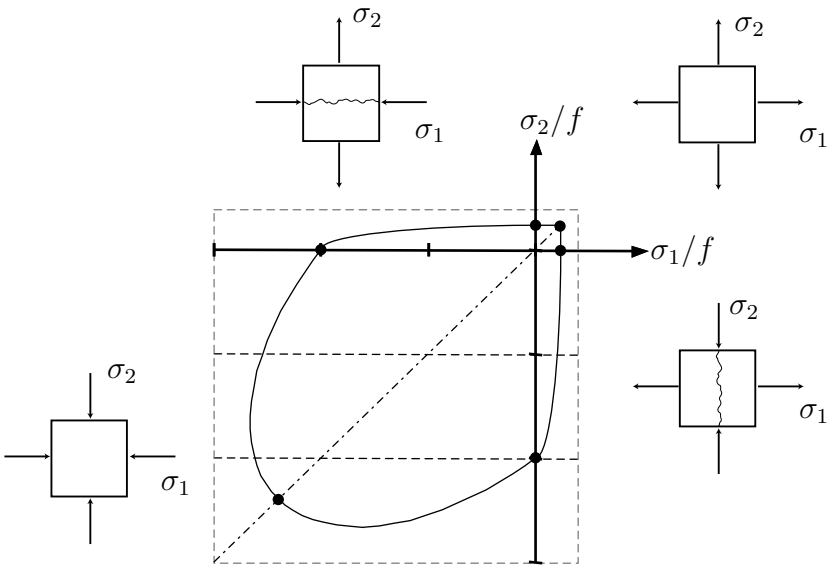

FIGURE 2.3: Biaxial plane stress strength. From Malm (2006).

2.1.2 Reinforcement

Concrete is most often reinforced to compensate for its limited tensile capacity. The reinforcement is often conventional steel bars, but alternative approaches are prestressing and fiber reinforcement. Ribbed hot-rolled bars are one of the most common types in Sweden and denoted B500B-T with a characteristic yield strength of $f_{yk} = 500$ MPa and with a stress-strain relation similar to the one shown in Figure 2.4.

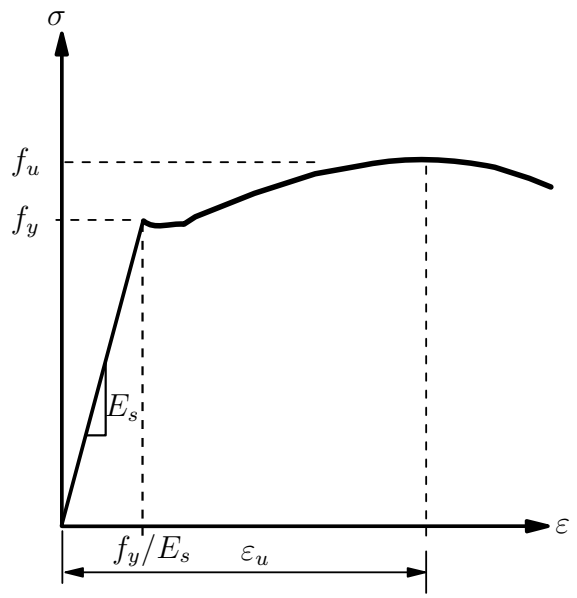

FIGURE 2.4: Illustration of stress-strain relation for hot-rolled reinforcing steel bar in tension.

2.2 Interaction

This section describes the behavior of reinforced concrete with focus on effects from crack propagation. First the cracking process for reinforced concrete is described and then the two important phenomena, tension stiffening and bond slip, are described in detail.

2.2.1 Cracking process of reinforced concrete

When studying the cracking process, tensile tests of prismatic reinforced concrete specimens are often used for understanding the process. This has been well described by Engström (2011) and Figure 2.5 shows a typical example of the cracking process with concrete stresses for increasing load. The relevant remarks from Engström (2011) are presented in this section.

For this member the ends of the bar are loaded, and the bar tends to elongate in relation to the surrounding concrete. The intended relative elongation or slip is prevented by bond at the interface which transfers force from the reinforcement to the concrete. The transfer of force and the associated bond stress is present within a transmission length l_t close to ends, where the steel stress decreases and the concrete stress increases. According to a bond stress - slip relation described in section 2.2.3 the bond stress is associated with a certain slip in the cross section.

The transmission length is dependent on the stress in the steel caused by the load and increases for increased load. But when the tensile strength is reached in the concrete, the load can not increase further without crack formation. The first crack then appears somewhere in the

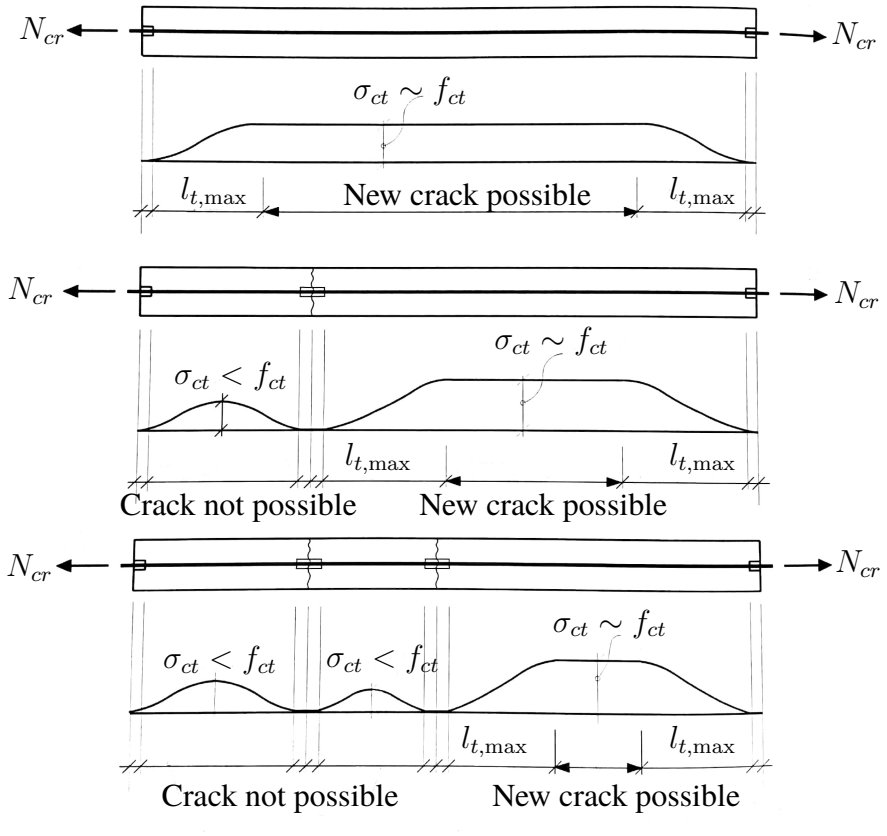

FIGURE 2.5: Example of cracking process for thin reinforced concrete member in tension with increasing load, reproduction from Engström (2011).

mid-region between two transmission lengths. Tensile stresses are at the crack only carried by the reinforcement and new transmission zones develop on each side of the crack and bond transfer force to the concrete. At a critical distance away from the first crack enough force has been transferred to the concrete and a new crack can occur where the tensile strength is reached. New cracks can form until all crack spacings are smaller than two transmission lengths and the fully developed crack formation is reached and the maximum extension of the transmission length $l_{t,max}$ is found.

For members in pure tension there could in theory occur several cracks without an increased load, but since the strength of the concrete in practice varies slightly in the member, a small increase of the load is necessary. The crack width is determined by the relative elongation of the reinforcement bar over $l_{t,max}$ on each side of the crack. Since an elongation requires increased stress in the bar, i.e. an increased load, the width of the cracks will not extend until the maximum number of cracks are reached.

In the above reasoning the cracking process is restricted to thin members, where the transmission length is significantly greater than the width and the concrete stress at the end of the transmission length could therefore be assumed to be uniformly distributed over the cross

section. For thicker members the stress in the concrete is uniformly distributed at a distance away from the end of the transmission zone. This leads to a discontinuity region where the contributing parts of the concrete regarding crack formation is limited. In this region the tensile strength of the concrete is reached for the smaller highly stressed part around the bar, referred to as the effective area. In this area another crack is initiated. For boundary conditions where the tensile stress is applied uniformly distributed to the concrete, the first crack would in theory be a through crack as opposed to the subsequent cracks, which only propagates in the effective area. An example of a typical cracking process for thick reinforced concrete members is shown in Figure 2.6.

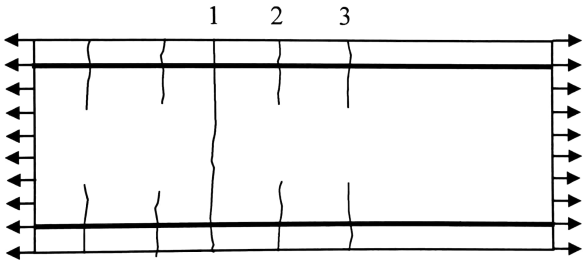

FIGURE 2.6: Example of cracking process for thick reinforced concrete member from Engström (2011).

2.2.2 Tension stiffening

When cracks are initiated in a reinforced concrete member, the force that the structure can carry at a certain displacement is reduced. This can be seen as a stiffness reduction of the member and the stiffness reduces for every crack. When the cracking is stabilized, the stiffness is close to the stiffness of the reinforcement bar only. The occurring difference from the stiffness of the reinforcement bar only and the stiffness of a cracked section is due to that the concrete between the cracks is carrying tensile forces from the bond. This effect is called tension stiffening and is shown in Figure 2.7.

As could be seen in Figure 2.7 the effect is as largest just after the crack initiation and is therefore of more significance for service loads than for ultimate loads. The effect is time dependent and decreasing for sustained loading (Ian Gilbert, 2007), which could be described by creep in the concrete in combination with shrinkage cracks. These effects should be accounted for in long-term calculations.

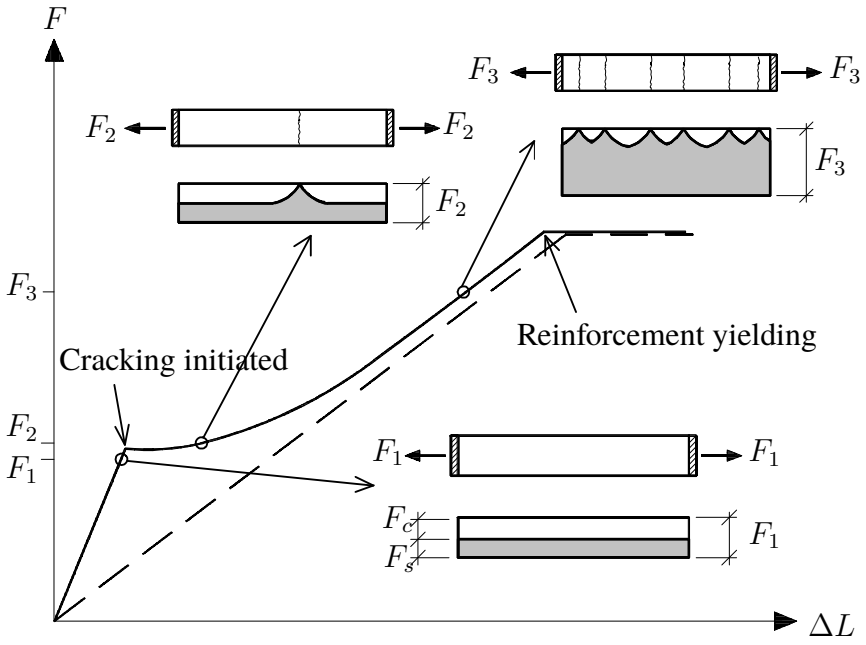

Figure 2.7: Effect of tension stiffening on load-displacement response for reinforced concrete under tension loading. Reproduction from Plos (1996).

2.2.3 Bond stress - slip relation

The presence of bond between concrete and reinforcement is essential to get a composite behavior where the materials carry load together. The bond is affecting the flexural, shear and torsional load bearing capacity of reinforced concrete structures, especially in the serviceability limit state where the tension stiffening effect is evaluated directly in the analysis when bond slip is considered (Balazs and Borosnyói, 2003).

The bond effect is more pronounced at the end anchorage and the surrounding area close to cracks, where bond stresses arise from the strain difference along the length of the reinforcement bar. In regions with negligible force transfer between concrete and reinforcement, perfect bond with complete compatibility of strains is usually assumed as a simplification. But close to cracks this compatibility of strain is not realistic and relative displacements between concrete and steel is required, hence bond-slip is introduced. (Kwak and Filippou, 1990).

The bond performance is divided into three phases for deformed bars with ribs; chemical adhesion between the cement paste and rebar, mechanical interlock between lugs and friction from dislodged sand particles. Here the mechanical bearing is the main part of the bond resistance for deformed bars. The mechanisms of the bond behavior at different slip values is shown Figure 2.8.

Rehm (1961) and Lutz (1970) studied bond slip and described that for low bond stresses adhesion is present, but soon the stresses will either crush the concrete in front of the ribs

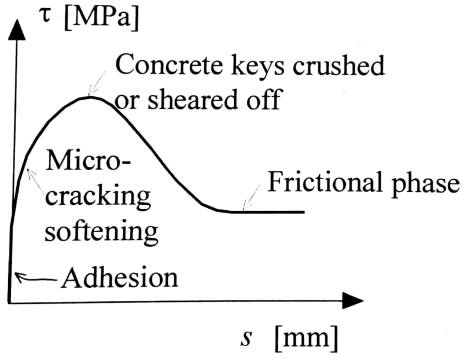

FIGURE 2.8: The different types of bond mechanisms in the bond stress-slip relation. Reproduction from Engström (2011).

or split the concrete by wedging action and initiate slip. The slip will disrupt the surface adhesion and mobilize mechanical interlock and friction forces on the ribs. The normal and shear forces on the rebar surface from the reinforcement ribs and roughness radiate to the surrounding concrete and causes corresponding inclined principle stress in tension and compression. For increased bond stresses the tensile stresses approach the tensile strength and eventually inclined internal bond cracks occur. For higher bond stresses different failure mechanisms occur; splitting failure, splitting induced pull out failure and pull out failure due to concrete keys sheared off (FEB, 2000). The bond capacity differs for the different failures and is highest for pull out failure, which therefore is the aim to achieve.

The bond stresses vary with the length of the reinforcement and at a given position a local bond stress-slip relation is of interest to find. This has in the past been studied experimentally in pull-out tests where the reinforcement is embedded over a short distance about $l_b = 3\phi$. The bond stress is then approximately uniformly distributed over the embedment length. A test set-up for the pull-out test is shown in Figure 2.9.

The bond stress is calculated as:

$$\tau = N/(\pi\phi l_b) \tag{2.1}$$

The slip, s, is calculated as the measured displacement between reinforcement and the end face of the concrete. An idealized relation can be suggested based on different experiments. One suggested model is found in Model Code 10 (2012) and shown in Figure 2.10.

The ascending branch of the curve is in the model described by Eqn. 2.2.

$$\tau_b(s) = \tau_b max(s/s_1)^\alpha \tag{2.2}$$

The three different slip values, s_1, s_2 and s_3 depend on the bond conditions and which failure that is present, while the maximum bond slip, τ_{max}, depends on the concrete compressive

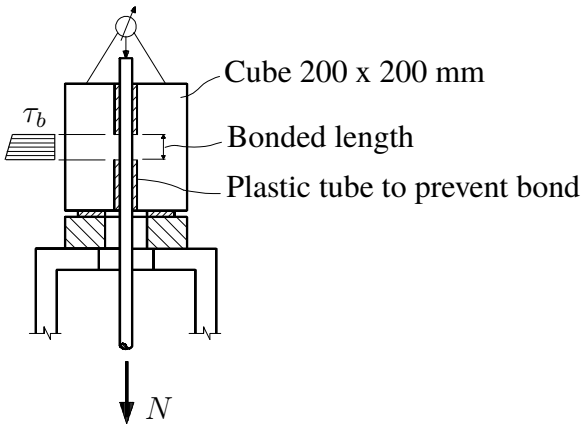

FIGURE 2.9: Example of pull-out test with short embedment length. Reproduction from Engström (2011).

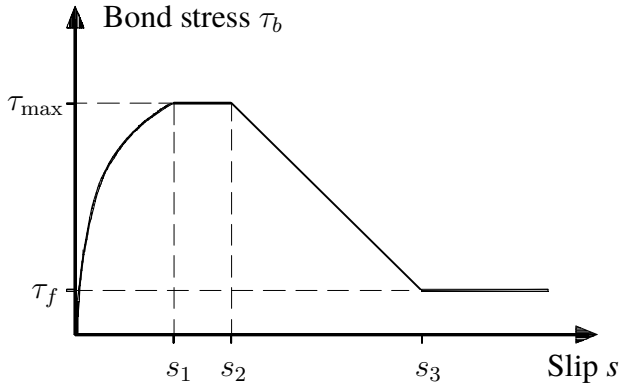

FIGURE 2.10: Model for bond-slip relation according to Model Code 10 (2012).

strength. Values and equations are found in Model Code 10 (2012) for the different bond conditions.

2.3 Non-linear constitutive model

In this section fundamental theory of plasticity and fracture mechanics are described with focus on concrete and how it is implemented in the FE-model. First the concept of fracture mechanics and crack models are described and then the fundamentals of plasticity theory used in the concrete damaged plasticity model explained.

2.3.1 Fracture mechanics

The cracking in concrete is fundamentally different from metals where the cracking in metals is proceeded by yielding, where it in concrete is proceeded by micro cracking. It is also assumed for metals that the stress within the fracture process zone is increasing or remaining constant at increasing load. This is not true for concrete where the stress decreases for increasing load - called tension softening. (Arne Hillerborg, 1983)

In general, fracture in concrete is characterized by three properties, fracture energy G_f, tensile strength f_t and the shape of the $\sigma - w$ curve in Figure 2.11, where w is the crack width.

Tension softening

The tension softening response is an important concept in fracture mechanics for concrete. In Figure 2.11 a) the stress-deformation relationship is illustrated for concrete that undergoes a displacement controlled tension test. The stress increases as the displacement increases until it reaches its peak. After the peak the stress starts to decrease with increasing strain, and this is what is called tension softening.

In Figure 2.11 b) the $(\sigma - \varepsilon)$-relationship is shown. Here has no cracking yet occurred and the response is of linear elastic nature. The strain is evenly distributed over the entire test specimen.

In Figure 2.11 c) the strain softening starts to occur. The strain softening only takes place within the fracture process zone, while the rest of the specimen will contract due to the decrease in stress. Here the displacement is the width of the propagated crack denoted w. Note that this is a displacement in absolute value and not a strain. When the fracture process zone has been developed the stress-deformation properties can not be described by one single curve since the cracking strain will depend on the width of the fracture process zone. Hence the division of the $\sigma - \Delta L$-curve into two curves according to b) and c) in Figure 2.11.

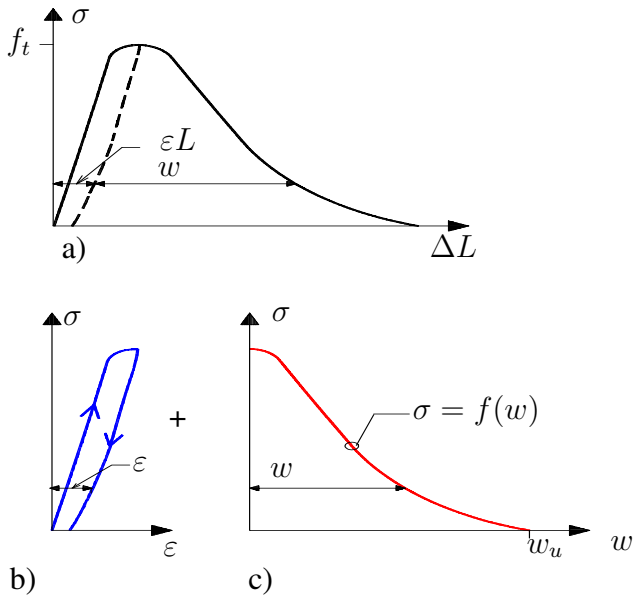

FIGURE 2.11: Division of the deformation properties into $\sigma - \varepsilon$ diagram and a $\sigma - w$ diagram. Reproduction from Arne Hillerborg (1983).

Fracture energy

The total amount of energy absorbed in a specimen during a tensile test is the integral of the stress - deformation curve in Figure 2.11 a). This energy can be divided in two parts corresponding to the integral of the two curves in Figure 2.11 b) and c). The integral of the elastic curve b) corresponds to the elastic energy stored in the whole specimen. The integral of the tension softening curve c) corresponds to the absorbed energy in the fracture process zone. It is this energy that is stored in the fracture process zone that is denoted as the fracture energy G_f. (Arne Hillerborg, 1983)

According to Zhao, Kwon, and Shah (2008) among others the fracture energy depends on the grain-size distribution of aggregate except the strength class of the concrete. The fracture energy can be determined from a standard three-point bending test suggested by RILEM Technical Comittee 50. The fracture energy is between 50-170 N/m and is depending on the grain-size distribution according to Model Code 90. However for Model Code 10 it is independent of grain-size distribution and is calculated as $G_f = 73 \cdot f_{cm}^{0.18}$.

As mentioned above the fracture energy corresponds to the area under the stress-displacement curve. The shape of the curve however can be different for equal fracture energy. Arne Hillerborg (1985) proposed a bilinear function. Later on, Cornelissen, Hordijk, and Reinhardt (1986) developed an exponential approximation which is according to Karihaloo (2003) the most accurate. Both approximations are plotted in Figure 2.12. The exponential function is defined according to Eqn. 2.3 and 2.4

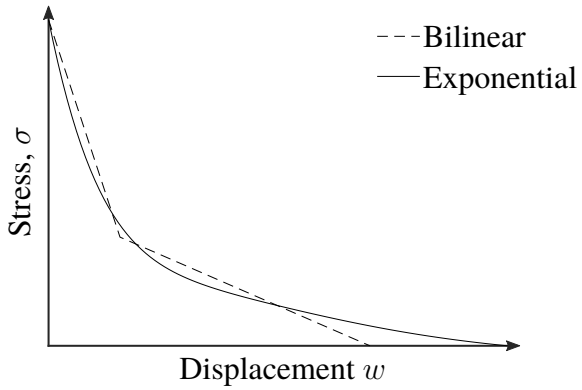

FIGURE 2.12: Bilinear and exponential curves for tension softening.

$$\sigma = \left((w) - \frac{w}{w_c} f(w_c) \right) f_t \tag{2.3}$$

$f(w)$ is the function describing the displacement and is defined accordingly

$$f(w) = \left[1 + \left(\frac{c_1 w}{w_c} \right)^3 \right] exp \left(-\frac{c_2 w}{w_c} \right) \tag{2.4}$$

where,

w is the crack opening displacement
w_c is the crack opening displacement that corresponds to a stress free crack. $w_c = 5.14 G_f / f_t$
c_1 material constant $c_1 = 3.0$ for normal concrete
c_2 material constant $c_2 = 6.93$ for normal concrete

Crack models

Cracks in FEM can be modeled in different ways, where the first discrete crack model was proposed by A. Hillerborg, Modéer, and Petersson (1976) including a fictitious crack. The discrete crack model requires a predefined crack pattern or a continuous mesh adaption, which redefines the topology. It needs separate crack elements, normally springs or interface elements, where the material response is used directly.

Another model is the crack band model proposed by Bažant and Oh (1983) using the widely used smeared crack approach by Rashid (1968). The smeared crack approach is the contrary without special elements and predefined crack locations. Instead all the continuum elements are given a strain-softening constitutive relation covering the tension softening at crack formation. The fact that microcracking in the fracture process zone does not necessarily develop in a narrow discrete region has been an argument for that the tension softening

relation $\sigma(w)$ can equally well be approximated by a strain softening relation $\sigma(\varepsilon)$, i.e. a decreasing stress for increasing inelastic strain (Karihaloo, 2003). Since the relation is a function of strain, the crack deformation w is related to a crack band. The crack band needs to be defined in advance and is for plane concrete and reinforced concrete with bond-slip approximately taken as the element length, $h = l_{elem}$.

The smeared crack approach proposed by Rashid (1968) treats the influence of a crack in an element as a change of the element's behavior from isotropic to orthotropic, with zero stiffness in the direction normal to the crack surface. This concept was broadened by Bažant and Oh (1983), Suidan and Schnobrich (1973), who reinstated the stiffness normal to the crack surface with a negative reduction factor, μ, and a shear retention factor, β, for the shear stiffness. A popular incremental orthotropic law for the smeared crack elements evolved in the 1980s accordingly Eqn. (2.5). (Rots and Blaauwendraad, 1989)

$$\begin{bmatrix} \Delta\sigma_{nn} \\ \Delta\sigma_{tt} \\ \Delta\sigma_{nt} \end{bmatrix} = \begin{bmatrix} \frac{\mu E}{1-v^2\mu} & \frac{v\mu E}{1-v^2\mu} & 0 \\ \frac{v\mu E}{1-v^2\mu} & \frac{\mu E}{1-v^2\mu} & 0 \\ 0 & 0 & \frac{\beta E}{2(1+v)} \end{bmatrix} \begin{bmatrix} \Delta\varepsilon_{nn} \\ \Delta\varepsilon_{tt} \\ \Delta\varepsilon_{nt} \end{bmatrix}, \tag{2.5}$$

where E is the Young's modulus and v is Poisson's ratio.

The smeared crack approach is usually categorized into rotating and fixed smeared crack concepts. The former allows the crack orientation to co-rotate with the principal strain axes, whereas with the fixed concept the crack orientation is fixed during the entire computational process (Rots and Blaauwendraad, 1989).

It is also possible to model the smeared cracked concept in the framework of plasticity theory. This treatment is nowadays often used in commercial FE programs, including Abaqus, and will be described more in the next section and in the section regarding Concrete Damaged Plasticity.

2.3.2 Plasticity theory

As Lubliner et al. (1989) puts it, classical plasticity theory serves as a representation in two ways, either as a translational of the physical reality or an approximation of a behavior under certain circumstances. For ductile crystalline materials such as steel the classical plasticity theory serves well as a translation of the physical reality while for materials such as concrete it does not. However, it has been successfully showed by Chen (1982) and others that plasticity theory works well as an approximation.

The most successful area where plasticity theory describes the concrete behavior is when concrete acts primarily in compression. In problems where at least one of the principal stresses is in tension it is suitable to introduce fracture mechanics to describe the strain softening. Lubliner et al. (1989)

The essential elements in classical plasticity theory is the yield function, the hardening rule and the flow rule which all will be described below.

Yield function

The yield function describes at what stress state yielding occurs. Since the material behaves nonlinear, the yield function is history dependent and change with plastic strains. The constitutive relation is of incremental fashion which means that the current stress or strain state can only be obtained by an integration of the load history. There are numerous yield functions for different materials but the most relevant for frictional materials such as concrete are the Drucker-Prager yield function and the Mohr-Coulomb yield function (Krenk, 2009).

Lubliner et al. (1989) proposed a yield surface which was later improved by Lee and Fenves (1998) to consider for different evolution of strength under tension and compression. This is the model that will further be described in the Chapter 2.3.3.

The direction of the incremental plastic strain is described by the flow rule, which is a partial derivative of a potential function. For concrete the flow rule is non-associated which means that the potential function is different from the yield function. Otherwise for metals the flow rule is associative and hence the potential function is equal to the yield function. von Mises yield criterion is mostly used to describe metals. For concrete the Drucker-Prager yield criterion is most common. The Drucker-Prager will give rise to plastic volume change that is characteristic for friction materials such as concrete (Lee and Fenves, 1998).

Hardening rule

The yield surface changes with plastic strains. The evolution of the yield surface is determined by the hardening rule. The hardening rule is defined by hardening parameters that determines how the yield surface changes its shape, size and position. This paper only treats static conditions which means that there is only isotropic hardening and no translation of the yield surface will occur.

Flow rule

The flow rule determines the incremental direction of plastic strain and can be written as

$$\dot{\varepsilon}^p_{ij} = \dot{\lambda}\frac{\partial g}{\partial \sigma_{ij}}; \quad \dot{\lambda} \geq 0 \tag{2.6}$$

g is a potential function that may or may not be equal to the yield function f. As said above, for non-associative flow rule $g \neq f$ which is typically for frictional materials such as concrete.

The yield function f serves for associated flow as a potential function and hence the direction of the incremental plastic strain is a partial derivate of the yield function.

2.3.3 Concrete damaged plasticity

Concrete can in Brigade be modeled by the provided Concrete Damaged Plasticity Model (CDPM), which is suited for quasi-brittle materials. This constitutive model allows for different yield strengths in tension and compression, and a softening behavior in tension as opposed to compression where initial hardening is followed by a softening. The model is based on proposed models by Lubliner et al. (1989) and Lee and Fenves (1998). This model is advantageous for cyclic and dynamic loading, where a stiffness degradation is available with damage parameters for unloading after crushing or cracking. However the damage parameters are irrelevant for our thesis which focus is on monotonic loading and refer to Lubliner et al. (1989) for more details regarding the CDPM.

Since plane stress is assumed the yield function is described with a yield surface in the $\hat{\sigma_1} - \hat{\sigma_2}$ plane, where the hat denotes principal stresses. The initial yield surface is shown in Figure 2.13. For the complete yield function refer to Lubliner et al. (1989).

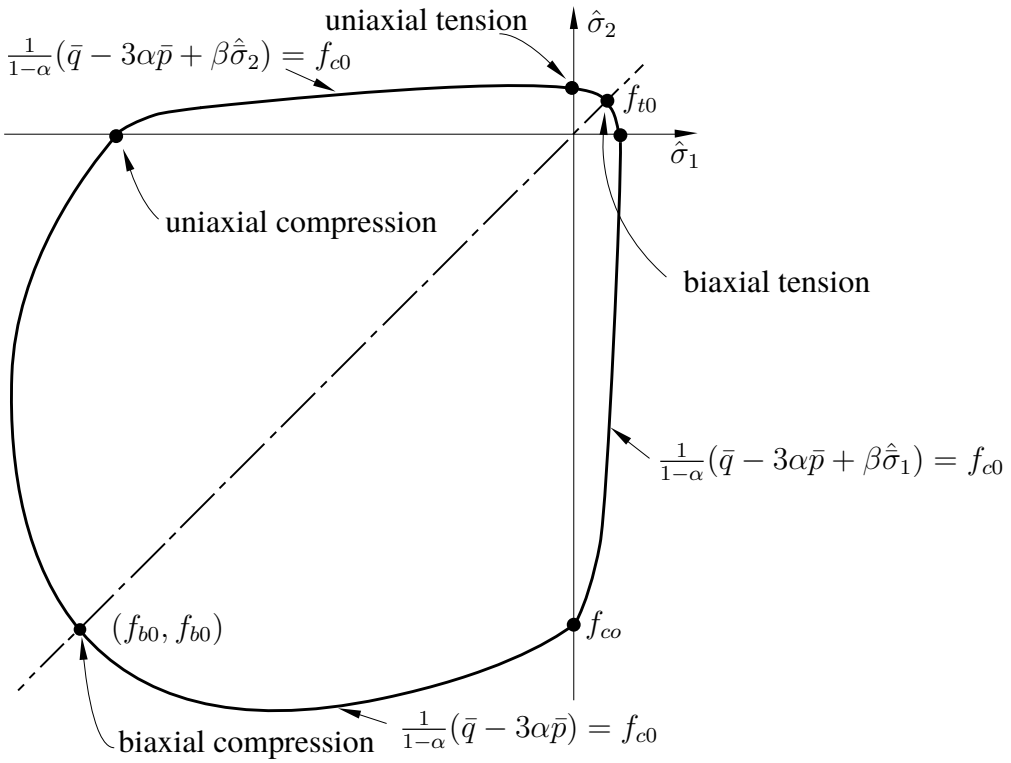

FIGURE 2.13: Yield surface for plane stress conditions in the CDPM. Reproduction from Abaqus (2011).

The parameters in Figure 2.13 are explained in the following.

$\bar{p} = -\frac{1}{3}\bar{\boldsymbol{\sigma}} : \mathbf{I}$, is the effective hydrostatic stress,
$\bar{q} = \sqrt{\frac{3}{2}\bar{\mathbf{S}} : \bar{\mathbf{S}}}$ is the von Mises effective stress, where
$\bar{\mathbf{S}} = \bar{\boldsymbol{\sigma}} + \bar{p}\mathbf{I}$ is the deviatoric part of the effective stress tensor, $\bar{\boldsymbol{\sigma}}$.
$\hat{\bar{\sigma}}_1$, $\hat{\bar{\sigma}}_2$ is the maximum principal stress of $\bar{\boldsymbol{\sigma}}$.

For details regarding stress tensors and stress invariants refer is made to Krenk (2009).

β is a function of the current tensile and compressive cohesion stresses, $\bar{\sigma}_t$ and $\bar{\sigma}_c$, according to

$$\beta(\tilde{\varepsilon}^{pl}) = \frac{\bar{\sigma}_c(\tilde{\varepsilon}_c^{pl})}{\bar{\sigma}_t(\tilde{\varepsilon}_t^{pl})}(1-\alpha) - (1+\alpha) \tag{2.7}$$

α is a material coefficient determined from the initial equibixaxial and uniaxial compressive yield stress, f_{b0} and f_{c0}, as

$$\alpha = \frac{f_{b0}/f_{c0} - 1}{2f_{b0}/f_{c0} - 1} \tag{2.8}$$

The ratio f_{b0}/f_{c0} for experimental values is typically in the range 1.10 to 1.16 yielding α from 0.08 to 0.12 (Lubliner et al., 1989). The default value in the CDPM is 1.16 and used in the analysis.

The CDPM assumes non-associated flow, where the potential function G is the Drücker-Prager hyperbolic function:

$$G = \sqrt{(\varepsilon f_{t0}\tan\psi)^2 + \bar{q}^2} - \bar{p}\tan\psi = 0, \tag{2.9}$$

where ψ is the dilation angle in the meridian plane at high confining pressure and ε the flow potential eccentricity. Both parameters are considered as material coefficients and is determined experimentally. The dilation angle considers the plastic volumetric strain increase for shear loading and will be determined in the verification in section 4. The default value for the eccentricity of 0.1 is used in the analysis and defines the rate at which the plastic potential function approaches the asymptote for higher hydrostatic stress.

The CDPM allows for viscoplastic regularization of the constitutive equations. This helps overcoming the convergence difficulties associated with a softening behavior in implicit analysis. The regularization permits stresses to be outside of the yield surface, but for a small value on the viscosity, μ, the results are not compromised.

3 FE-modelling

This chapter's focus is the implementation of the theory of reinforced concrete in to a finite element analysis. The analysis is done with 2D non-linear material finite elements in Brigade/Plus.

3.1 Non-linear finite element analysis

The finite element method is a numerical solution method used to approximate the solution of boundary value problems for partial differential equations. Elasto-plastic problems are located to these problems and are especially nonlinear. The nonlinear solution procedure can be summarized into: formulation of the nonlinear finite element method, solution of the nonlinear global equations and integration of the constitutive equations. The procedure for solving the global equations will be discussed in more detail and for details regarding the nonlinear FEM formulation and integration of the constitutive relations refer is made to Krenk (2009).

The Abaqus FEA solver allows for several numerical procedures, where the Newton-Raphson scheme is chosen, for solving the global equations. This procedure contains incrementation and iteration. The load is divided into increments and applied stepwise. In each increment the solver iterates until convergence of the solution. The solution in the increment is found when the residual forces, Ψ, is smaller than a limit close to zero. The residual force is found from the difference between the external applied force and the internal forces, and is a function of the displacement, Δ:

$$\Psi(\Delta) = f_{ext} - f_{int}(\Delta) \tag{3.1}$$

The procedure is shown in Figure 3.1. The first state (Δ_n, f_n) is known and for one increment the external force is fixed and known.

The solver can be used with an automatic incrementation, which can decrease and increase the increment within specified limits in order to find a solution or to proceed faster when possible. The limits are user-defined and also an initial increment is defined. The loading is displacement controlled since crack formation can suddenly decrease the applied load, which force controlled loading can not follow. Sudden force decrease oblige the displacement

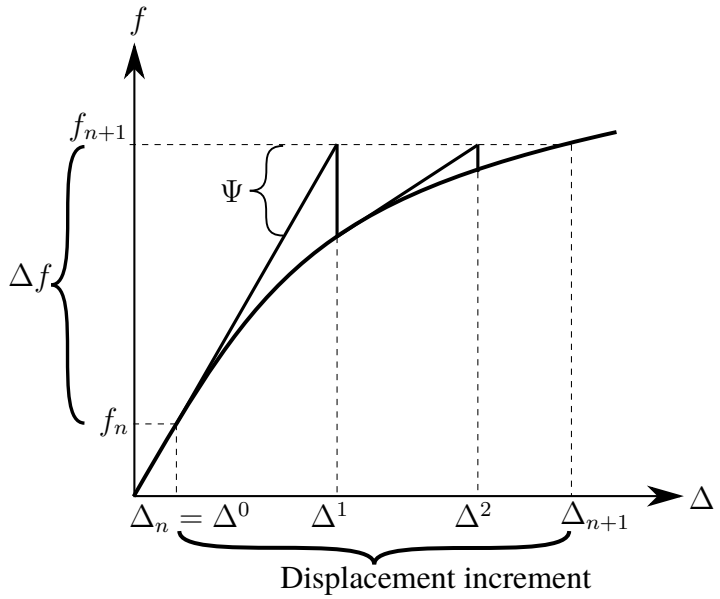

FIGURE 3.1: Illustration of the Newton-Raphson scheme for one-dimensional problem.

increment to be very small in order to find a solution. In the step module in Brigade/Plus the parameters in Table 3.1 are used in the analysis.

TABLE 3.1: Parameters for the step module in Brigade/Plus used in the analysis.

Step: Static, General	
Initial increment	0.001
Minimum increment	10^{-20}
Maximum increment	0.001
Maximum allowed cutbacks, I_A	30

3.2 Concrete modelling

Since the problems are two dimensional with focus on membrane forces the concrete is modeled with 2D plane stress elements. The discretization is done with linear triangle mesh elements, so called CPS3. The parameters and equations used in the analysis are described in this section.

3.2.1 Plasticity

The concrete damaged plasticity model requires values on five material parameters and the stress-strain relations for compression and tension. The material parameters are for some of them put to the default value described in the Chapter 2 and summarized in Table 3.2 and the dilation angle to be determined in the next chapter. The viscosity, μ, is kept small but increased up to 10^-5 when convergence problems occurs.

TABLE 3.2: Material parameters used in the CDPM.

Concrete damaged plasticity		
Parameter	Value	Comment
ε	0.1	Default
f_{b0}/f_{c0}	1.16	Default
K_c	0.667	Default
ψ	-	To be determined
μ	$10^{-5} - 10^{-7}$	Dependent on analysis

3.2.2 Compression

The stress-strain relationship in compression is modeled by the relation given in EC2 according to Eqn. (3.2) and Figure 3.2. The elastic part with an elastic modulus, E_{cm}, is assumed to be up to $0.4f_{cm}$, where irreversible plastic strains form.

$$\frac{\sigma_c}{f_{cm}} = \frac{k\eta - \eta^2}{1 + (k-2)\eta}, \tag{3.2}$$

where

$\eta =$ $\varepsilon_c/\varepsilon_{c1}$
ε_{c1} is the strain at peak stress
$k =$ $1.05E_{cm}|\varepsilon_{c1}|/f_{cm}$

The ultimate compressive strain, ε_{cu1}, is for normal strength concrete 3.5 ‰ ($f_c < 50$ MPa), but the strain at peak stress, ε_{c1}, is dependent on the concrete class, for instance 2.3 ‰ for C40 and the same holds for the Young's modulus, E_{cm} and the mean compressive strength, f_{cm}. The curve is implemented to the program in tabular form with yield stress to plastic strain values and approximated by 20 data points.

3.2.3 Tension

Also the tension softening response is given in tabular form to the program. This is done by giving the yield stress to crack displacement values from (2.3). Since there is a big decrease

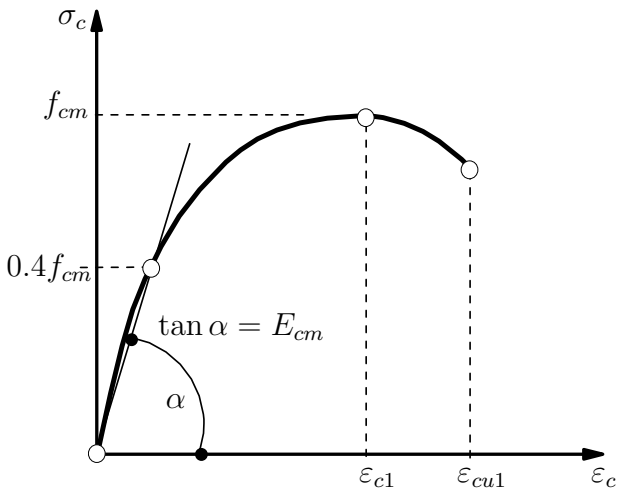

FIGURE 3.2: Stress-strain relation for concrete in compression according to EC2 3.1.5.

in stress directly after cracking the data points are more dense there, according to Figure 3.3. Ten points are used and the program assumes linear relations in between the points. The program then divides the crack displacement with the element length to get the corresponding plastic strain for the constitutive relation.

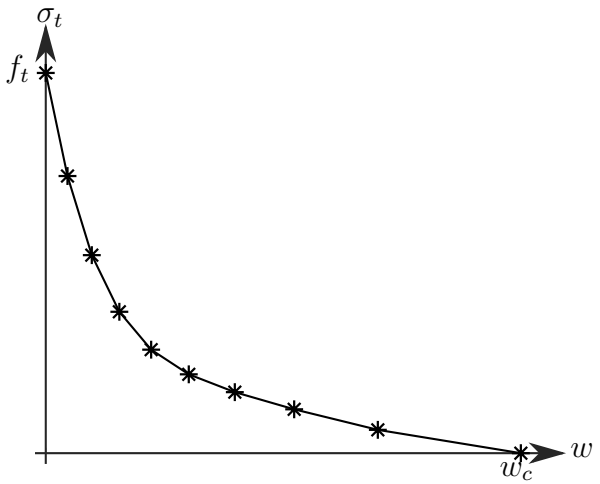

FIGURE 3.3: Input data points for exponential tension softening response for cracking displacement, w, and tensile stress, σ_t. $*$ marks the 10 input points.

3.3 Reinforcement modeling

The reinforcement is modeled separately with linear 2D truss elements (T2D2). An idealized strain curve is used for the plasticity since the main objective is to study the serviceability

state where the reinforcement stays in the elastic region.

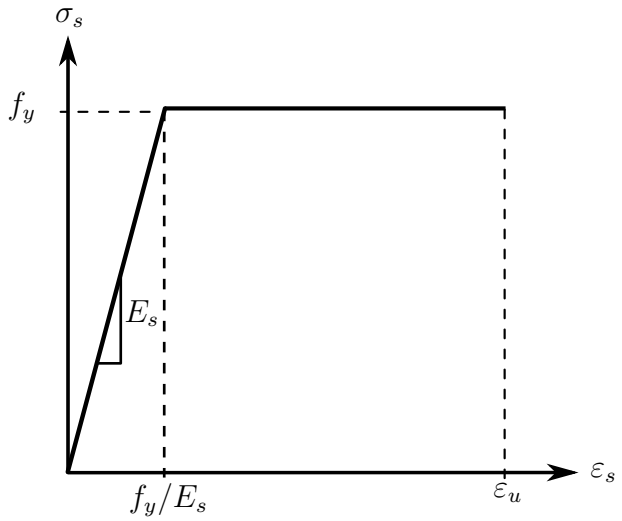

FIGURE 3.4: Stress-strain relation for ideal-plasticity model for reinforcing steel bars.

In Brigade/Plus the properties of the reinforcement are divided into elasticity with Young's modulus, E_s, Possion's ratio, v, and plasticity with the yield stress, f_y, as input.

3.4 Interaction

Since the two materials, concrete and steel, are modeled separately, a connection between them is needed in the model. A proposed connection by Ngo and Scordelis (1967), is the bond link element and is used in the analysis. This connection uses two orthogonal springs which transmit forces between a steel node and the concrete node in one direction per spring. Since the bond-slip is local, the concrete node and the steel node coincide in the finite element mesh of the undeformed structure, i.e. the connection element has no physical dimension.

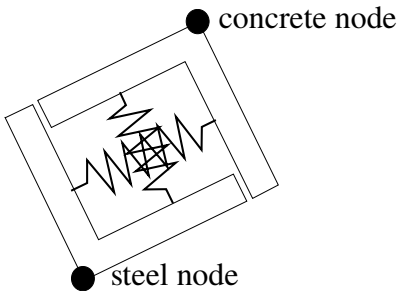

FIGURE 3.5: Bond link element proposed by Ngo and Scordelis (1967) with two orthogonal springs.

The stiffness of the spring orthogonal to the longitudinal reinforcement direction, transmitting the transverse force, is assumed to be very stiff to get a rigid behavior between the concrete and reinforcement. This is modeled by Cartesian connectors in Brigade/Plus with rigid translation, which assumes a stiffness ten times the stiffness of the surrounding material.

The longitudinal spring, which transmits the normal force in the reinforcement, is given the nonlinear bond-slip relation Eqn. (2.2). The relation is transfered to a force - displacement relation instead of shear stress - slip relation. The force is then the integral of shear stresses over the lateral area of the bar between two element nodes, i.e:

$$F_\tau = \int_A \tau_b dA = \pi \phi l_{elem} \tau_b \tag{3.3}$$

The relative displacement of the spring nodes is equal to the slip. The relation is again given in tabular form and is the same for negative respectively positive displacement according to Figure 3.6. Since the shear force varies more for lower slip/displacement, the data point closest to origo is at $s = s_1/10^6$ in order to get a high initial stiffness. The spring is modeled by cartesian connectors in Brigade/Plus.

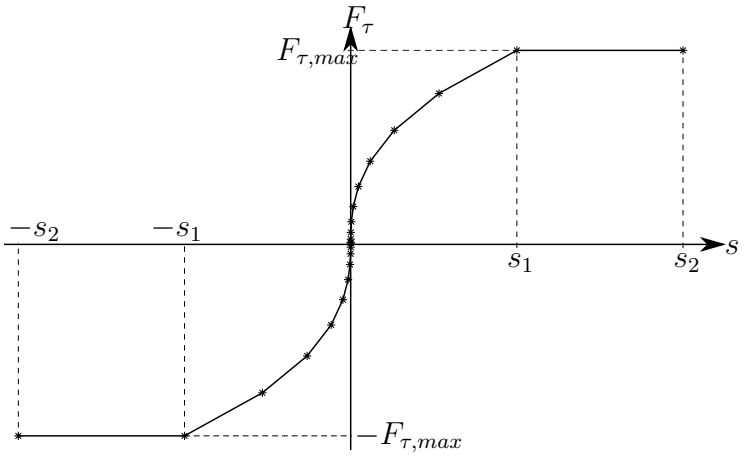

FIGURE 3.6: Force - displacement relation for axial spring according to Model Code 10 for the ascending part. The data points are marked with $*$.

The reinforcement can also be modeled as an embedded region in the concrete. This gives the assumption of perfect bond without slip between the reinforcement and the concrete. In Brigade/Plus is done by adding the extra stiffness from the reinforcement to the stiffness matrix for those concrete elements, where the reinforcement is embedded.

4 Verification of FE model

It is of great importance that the computational model, in this case the FE model, is verified and validated in order to make accurate predictions.

This master's thesis aims to describe behavior of wing walls under plane stress conditions. The computational model, which aims to describe this behavior, is validated against an experiment made by the American Concrete Institute (ACI), which is described in detail in Collins et al. (2015).

The wing wall may be seen as a deep beam with plane stresses. In its use, the wing wall will be loaded with forces normal to its plane, e.g. earth pressure, and forces parallel to its plane, e.g. membrane forces. However, the forces normal to the plane of the wing wall are not the focus of this thesis but rather the plane stresses which originates from the membrane forces. Since the experiment made by ACI describes the behavior of a deep beam, where plane stress is dominant, the experiment is suitable to validate the computational model used in this thesis.

This section describes the experiment made by ACI and the validation process for the computational model, i.e. the FE model. The first section describes the ACI experiment more in detail. The second section describes briefly how the ACI beam is modeled with all the input material parameters. The third section describes the validation of the model where the dilation angle and the fracture energy are validated and calibrated against the ACI experiment.

4.1 ACI Experiment

The experiment aims to predict shear failure in thick slabs. The experiment setup consists of a deep beam shown in Figure 4.1. The beam is reinforced with longitudinal reinforcement in the top and bottom, and with stirrups. The longitudinal reinforcement in the top consists of $3\phi20$ and in the bottom $3\text{x}3\phi30$. The beam is divided into two spans, the west span (7 m) and the east span (12 m). The compressive strength of the concrete was estimated to $f_c = 40$ MPa, and the tensile strength was estimated to $f_t = 2.48$ MPa. From the test's force-displacement curve the Young's modulus was estimated to $E_c = 30$ GPa.

The concrete beam is modeled with a roller support to the west and with a fixed support to the east. It can be noticed from Figure 4.1 that it is only the span to the west that is reinforced with stirrups. The reason for this is that the experiment aims to test two scenarios, one where

the beam is seen as reinforced with stirrups, and the other scenario where the beam is not. The beam will first fail in the east span. After failure the beam will the repaired by strapping the east span with $3\phi30$ Dywidag threadbars and post-tensioning each bar. Then the beam will be loaded again and fail in the west span. However, for simplicity, the validation of this thesis FE model will only focus on the first failure, that is in the east span. In the ACI experiment the stirrups do not cover the entire cross section, i.e. they do not go around but are only one vertical bar. This is also how it is modeled in the non-linear FE model.

The test is displacement controlled and the reading of the force is at the top of the beam between the two spans, marked with a dashed line in Figure 4.1.

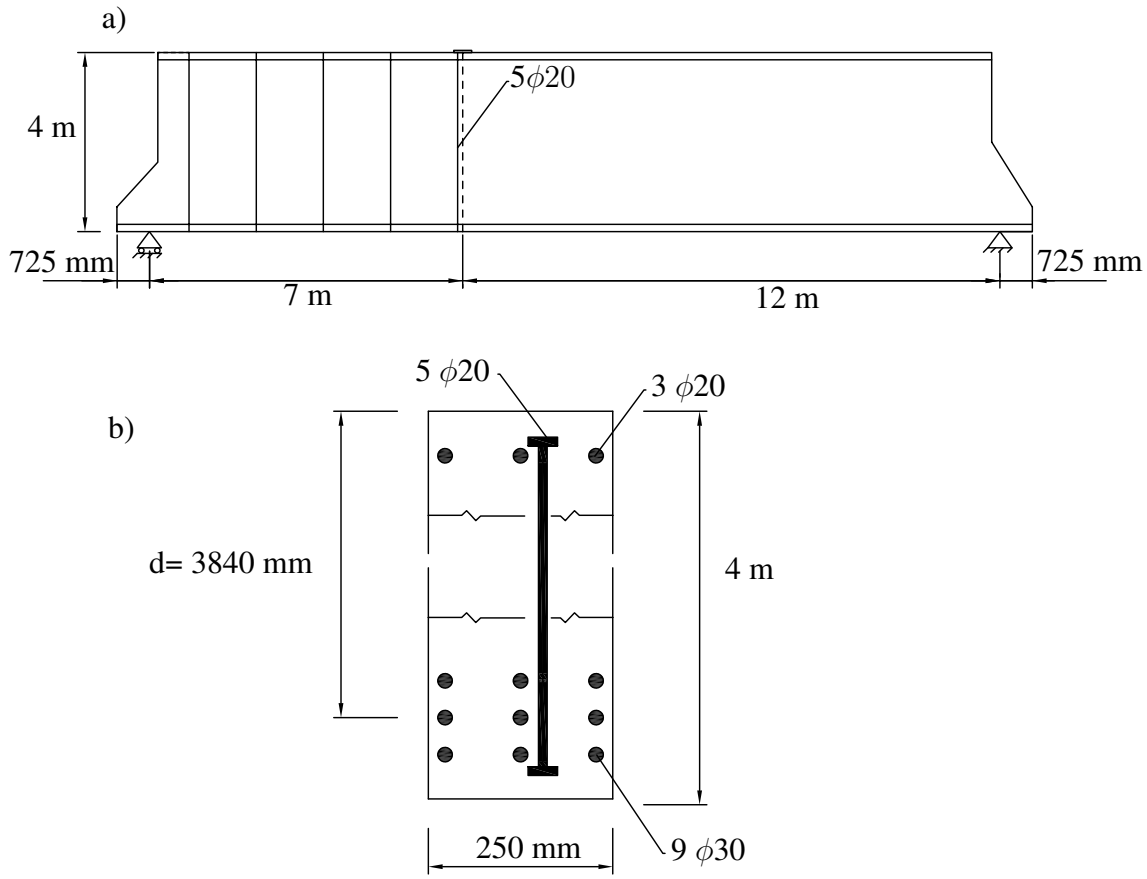

Figure 4.1: a) Elevation of the deep beam. Boundary conditions is roller support to the left and fixed support to the right. b) Section of the beam.

4.2 FE model

The FE model of the beam is modeled in the same fashion as described in Chapter 3. At the position of the support, and where the displacement is applied, steel plates are modeled. This

is so the force can spread out and to avoid elements experiencing unreasonably high stresses. A zoomed in part of the beam is illustrated in Figure 4.2 where the steel plate is also shown down to the left.

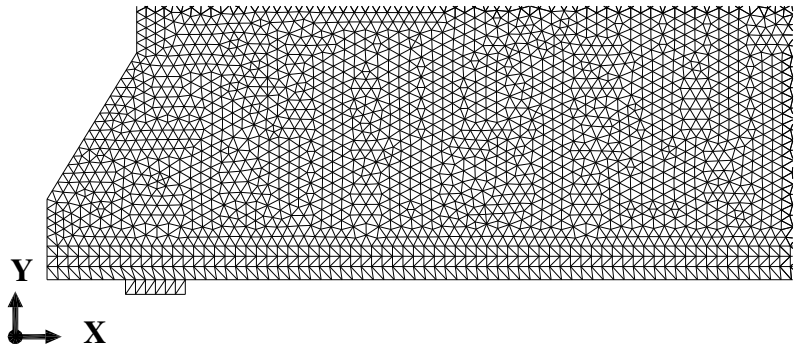

FIGURE 4.2: Zoomed in illustration of the FE model of the deep beam. At the support a steel plate has been placed.

Since the beam consists of 2D planar element and has no depth, the reinforcement has to be merged at the same height. This means that there is only 1 reinforcement bar modeled in the top with a cross section area of 900 mm^2. In the bottom there are 3 bars of reinforcement with a cross section area of 2100 mm^2 per modeled rebar. A summary of the material properties is shown in Table 4.1.

The lower reinforcement is modeled with bond-slip according to previous chapter. The stirrups and upper reinforcement are however modeled as an embedded region to save computational work. This simplification should be negligible since cracking mainly occurs along the lower reinforcement and in the plain concrete regions.

TABLE 4.1: Concrete and steel material properties.

Concrete

Property	Value	Unit
Compressive strength, f_c	40	MPa
Tension strength, f_t	2.48	MPa
Young's modulus, E_c	30	GPa
Density, ρ	2500	kg/m^3
Fracture Energy FIB 1990	85	Nm
Fracture Energy FIB 2010	141.8	Nm
Dilation angle, ψ	30, 35, 38	$^\circ$

Steel

Property	Value	Unit
Yield strength 30M, f_y	573	MPa
Yield strength 20M, f_y	522	MPa
Young's Modulus, E_s	210	GPa
Density, ρ	7800	kg/m^3
Area 30M, A_s	2100	mm^2
Area 20M, A_s	900	mm^2
Area Stirrup A_s	300	mm^2

4.3 Results and validation of FE model

As stated above, the FE model will be validated against scenario 1 where the ACI beam will fail in the east span where there is no shear reinforcement. The FE model is performed with a displacement-controlled loading. The force is measured at the same position where the displacement is applied.

The validation will focus on three quantities, fracture energy, G_f, dilation angle, ψ, and the size of the mesh. The goal is to calibrate the first two quantities so that the FE model will behave similarly to the ACI experiment in a confident way. Later the mesh also has to be checked to establish mesh convergence. Different parameters will be looked upon. The stress at which the first crack occurs is important. The maximum load and deformation before failure is also important. Also, the crack width of the largest crack will be checked and compared to the experiment at a load of 375 kN and failure load. For P = 375 kN the average spacing between the cracks will also be checked

4.3.1 Dilation angle

The dilation angle is tested for 30°, 35°, and 38°. For these dilation angles the FE model has a fracture energy according to Model Code 10 (2012). The load-displacement curves for

the three dilation angles and the experiment are plotted in Figure 4.3. What can be noted from the graph is that there is not a significant difference from different dilation angles. One thing that can be noted is that for higher dilation angle, the beam can carry more load until failure. Regarding the angle $\psi = 30°$ it is assumed to fail when the load starts to decrease at approximately 570 kN. Another thing that can be noted is that the FE model, regardless of the dilation angle, overestimates the tensile strength, i.e. when the first crack occurs.

The crack width at P = 375 kN and failure load are shown in Table 4.2. The crack width is measured for the maximum width at half the height of the beam. It can be noted that the FE model regardless of the dilation angle is overestimating the width of the crack for P = 375 kN. In the FE model for P = 375 kN there are approximately 4-5 cracks, while it in the experiment are 7 cracks. Hence it can be stated that the FE model tends to propagate fewer but wider cracks, while it in the experiment propagate more cracks but not as wide. The crack patterns for P = 375 kN are shown in Appendix B. The table also shows the average spacing between the cracks for P = 375 kN. It can be noted that $\psi = 30°$ gives the most accurate result but regardless of the dilation angle the average crack distance is relatively accurate.

For the failure load the crack width tends to be underestimated. One possible explanation to this is simply that the beam in the experiment experienced a higher load and displacement before failure than it did in the FE model.

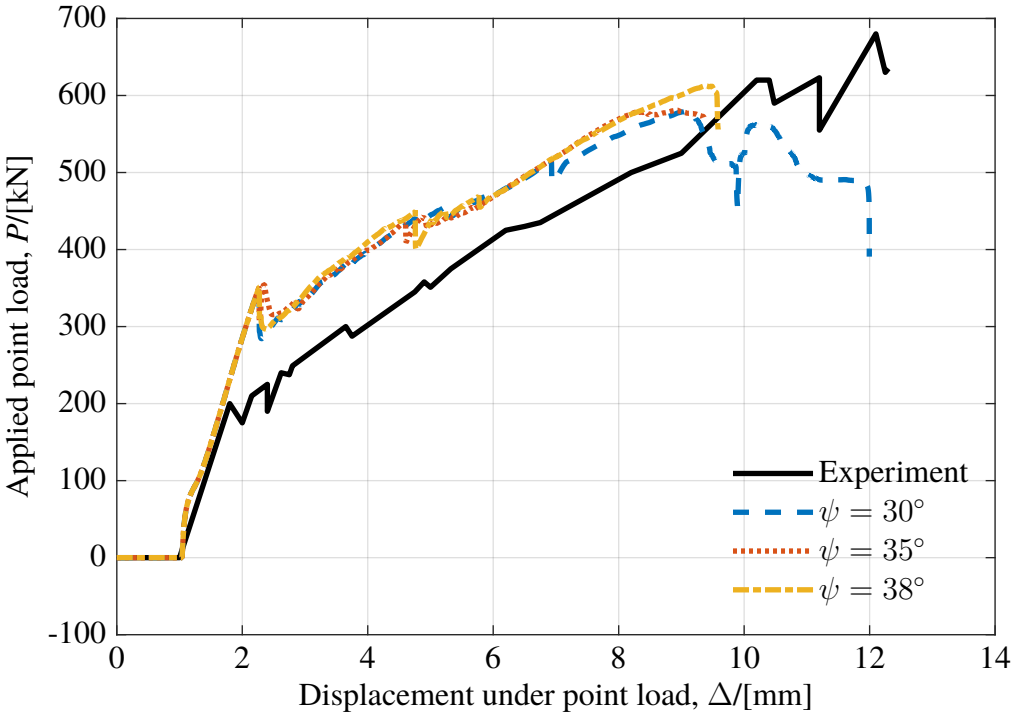

Figure 4.3: Load-Displacement curve for different dilation angles. Fracture energy according to Model Code 10.

TABLE 4.2: Crack widths for different dilation angles for $P = 375$ kN and for failure load. For $P = 375$ kN the average crack spacing is also showed.

$P = 375$ kN				Failure		
Model	Crack width	Spacing		Model	Crack width	
Experiment	0.15	724	mm	Experiment	3	mm
$\psi = 30°$	0.42	725	mm	$\psi = 30°$	0.69	mm
$\psi = 35°$	0.45	650	mm	$\psi = 35°$	0.88	mm
$\psi = 38°$	0.32	647	mm	$\psi = 38°$	1.23	mm

The crack pattern from the experiment and the FE model is shown in Figure B.3a, in Appendix B. In the results from the FE model there is not a distinct shear crack visible. One explanation to this can be that the shear failure is of brittle nature and can be difficult for a FE model to capture since it happens under a small increment of time. There is not a significant difference of the crack patterns for different dilation angles.

From the analysis of the different dilation angles it can be stated that $\psi = 38°$ best approximates the real experiment mainly due to the reason that it takes the highest load of the three different dilation angles. It also has smallest crack width of the three dilation angles which best corresponds to the ACI experiment.

4.3.2 Fracture energy

The fracture energy is tested for two different values. The two values originate from the Model Code 90, G_f=85 Nm, and Model Code 10, G_f=141.8 Nm, as stated in Chapter 2.

The load displacement curves for the experiment and the two fracture energies are plotted in Figure 4.4. From Section 4.3.1 it is stated that the most accurate dilation angle is $\psi = 38°$ and that is also for which angle the fracture energies are plotted. It can be stated from Figure 4.4 that for higher fracture energy, the more load the beam can take before the first crack appears. For the low fracture energy, the curve follows the experiment in a similar way after the first crack appears. However, for the low fracture energy it fails for relatively low load. It can also be stated that both Model Code 90 and Model Code 10 overestimate when the first crack appears. The table also shows the average spacing between the cracks for P = 375 kN. It can be noted that regardless of the fracture energy, the average spacing between the cracks match the experiment quite well. The crack pattern for P = 375 and failure are shown in Figure B.4 and B.3 in Appendix B.

The crack width at P = 375 kN and failure load is shown in Table 4.3. The crack width is measured for the maximum width at half the height of beam. It can be noted that the FE model overestimates the crack width at P = 375 kN. However, for the high fracture energy according to Model Code 10 the crack width is more accurate. For the failure load the FE model regardless of the fracture energy underestimates the crack width. As stated above,

in Section 4.3.1, one explanation to this can simply be that the beam in the experiment experienced a much higher load and deformation at failure.

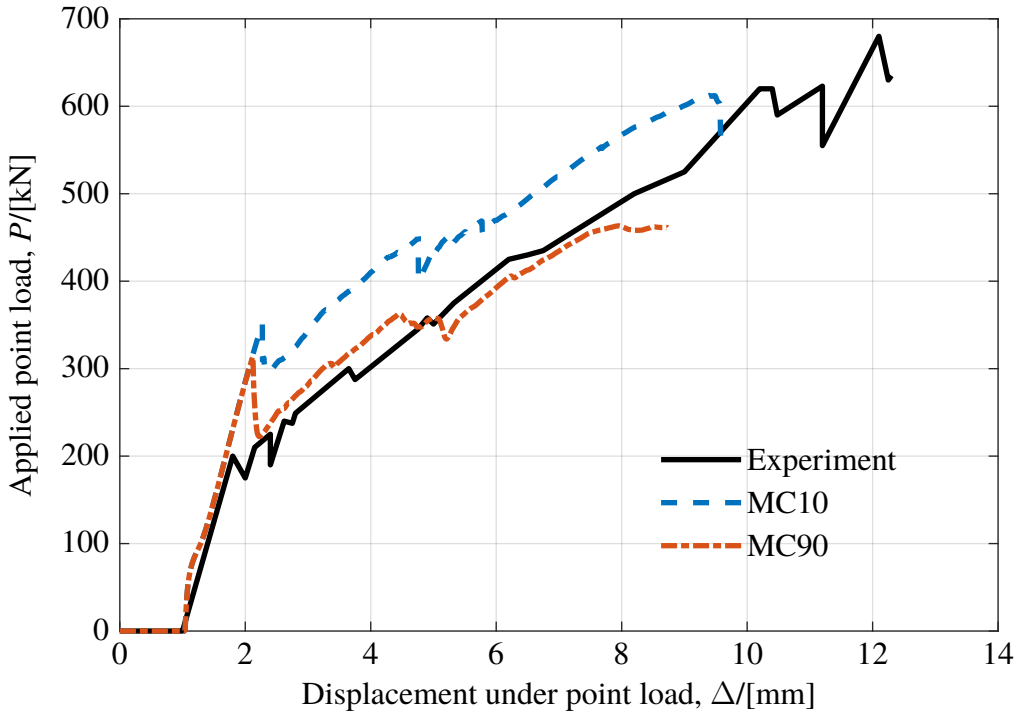

Figure 4.4: Plot of the load - displacement curve for experiment and the two fracture energies Model Code 90 and Model Code 10.

To summarize the validation, it can be stated that the Model Code 10 gives the most accurate response. This is mainly due to two reasons. Firstly, the FE model with the high fracture energy can take more load than the FE model with low fracture energy. The second reason is that the crack width for P = 375 kN for the high fracture energy is more accurate than for low fracture energy.

Table 4.3: Crack widths for different fracture energies for $P = 375$ kN and for failure load. For $P = 375$ kN the average crack distance is also showed.

P = 375 kN				Failure		
Model	Crack width	Spacing		Model	Crack width	
Experiment	0.15	724	mm	Experiment	3.0	mm
Model Code 90	0.68	657	mm	Model Code 90	1.0	mm
Model Code 10	0.32	647	mm	Model Code 10	1.23	mm

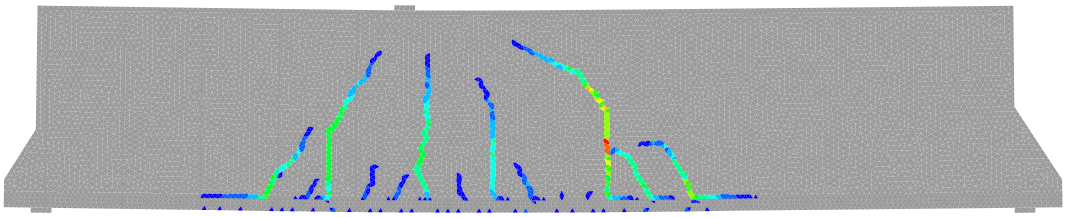

(A) Crack pattern for G_f=141.8 Nm and $\psi = 38°$.

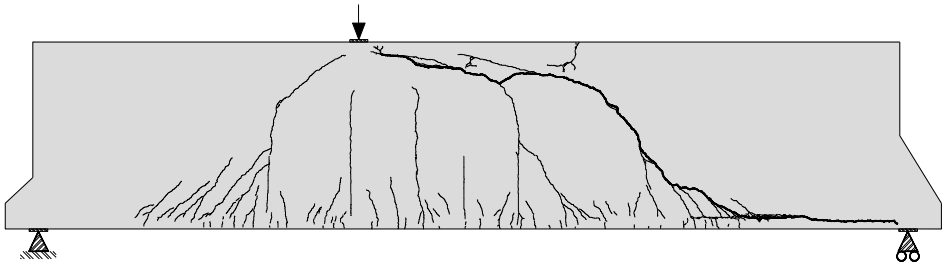

(B) Crack pattern for experiment.

FIGURE 4.5: Crack pattern for experiment and FE-model.

4.3.3 Summary

It is decided that the most accurate FE model corresponds to a model with a dilation angle of $\psi = 38°$ and fracture energy according to Model Code 10 G_f = 141.8 Nm. The crack width at P = 375 kN is approximately double the size compared to the ACI experiment. However, this is on the safe side and in the broader perspective the FE model gives a confident result. The crack pattern for the chosen parameters is shown in Fig 4.5 together with the crack pattern from the ACI Experiment.

4.3.4 Mesh

To assure that the results from the FE analysis are independent from the size of the mesh, a mesh convergence check is conducted. The convergence check is done for the FE model stated above ($\psi = 38°$ and G_f = 141.8 Nm). The mesh type is linear triangular mesh elements, so called CPS3 and is more described in Chapter 3.2.

The FE model is checked for different size of the mesh and later the result is compared. The two parameters that are checked for validating the mesh is average crack width at half the height of the beam for P = 375 kN and P = 500 kN. The convergence check is done for mesh size 500 mm, 100 mm, 80 mm and 60 mm and shown in Table 4.4. It can be stated that for a mesh size of 100 mm, the FE model has converged.

TABLE 4.4: Average crack widths at mid height for different mesh sizes.

Mesh size [mm]	Crack width P = 375 kN [mm]	Crack width P = 500 kN [mm]
500	0.44	0.55
100	0.26	0.49
80	0.24	0.51
60	0.23	0.5

5 Parametric study

The focus of this chapter is to evaluate different wing wall geometries for a slab frame bridge. A deformation pattern is extracted from a global model and inserted in a local model. The global model consists of the whole slab frame bridge and the local model consists of the wing wall alone. The wing wall is parametrized to distinguish different behaviors coupled to its geometry.

5.1 Global model

This section focuses on the global model of the slab frame bridge. One geometry for the bridge is taken into consideration. Load cases are determined for the slab frame bridge and a deformation pattern is extracted over the boundary of the intersection of the frame leg and the wing wall. Brigade/plus is used for the FE analysis.

5.1.1 FE model

The frame bridge is modeled with 3D deformable homogeneous shell elements. The material in the model is concrete of strength class C35/45 with Young's modulus E_c = 34 GPa and linear elastic behavior. The whole bridge is modeled as one part. The supports are modeled with springs with stiffnesses according to Appendix C.

The uniform temperature load is applied over the whole model and the uneven temperature gradient is only applied on the bridge deck. The earth pressure is acting perpendicular to the concrete surface and there is earth pressure on the inside and outside of the frame legs, though only approximately of 1 m height on the inside. The shrinkage is applied as an equivalent temperature field determined in Appendix C, where the other load entities also are determined. The mesh consists of triangular shell elements and is of size 0.2 m for the wing wall and about 0.5 m for the rest of the bridge.

The bridge that is analyzed has a length of 16.0 m, a width of 19.75 m and a height of 7 m, as seen in Figure 5.1 and Appendix A.

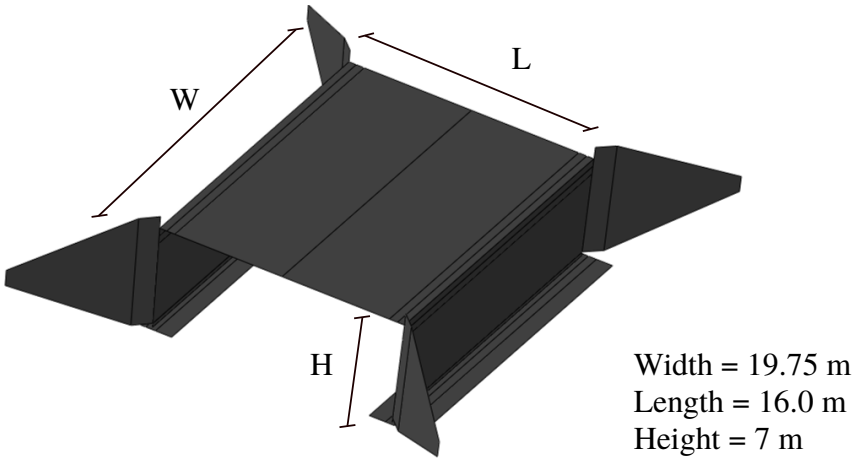

Figure 5.1: Global FE model of slab frame bridge.

5.1.2 Load entities

The bridge is analyzed for quasi-permanent load combination in SLS. The partial coefficients are chosen according to Trafikverkets Författarsamling (TRVFS) 2011:12, which is based on Eurocode. The coefficients for the load combination are described in Table 5.1. What can be noted is that in SLS there are no traffic loads acting on the bridge. The values for the loads are determined in Appendix C. The residual earth pressure corresponds to the increase of earth pressure due to thermal expansion.

What can be noted is that for temperature, support yielding and surfacing there are two different load coefficients, based on whether the load is favorable or not. The loads are determined as favorable or not in the FE analysis. In order to determine if a load is favorable or not the section forces are checked in the wing wall. If a load results in a negative section force, i.e. compression, in critical tension areas it will be considered favorable.

Creep is considered in Brigade/plus by a scale factor in the load combination, shown in the third and fourth column in Table 5.1. For some loads the creep will increase the deformation, and for certain loads the creep will reduce the force. "Disp" in the third column specifies the factor at which the deformation is increased with. "Force" in the fourth column specifies at which factor the force is reduced with.

TABLE 5.1: Values of load coefficients for quasi-permanent load combination. "Disp" and "Force" are scale factors for considering creep.

Load	Load Coefficient	Disp.	Force
Permanent loads			
Self weight	1/1	2.7	1
Earth pressure	1/1	2.7	1
Surfacing	1.1/0.9	2.7	1
Opposite support yield vertical	1/0	1	0.42
Adjoining support yield vertical	1/0	1	0.42
Opposite support yield horizontal	1/0	1	0.42
Adjoining support yield horizontal	1/0	1	0.42
Overburden	1/1	2.7	1
Shrinkage	1/1	1	0.42
Variable loads			
Uniform temperature low	0.5/0	1	0.79
Uniform temperature high	0.5/0	1	0.79
Temperature difference low	0.5/0	1	1
Temperature difference high	0.5/0	1	1
Residual earth pressure	0.5/0	1	0.79
Traffic loads	0	-	-

5.1.3 Load combination

The load combination is simplified into two extremes, SLS low and SLS high. The load entities used in each combination is specified in Table 5.2. SLS low refer to a low uniform temperature and SLS high to a high uniform temperature. The other loads are determined to be unfavorable if they correspond to an increase of tension in areas where the respectively uniform temperature load corresponds to tension section forces. The two load combinations are considered since it is to tell in advance hard which will be most adverse for the respective wing walls.

An example of the normal forces in direction 1 and 2 for SLS low and SLS high can be seen in Figure 5.2.

TABLE 5.2: Load combination for SLS low and SLS high.

SLS low	SLS high
Self weight	Self weight
Earth pressure	Earth pressure
Surfacing	Surfacing
Overburden	Overburden
Shrinkage	Shrinkage
Adjoining support yield horizontal	Opposite support yield horizontal
Uniform temperature low	Opposite support yield vertical
Temperature difference low	Uniform temperature high
	Temperature difference high
	Residual earth pressure

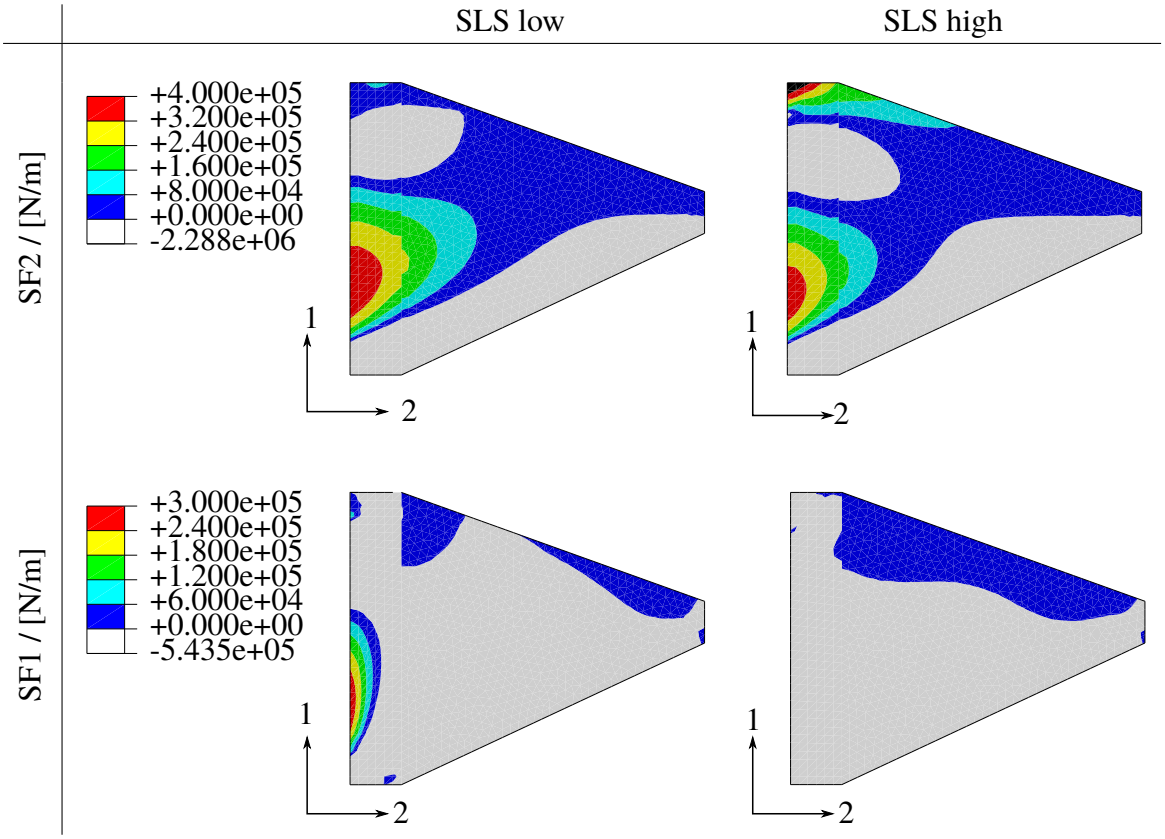

FIGURE 5.2: Example of normal forces in direction 1 and 2, SF1 respectively SF2, for load combination SLS high and SLS low.

5.2 Local model

The local model concerns the wing walls of the slab frame bridge. The wing wall is first designed linearly according to Eurocode and then analyzed with a 2D non-linear FE-model in Brigade/Plus. Different geometries and amount of reinforcement are analyzed. Results from the global FE-model are used for the linear design and non-linear analysis.

5.2.1 Geometries

The geometry of the wing wall is parametrized into the parameters in Table 5.3. For simplicity the wing walls are approximated by two parts, one rectangular part and one trapezoidal part. The inclination of the trapezoidal part is limited by the maximum allowed slope of the ground, which is approximately determined to 1:2. The upper and lower inclination is the same, so the wing walls are symmetrical with respect to the horizontal plane.

Table 5.3: Wing wall geometry parameters. The symbols are shown in Figure 5.6.

Dimension	Symbol	Values
Length of rectangular part	L_1	1 m
Length of trapezoidal part	L_2	2, 4, 6 m
Height by frameleg	H_{Frame}	3, 5, 7 m
Height at edge	H_{Edge}	1, 3, 5 m
Inclination	Δ	1:2, 1:3, 1:4, 1:6

The dimensions for the 9 different geometries are shown in Figure 5.3.

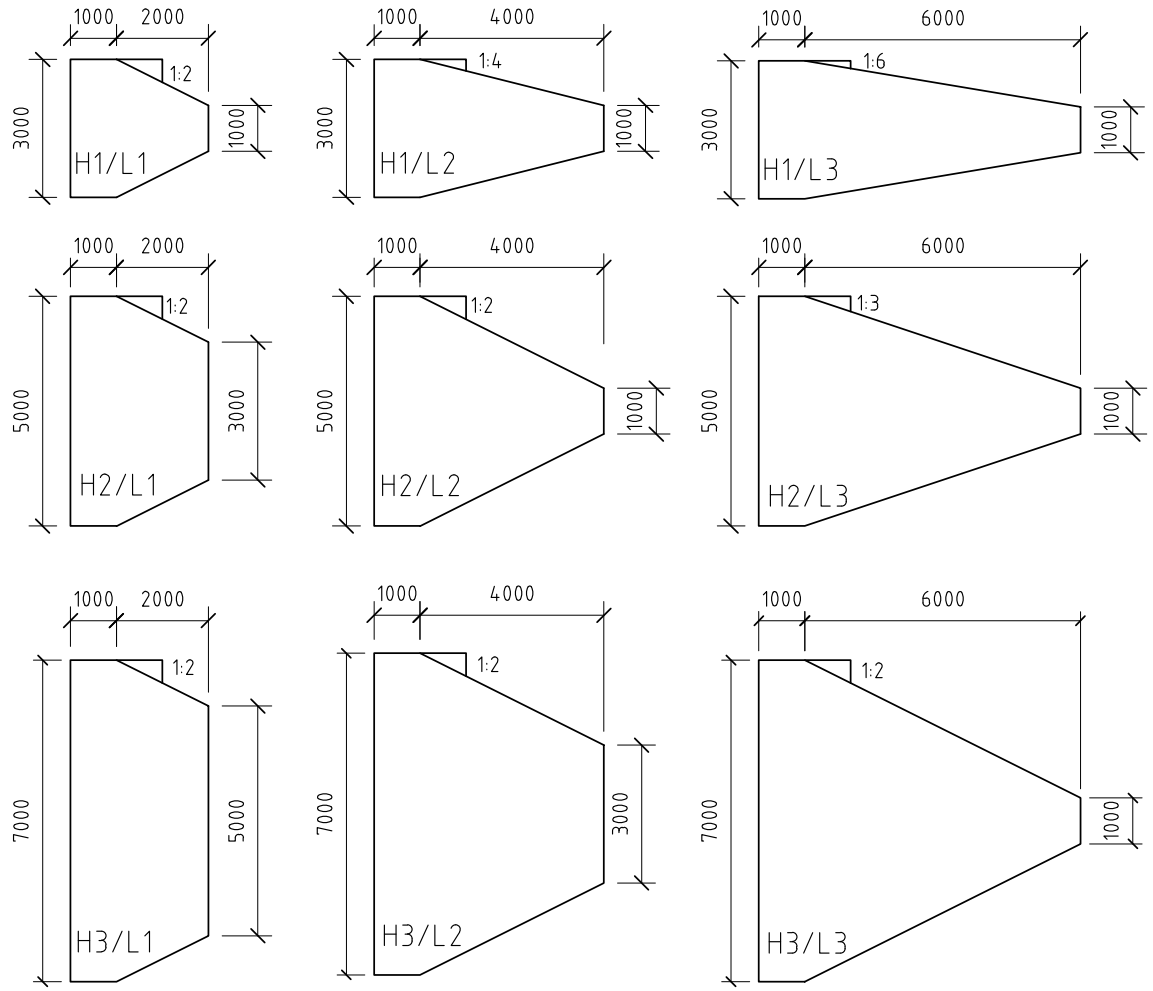

Figure 5.3: Dimensions of wingwall geometries.

5.2.2 Linear design

The linear design is done according to the regulations concerning bridges and concrete in Eurocode. The design is done with help of an in-house toolbox for reinforcement design for bending and twisting in concrete shells, provided by ELU Konsult.

From the global model in Brigade/Plus, normal forces, moment and geometry for the wing wall is exported for the two load combinations, SLS high and SLS low. Also, the section forces for only earth pressure on the wing wall is exported to compare the difference in reinforcement amount. The differences in the reinforcement amount between the SLS combinations and earth pressure illustrate the extra amount of reinforcement due to the membrane forces.

From the design, the reinforcement amount is obtained for the wing walls in each element node from the global mesh. The reinforcement amount is provided as reinforcement area per length for top and bottom side, and in each direction. In order to obtain the total reinforcement amount, i.e kg reinforcement per m^3 concrete, the node values are integrated

over their respective area. This area is determined by Delaunay triangulation and summation over all nodes provide the total reinforcement amount.

The result from the linear design is presented in Chapter 6 and Appendix D with figures showing the required amount of reinforcement.

In the design, bending, twisting and normal forces are taken into consideration when the reinforcement is calculated. This is done in accordance to Bro 2004 Part 4 Appendix 4-5.

The maximum crack width is controlled by the design working life and exposure class according to TRVFS 2011:12. These preconditions vary for different bridges and wing walls, but is in the analysis assumed to be the same. The wing walls are considered to be a part of the substructure with a design working life of 120 years, L100. The wing walls are also assumed to be exposed to moderate humidity on the side towards the earth regarding corrosion induced by chlorides, which corresponds to the exposure class XD1.

The exposure class and design working life is used to determine the concrete cover, maximum crack width and a crack safety factor. For L100 and XD1 the maximum allowed crack width is $w_{max} = 0.2$ mm (TRVFS 2011:12, 21 kap.11 §). The minimum concrete cover is determined for the concrete class C35/45 with a water cement ratio, w/c ≤ 0.4, to c_{nom} = 40 mm. The crack safety factor is used to reduce the tensile strength of the concrete when determining if a section is cracked or uncracked. If the section is cracked the reinforcement is designed with the assumption of a cracked section. The factor is determined to $\zeta = 1.5$ for L100 according to TRVFS 2011:12, 21 kap. 12 § (Trafikverket, 2011a).

According to TRVR Bro 11, D.2.2.1.6 (Trafikverket, 2011b), the top values for the normal force and moment are allowed to be distributed over a distance in FEA. The distance can for plates in SLS be taken as twice the plate thickness. This distribution is done the design.

When calculating the reinforcement amount, the diameter of the reinforcement is determined in advance and the c/c distance is to be determined in the calculations. The horizontal reinforcement at earth side, which is subjected to tension from the earth pressure, is given a diameter of $\phi = 20$ mm and the vertical reinforcement a diameter of $\phi = 12$ mm.

5.2.3 Non-linear analysis

The non-linear analysis is performed to check whether the membrane forces are a problem as a consequence of the linear design or if the membrane forces will cause wider cracks. Since it is a non-linear analysis, superposition of the loads is not possible, so all forces acting on the wing wall should be considered at the same time in the analysis.

The membrane forces, which are obtained from the deformation of the wing wall due to loads on the rest of the bridge, are considered by a deformation pattern on the adjoining edge to the frame leg. The moment in the wing wall from the earth pressure is applied as an equivalent body force. The other loads: shrinkage, gravity and uniform temperature are also applied in the local non-linear model. The deformation pattern and the applying of other loads, and

also creep, which is considered, are explained further for the local model. But first the FE model is described.

FE model

The non-linear analysis is performed with 2D plane stress elements for concrete and 1D truss elements for reinforcement as described in chapter 3. The concrete is of the strength class C35/45 and modeled with the plasticity parameters in Table 3.2, where the dilation angle was determined in chapter 4 to $\psi = 38°$. The viscosity is put to $\mu = 10^{-7}$. Also, bond-slip is considered and modeled as described in chapter 3.

In the non-linear local model, the thickness of the concrete is modeled as the effective thickness determined in the linear design according to Eurocode and in accordance with the theory described in section 2.2.1, regarding the effective area for thick reinforced members. The effective thickness, w_{eff}, is determined approximately for all sections to:

$$w_{\text{eff}} = 2.5(c_{nom} + \phi/2) \tag{5.1}$$

This effective thickness should represent the concrete on the earth side subjected to tensile stresses, when assuming a cracked section. The membrane forces that originates from the deformation of the frame leg is then assumed to be uniformly distributed over the thickness and the reinforcement subjected to the membrane forces in the effective area in addition to the stresses from the moment from the earth pressure.

Deformation pattern

When the bridge is subjected to different load combinations it will deform. The deformation of the frame leg, where the wing wall is connected, is of interest. The displacement of each node, at the intersection of the frame leg and the wing wall, is extracted from the global FE model. This is done for the global coordinates, see Figure 5.4a. The wing wall is of angle 45 $^{\circ}$ as can be seen in Figure 5.4b. The node displacements are then transformed into the local coordinate system of the wing wall as defined in Figure 5.4c. Only the deformation in the local plane of the wing wall, i.e. $\hat{x}$ and $\hat{y}$, is applied in the non-linear analysis.

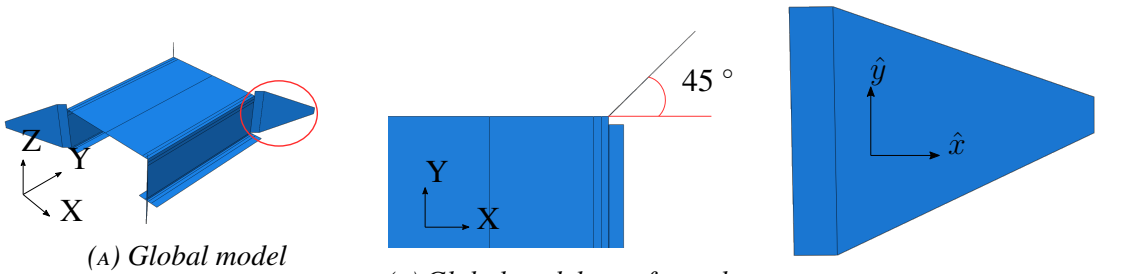

(A) *Global model* (B) *Global model seen from above* (C) *Local model of wing wall*

FIGURE 5.4: Transformation of global coordinates to local coordinates.

Earth pressure

Aside from the membrane forces, the wing wall is also subjected to earth pressure, gravity, temperature, shrinkage and creep. All load entities except earth pressure are implemented in the non-linear model directly. However, for the earth pressure it is different. Since the wing wall consists of plane stress elements, and can not take any bending or force perpendicular to its plane, the earth pressure can not be directly applied in the non-linear model.

Instead the section moments from the earth pressure are extracted from the global linear model and saved in data series. From the data series a surface function is approximated, which describes the section moment as a function of the two directions of the plane of the wing wall, $\hat{x}$ and $\hat{y}$. This is however only done for the section moment in the longitudinal $\hat{x}$-direction, of the wing wall, SM2. The section moment in the vertical direction is of a factor 10 less and hence is neglected. The function is a 5:th degree polynomial in each direction and described below.

$$F(\hat{x},\hat{y}) = a_1 + a_2\hat{x} + a_3\hat{y} + \cdots + a_{19}\hat{x}^5 + a_{20}\hat{y}^5 \approx \mathrm{SM2}(\hat{x},\hat{y}) \ \ [\mathrm{Nm/m}] \tag{5.2}$$

To approximately implement the stresses that the section moments will give in every section, a body force with an analytical field is used in Brigade/plus. The analytical field is given by the derivative of the surface function with respect to the x-direction, $f(\hat{x},\hat{y}) = \frac{\partial F(\hat{x},\hat{y})}{\partial x}$. The amplitude of the body force is derived assuming a cracked section, where the tension force from the moment is taken by a force couple from the reinforcement. The force in the reinforcement is approximately given by $F_M = \mathrm{SM2}/h_{lever}$, where h_{lever} is the distance between the reinforcement at earth and air side, i.e. $h_{lever} = w - 2c_{nom} - \phi$. See Figure 5.5 for explanations. The body force is applied to the concrete elements, so F_M should be spread over the thickness of the modeled wing wall, i.e. the body force is given by:

$$b_M(\hat{x},\hat{y}) = \frac{f(\hat{x},\hat{y})}{(w - 2c_{nom} - \phi)\cdot w_{\text{eff}}}, \tag{5.3}$$

where w is the thickness of the wing wall in the global model.

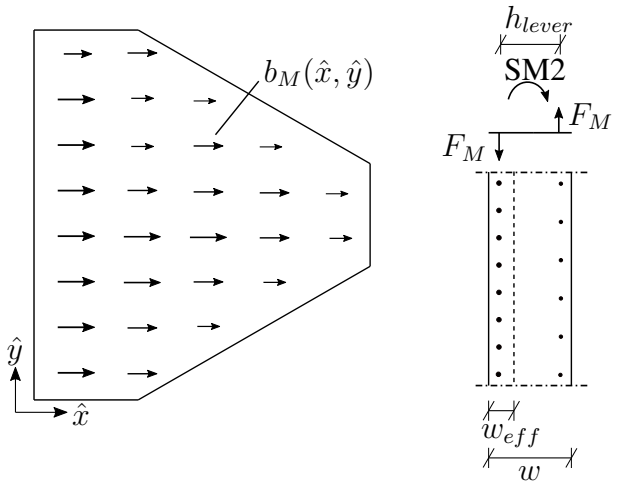

FIGURE 5.5: Applied body force $b_M(\hat{x},\hat{y})$ from the section moment SM2 with assumptions regarding the force couple and effective thickness.

Temperature

The temperature load is directly implemented in the FE model with temperature fields. In the FE model there are only uniformly distributed temperature fields occurring. The concrete and the steel are subjected to the same temperature field. The temperature field is reduced with a factor 0.5 according to standard Eurocode for SLS. The shrinkage is converted to a corresponding negative temperature field and applied to the concrete elements only.

Creep

For considering creep, the elastic modulus of the concrete is reduced to an effective elastic modulus. This will redistribute some load from the concrete to the reinforcement. Note that no load is reduced, as contrary to certain loads in the global linear FE model. It is only the stiffness of the concrete that is reduced.

Crack safety factor

To account for the crack safety factor in the non-linear analysis, the loads are increased with this factor instead of reducing the tensile strength of the concrete, as in the linear design. This is to avoid a change of failure type, which could be the case when reducing the tensile strength.

Reinforcement

Since only the effective thickness on the wing wall's earth side is modeled, only the reinforcement in this part should be implemented. The reinforcement layout is simplified from the calculated reinforcement in the linear design, to minimize the modeling. The simplifications are shown in Figure 5.6. The vertical reinforcement is given the same diameter and c/c-distance, s, over the whole wing wall length. The horizontal reinforcement is simplified to two different types, one going from the frame leg to half the length of the wing wall and one over the whole length, as seen in Figure 5.6. A surface reinforcement is placed along the edges of the wing wall and extra reinforcement is placed at the connection to the frame leg. Symbols for the reinforcement parameters are shown in Table 5.4 and values determined in the linear design shown in Table 6.1. The wing walls are first modeled with the reinforcement from the design for only earth pressure and checked against the max crack width requirement.

TABLE 5.4: Wing wall reinforcement diameter, ϕ, and c/c-distance, s, respectively number of bars, n, for the simplified layout in the non-linear analysis.

Reinforcement	Diameter	s/n
Vertical	ϕ_{V}	s_{V}
Horizontal earth whole length	ϕ_{H_1}	s_{H_1}
Horizontal earth half length	ϕ_{H_2}	s_{H_2}
Surrounding	ϕ_{S}	n_{S}
Frame leg connection	ϕ_{F}	n_{F}

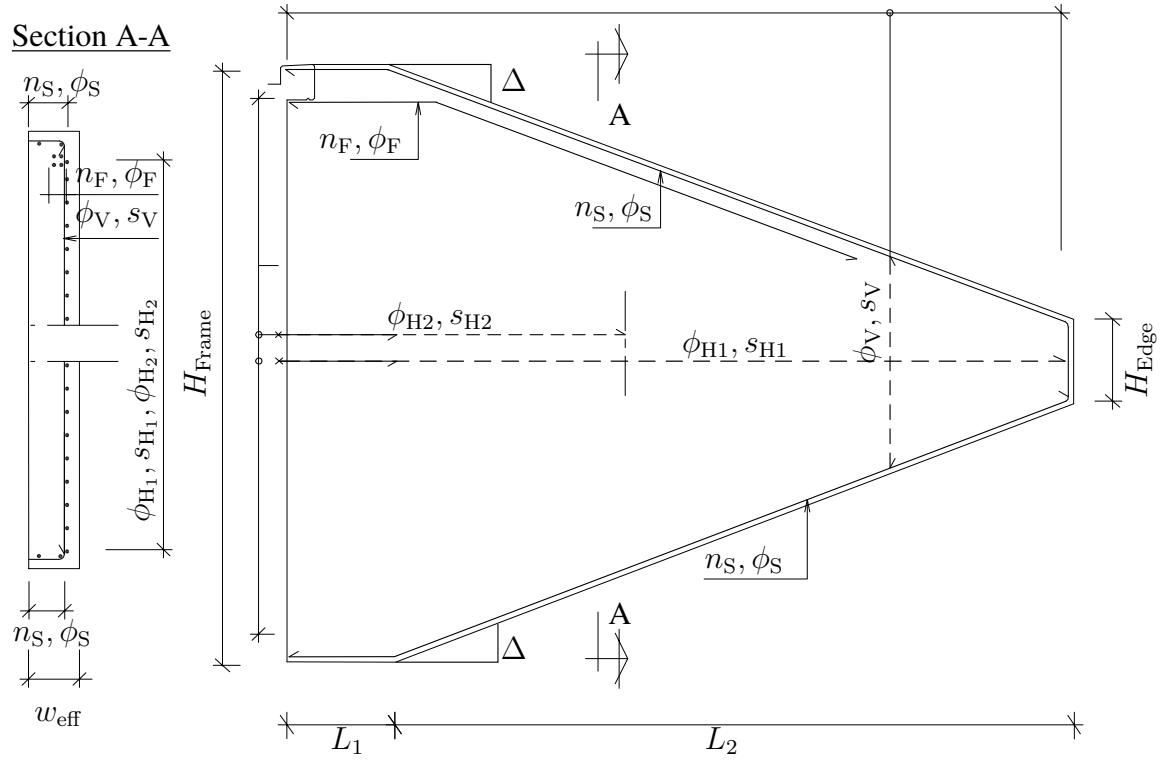

FIGURE 5.6: Reinforcement drawing for simplified layout in the non-linear analysis. Values for the geometry parameters are presented in Table 5.3 and Figure 5.3.

6 Results

6.1 Linear design

In this section the results from the parametric study of the linear analysis are presented. It consists mainly of two parts. The first part describes the distribution of required reinforcement in the wing wall. The results for wing wall H1L3, H3L1 and H3L3, with geometries according to Figure 5.3, are shown. The other 6 wing walls are shown in Appendix D together with the 3 shown in this chapter, i.e. all wing walls concerning the master thesis are shown in Appendix D.

For each wing wall there are two charts of plots. The first chart is of dimension 3x3 and shows the required reinforcement for SLS high, SLS low and for earth pressure. In the top of the wing wall there is both longitudinal and vertical reinforcement. The top of the wing wall is the surface towards the soil and the bottom of the wing wall is the surface towards the air.

In the bottom of the wing wall there is only need of vertical reinforcement. This is due to the reason that for the longitudinal direction the earth pressure will cause tension in the top and compression in the bottom and hence, there will be no longitudinal reinforcement in the bottom, except the minimum reinforcement.

For earth pressure the membrane forces are reduced to zero, i.e. the plot of the earth pressure only shows the required reinforcement from the moment.

It should be noted that the earth pressure also give rise to some membrane forces in the wing wall. This can be due to deformation of the frame leg, which will generate membrane forces in the wing wall caused by the earth pressure. However, it is only the pure bending that is considered from the earth pressure.

The second chart is of dimension 3x2 which shows the required reinforcement of the membrane forces of SLS high and SLS low. Here the required reinforcement from the earth pressure is subtracted from SLS high and SLS low. What is left is the required reinforcement from only membrane forces.

The second part consists of bar plots where the aim is to show relationships for varying geometries.

6.1.1 Wing wall H1L1

The required reinforcement for H1L1 is shown below. What can be noted from Figure 6.1 is that for SLS high there tends to be a higher required amount of reinforcement compared to SLS low. In Figure 6.2 there is a higher need of reinforcement for SLS high compared to SLS low. It can also be noted that for Top-Longitudinal the membrane forces result in a need of reinforcement in the top left corner of the wing wall.

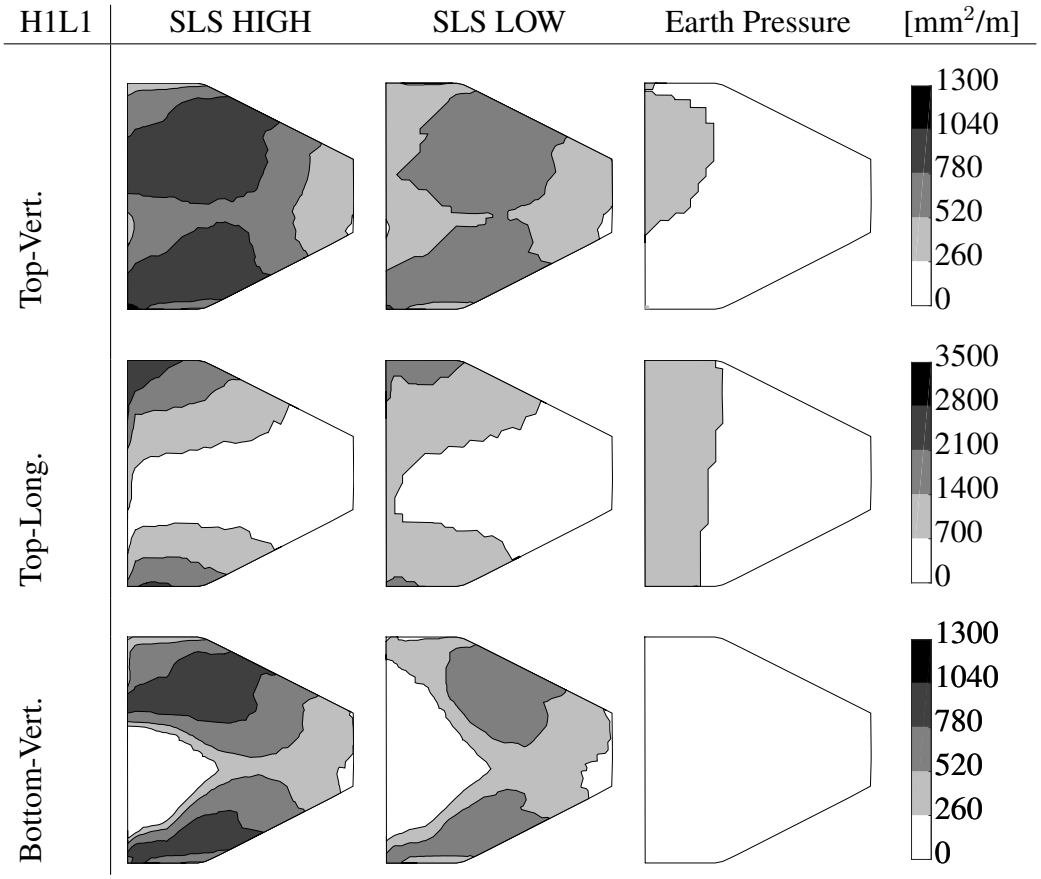

Figure 6.1: Longitudinal and vertical reinforcement for top and bottom side of wing wall H1L1.

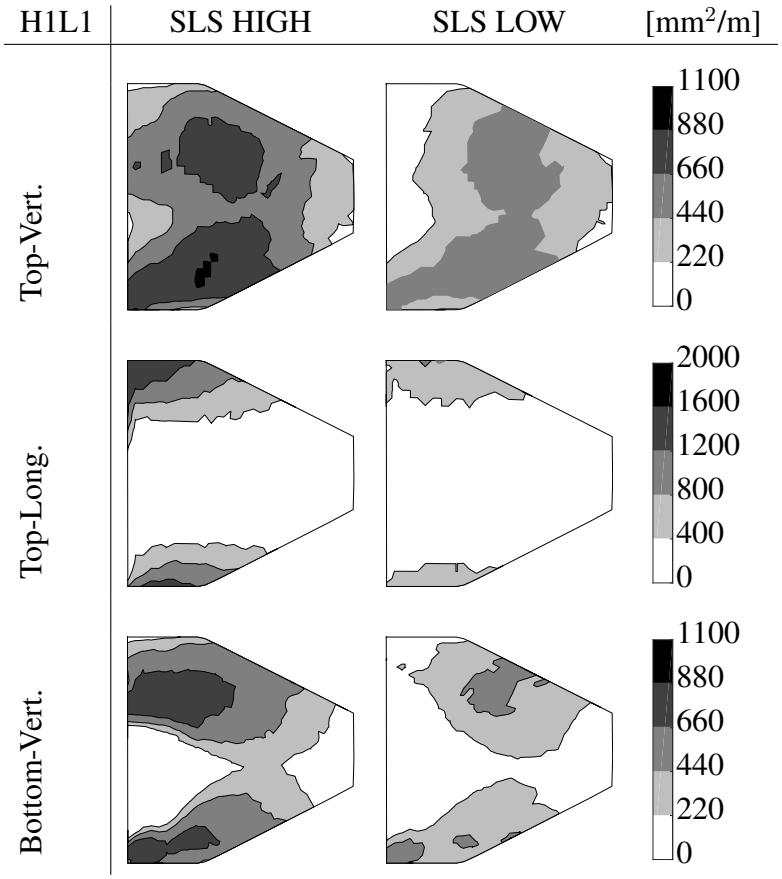

FIGURE 6.2: Reinforcement caused by only membrane forces for H1L1.

6.1.2 Wing wall H2L1

The required reinforcement for H2L1 is shown below. As for wing wall H1L1 it can be noted from Figure 6.3, that for SLS high there tends to be a higher required amount of reinforcement compared to SLS low. In Figure 6.4 there is higher need of reinforcement for SLS high compared to SLS low. It can also be noted that for Top-Longitudinal the membrane forces result in an extra need of reinforcement in the top left corner of the wing wall as for wing wall H1L1.

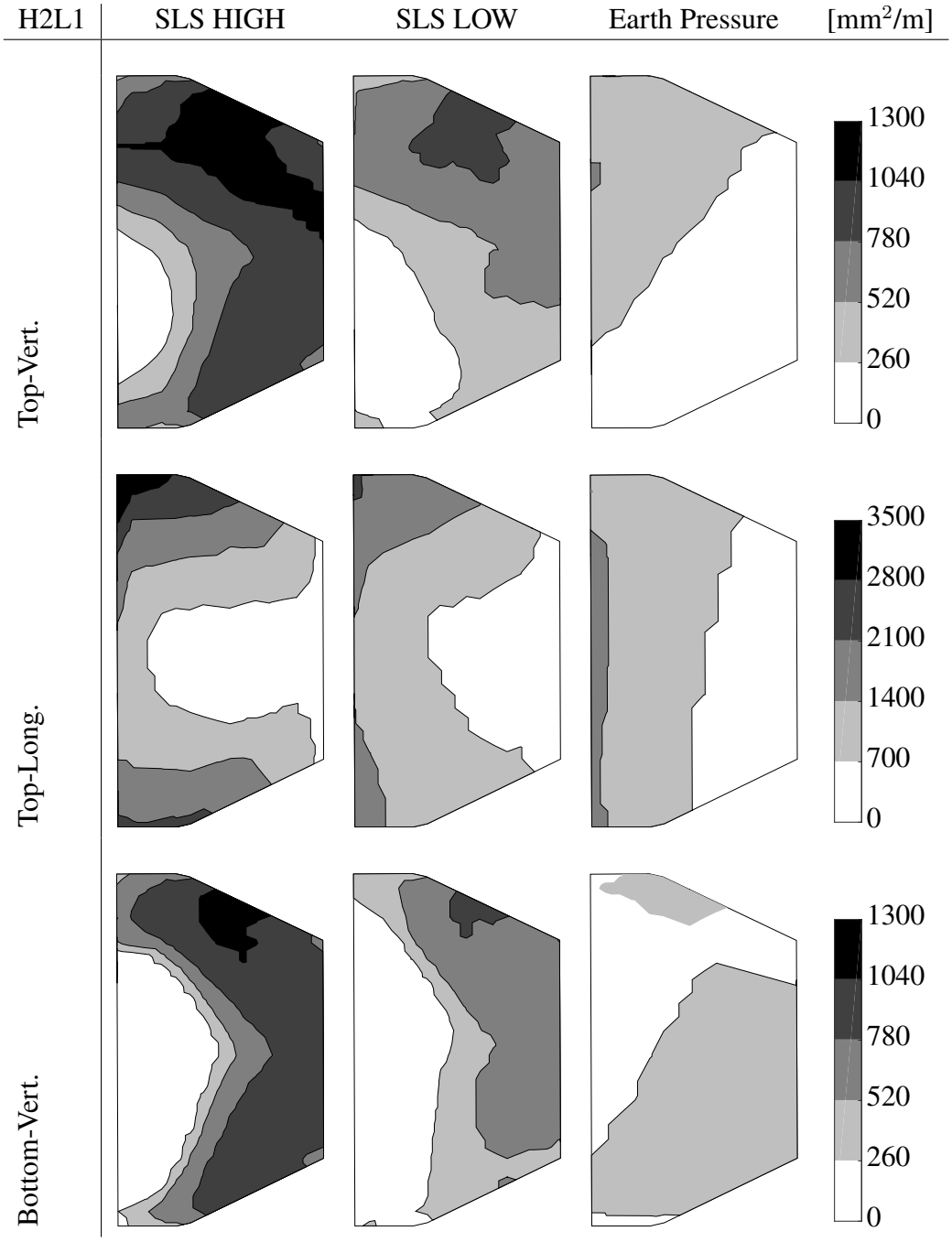

Figure 6.3: Longitudinal and vertical reinforcement for top and bottom side of wing wall H2L1.

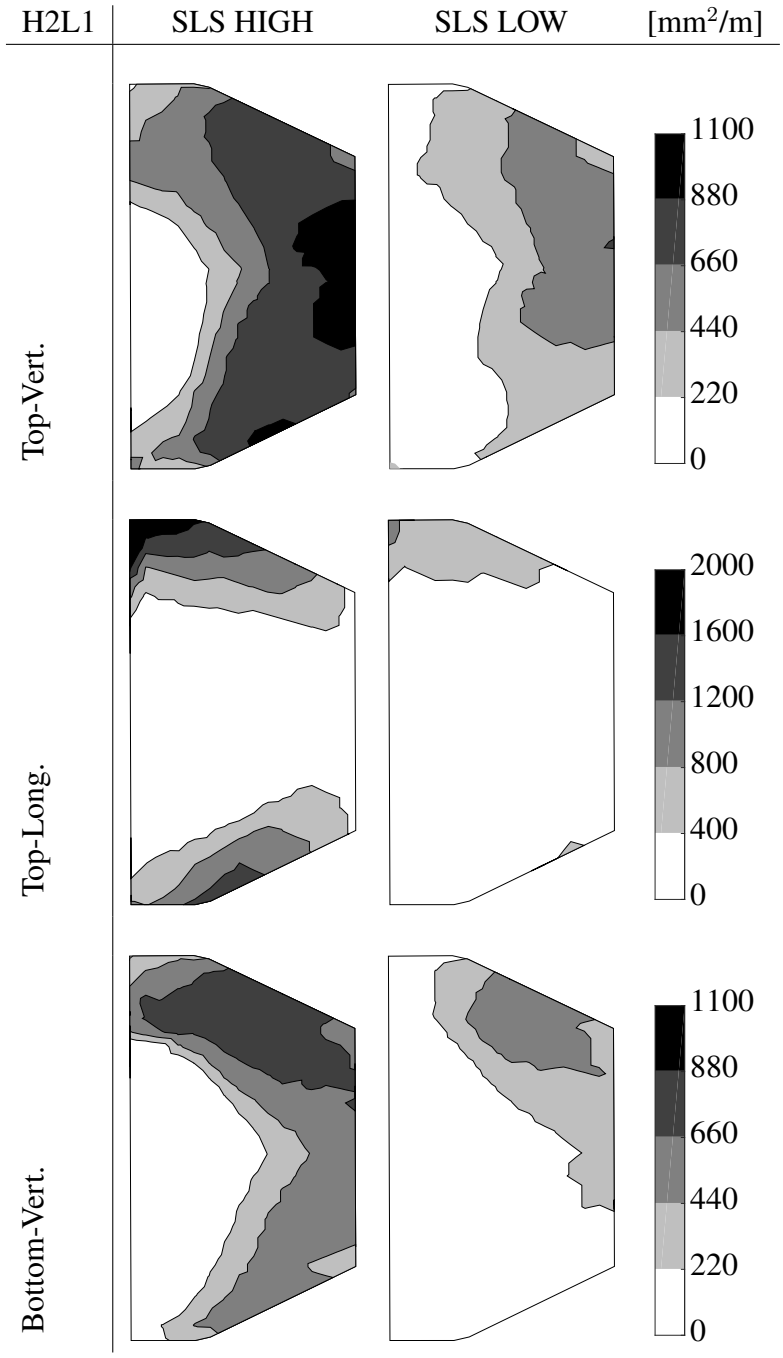

FIGURE 6.4: Reinforcement caused by only membrane forces for H2L1.

6.1.3 Wing wall H3L1

For H3L1, the required reinforcement is shown below. What can be noted from Figure 6.5 is that for SLS high there tends to be higher required reinforcement compared to SLS low. In Figure 6.6 there is higher need for reinforcement for SLS high compared to SLS low. It can also be noted that for Top-Longitudinal the membrane forces result in a need of reinforcement in the top left corner of the wing wall. For the vertical reinforcement the membrane forces tend to give a need of reinforcement in the outer edge of the wing wall.

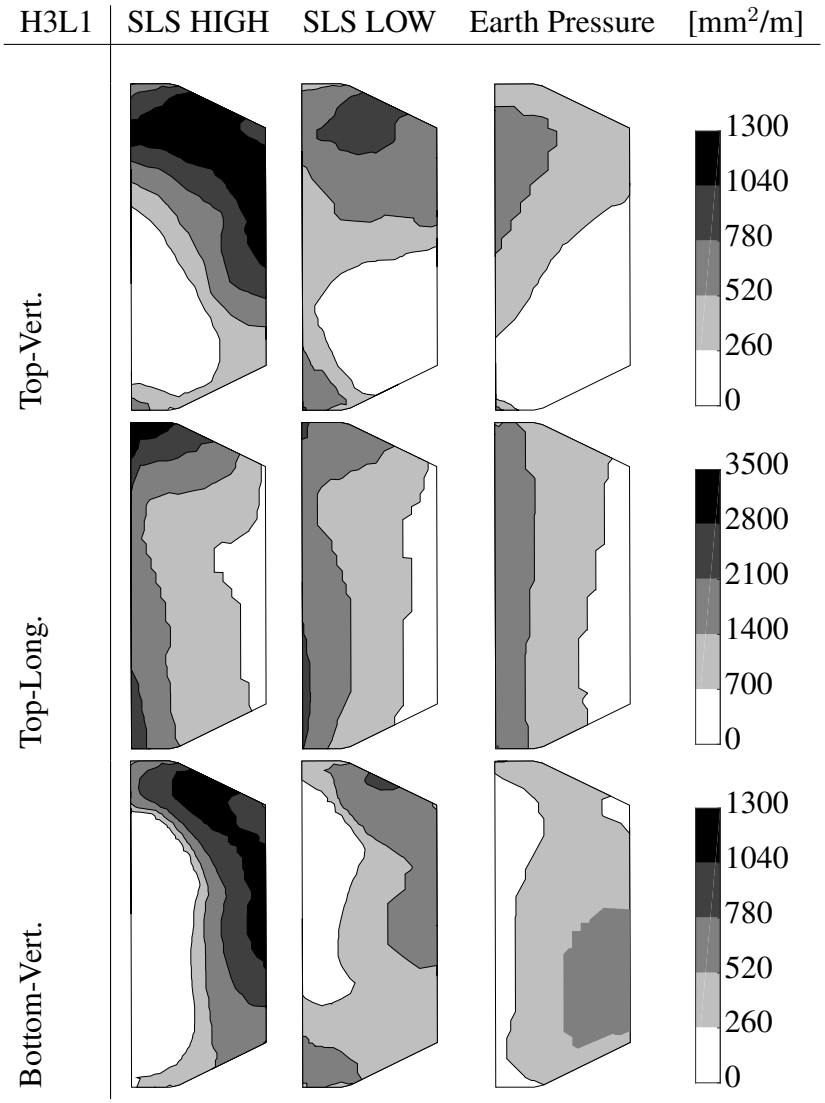

Figure 6.5: Longitudinal and vertical reinforcement for top and bottom side of wing wall H3L1.

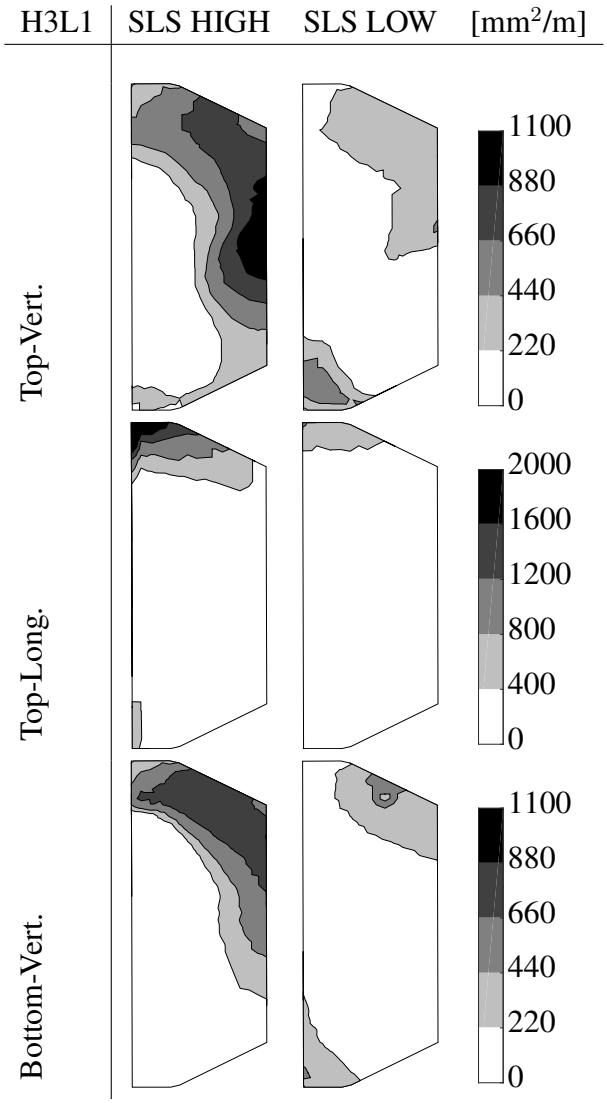

FIGURE 6.6: Reinforcement caused by only membrane forces for H3L1.

It can be noted from all the wing walls that there is a high demand of longitudinal reinforcement due to membrane forces in the top left corner of all the wing walls. The demand of vertical reinforcement is not as concentrated as for the longitudinal, but it is more evenly spread out over the entire wing wall.

6.1.4 Comparison of top 10 % required reinforcement

To get an overview of the required reinforcement in the wing walls, bar plots are produced. The target is to identify relationships connecting the geometry of the wing wall to the required amount of reinforcement caused by the membrane forces.

One evaluation that is conducted is concerning the area of the wing wall that experiences the highest need of reinforcement caused by the membrane forces. The area experiencing the top 10 % need of reinforcement is isolated and analyzed. This area is denoted as the critical area. These values of the critical area are averaged and plotted with bars in Figure 6.7 and 6.8.

For the vertical reinforcement at Top it can be noted that for constant height and increasing length of the wing wall, the required reinforcement due to membrane forces is decreasing. This is seen for all the heights and both for SLS high and SLS low. The same tendency is not equally as true regarding Top - Longitudinal and Bottom - Vertical.

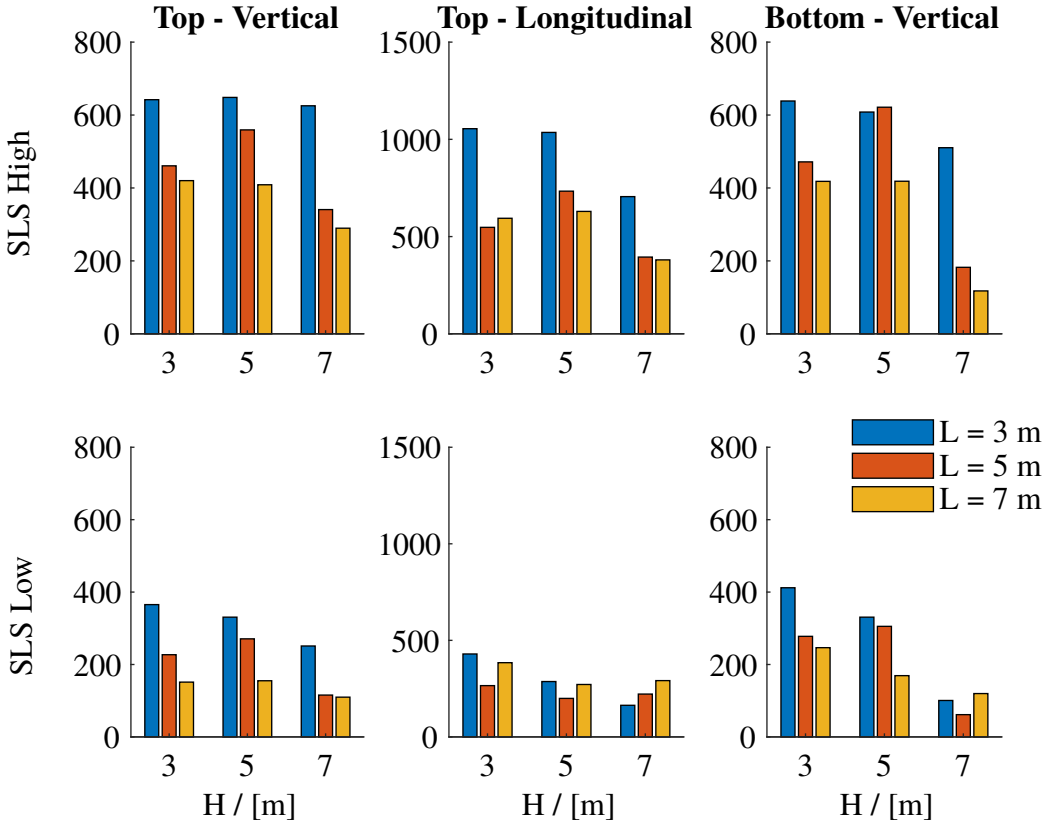

Figure 6.7: Bar diagram of the mean value of required reinforcement [mm^2/m] that originates from the membrane forces in the critical area of the wing wall.

Figure 6.8 illustrates how large the need of reinforcement that originates from the membrane forces are in relation to the need of reinforcement that originates from the earth pressure. For example, for the vertical reinforcement in the top for H = 3 m L = 3 m, the required amount of reinforcement due to membrane forces is almost twice as great as the required amount of reinforcement due to earth pressure.

It can be noted that for constant height and increasing length of the wing wall, the relative amount of required reinforcement that originates from the membrane forces is decreasing.

The same tendency is seen for constant length and increasing height of the wing wall. This is seen for almost all geometries for both SLS high and SLS low.

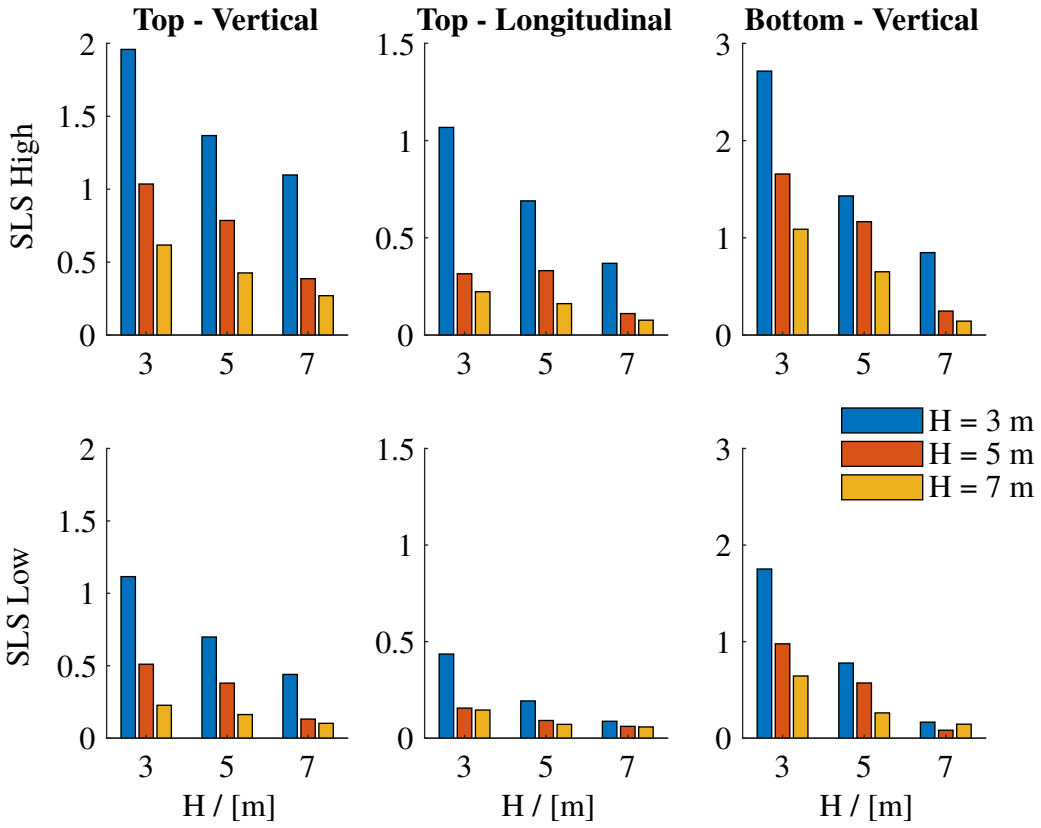

Figure 6.8: Bar diagram of the ratio between the required amount of reinforcement due to membrane forces and earth pressure, in the critical area of the wing wall.

6.1.5 Comparison of total required reinforcement

In Figure 6.9 the total mass of required reinforcement divided by the total volume of concrete is shown $\left[\mathrm{kg_{steel}}/\mathrm{m^3_{concrete}}\right]$. The procedure of retrieving the data is described in Chapter 5.2.2. One thing that can be noted is that the amount of longitudinal reinforcement per cubic meter concrete is increasing with increasing height and length.

In Figure 6.10 the mass of steel divided by the total volume of concrete is shown. In this figure the mass of steel is the required amount of reinforcement due to the membrane forces for SLS high and SLS low in absolute value $\left[\mathrm{kg_{steel}}/\mathrm{m^3_{concrete}}\right]$. In absolute values there will be more vertical than longitudinal reinforcement at the Top caused by the membrane forces. It can also be noted that the vertical reinforcement caused by the membrane forces tends to decrease for increasing height and length of the wing wall.

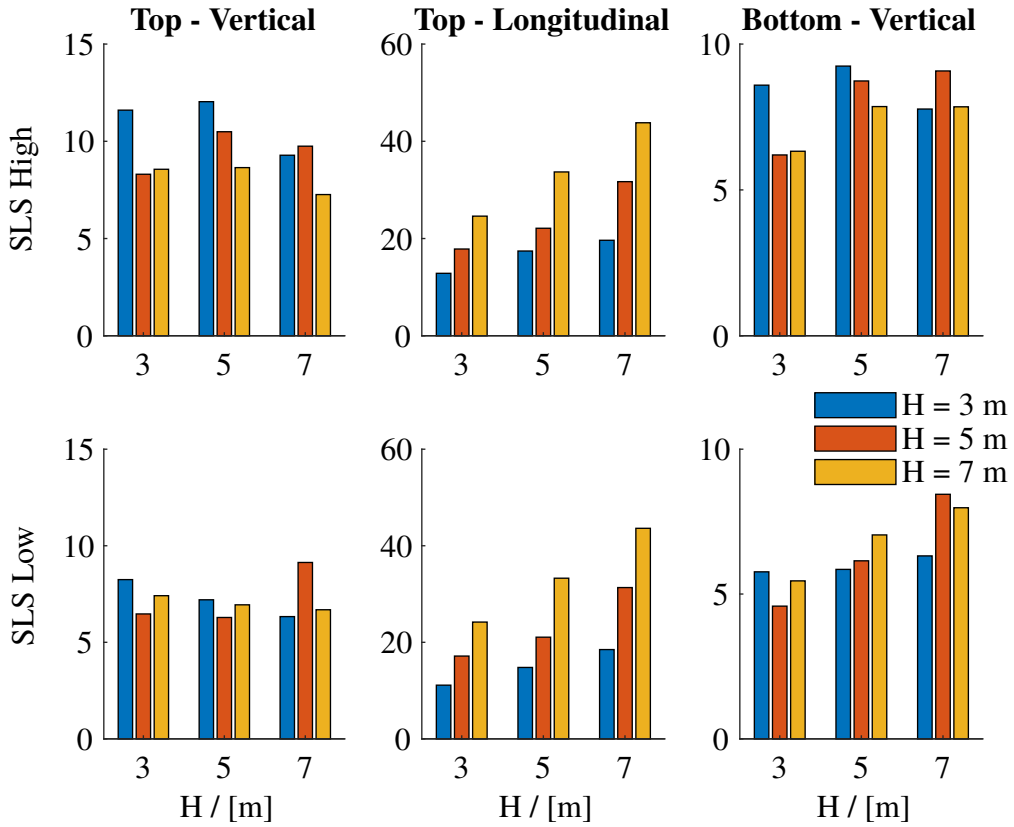

FIGURE 6.9: Bar diagram of mass steel per volume concrete $\left[\mathrm{kg}_{\mathrm{steel}}/\mathrm{m}^3_{\mathrm{concrete}}\right]$ *in the whole wing wall that originates from the total load combination SLS high and SLS low.*

In figure 6.11 the relative difference in the total required reinforcement in kg steel per cubic meter concrete $\left[\mathrm{kg/m}^3\right]$ is shown. For example, for wing wall $H = 3$ m $L = 3$ m the total required reinforcement from membrane forces in SLS high is approximately 3.5 times higher than the total required reinforcement form earth pressure.

There is a tendency for the vertical reinforcement at Top, that for increasing height and length of the wing walls, the relative difference in reinforcement is decreasing. This tendency is seen for both SLS high and SLS low. The same tendency is also applicable on the vertical reinforcement in the bottom.

Regarding the longitudinal reinforcement the above tendencies are not as easily distinguished. However, it can be noted that the total amount of required reinforcement due to membrane forces is always less than the total required reinforcement due to earth pressure.

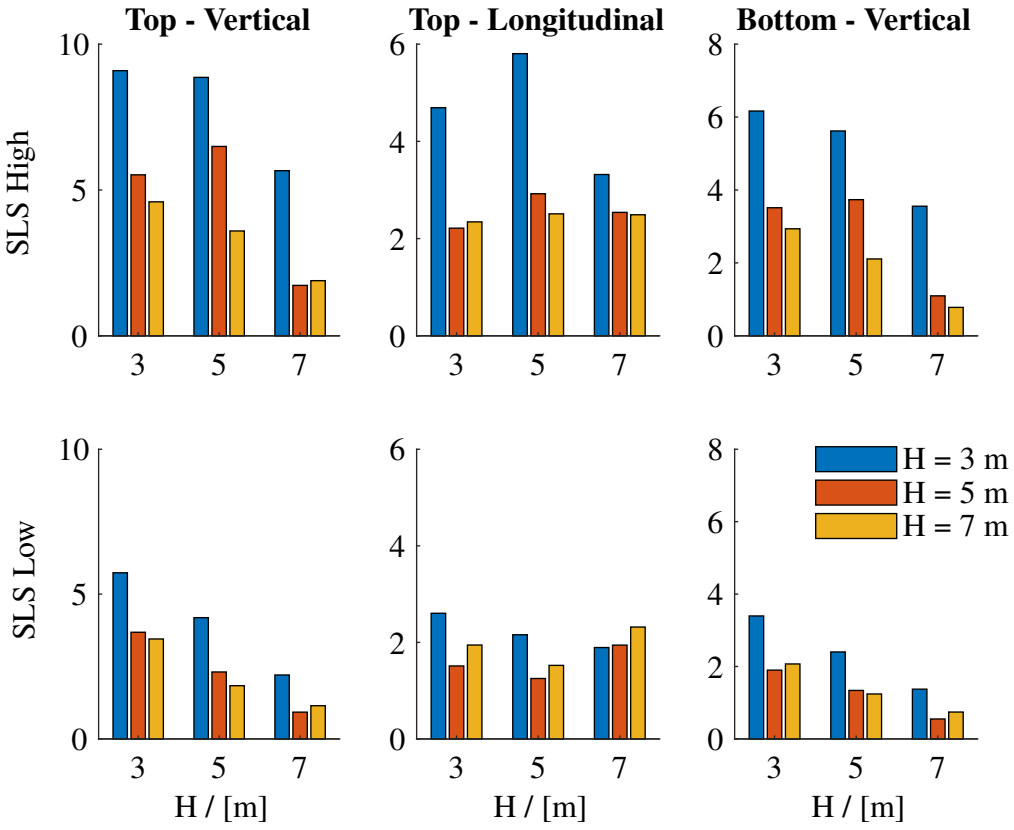

FIGURE 6.10: Bar diagram of mass steel per volume concrete $\left[\mathrm{kg_{steel}}/\mathrm{m^3_{concrete}}\right]$ *in the whole wing wall that originates from the membrane forces in the whole wing wall.*

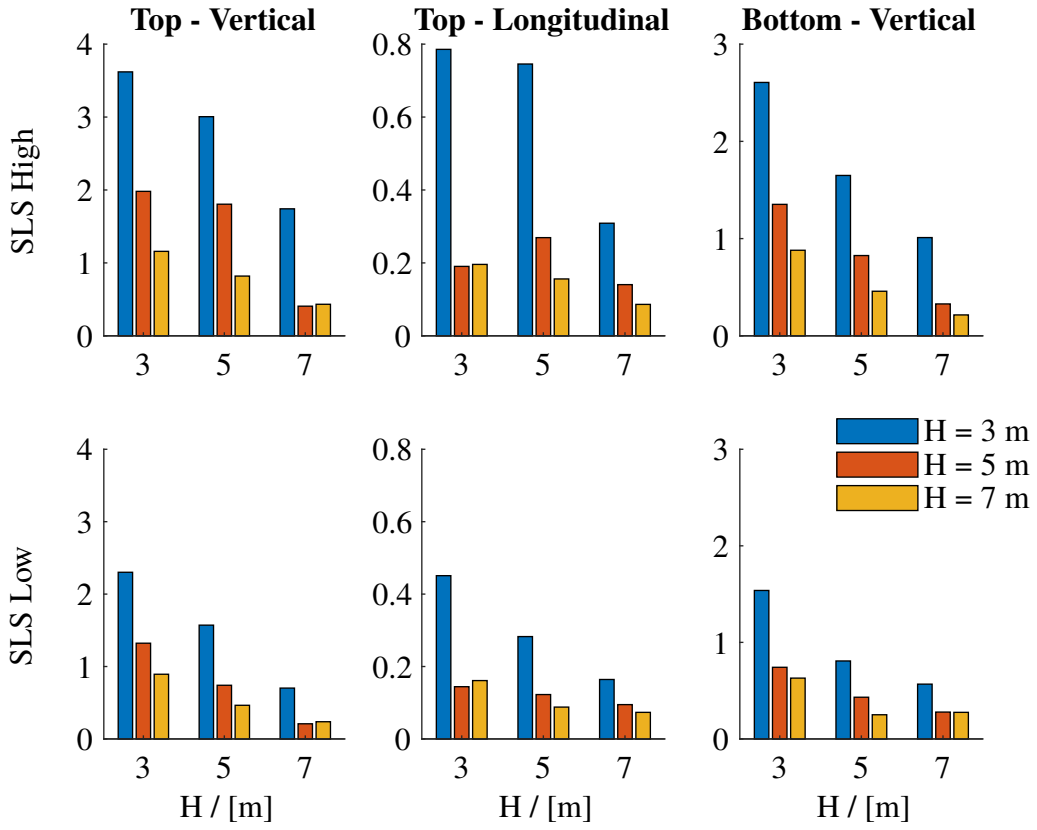

Figure 6.11: Bar diagram of the ratio between the required amount of reinforcement due to membrane forces and earth pressure, in the whole wing wall.

6.2 Non-linear analysis

The Non-linear analysis is performed for three different wing walls. In the analysis the reinforcement designed for only the earth pressure is used. In the results, figures show crack pattern and crack widths achieved with the non-linear model, along with max principal stress contour plots for the linear model. In the linear design it is seen that the load combination SLS high was more adverse than load combination SLS low, so the non-linear analysis is performed for the loads in load combination SLS high. A comparison between the global and local linear model is made to see the accuracy in transforming the loads from the global model to the local model. In the stress contour plots the crack safety factor is not used for the local linear model, to be able to compare the stresses. The characteristic tensile strength for concrete C35/45 is 2.2 MPa, so the wing wall is expected to crack in the green areas when considering the crack safety factor of 1.5.

From the linear design of the earth pressure load, the reinforcement implemented in the non-linear analysis is determined according to Table 6.1, with definitions in Table 5.4 and Figure 5.6. Note that ϕ_{H_1} and ϕ_{H_2} are overlapping each other from the frame leg edge to half the wing wall length.

Table 6.1: Amount of reinforcement for the wing walls analyzed in the non-linear analysis. Dimensions is presented in mm.

Wing wall	ϕ_{H_1} - s_{H_1}	ϕ_{H_2} - s_{H_2}	ϕ_{V} - s_{V}	ϕ_{S} - n_{S}	ϕ_{F} - n_{F}
H1L1	ϕ20s620	ϕ20s620	ϕ12s420	ϕ16 - 2 st	ϕ16 - 2 st
H2L1	ϕ20s400	ϕ20s400	ϕ12s280	ϕ16 - 2 st	ϕ16 - 2 st
H3L1	ϕ20s300	ϕ20s300	ϕ12s190	ϕ16 - 2 st	ϕ16 - 2 st

6.2.1 Wing wall H1L1

It can be seen in Figure 6.12 that the top values are close for the linear and global model, but that the contour pattern differs. It can also be noted that the effective area over the whole wing wall is in tension, but that the stress is below the tensile strength except at the corners. With the amplification from the crack safety factor applied in the nonlinear model the tensile strength will be reached for a bigger area and cracks are formed in the upper left corner.

The maximum crack width seen for wing wall H1L1 is 0.15 mm wide and below the requirements. One would expect a crack in the bottom left corner. However, the area with stresses higher than 2.2 MPa is smaller there than in the top left corner, which could explain that the results show that the crack width is lower than 0.05 mm.

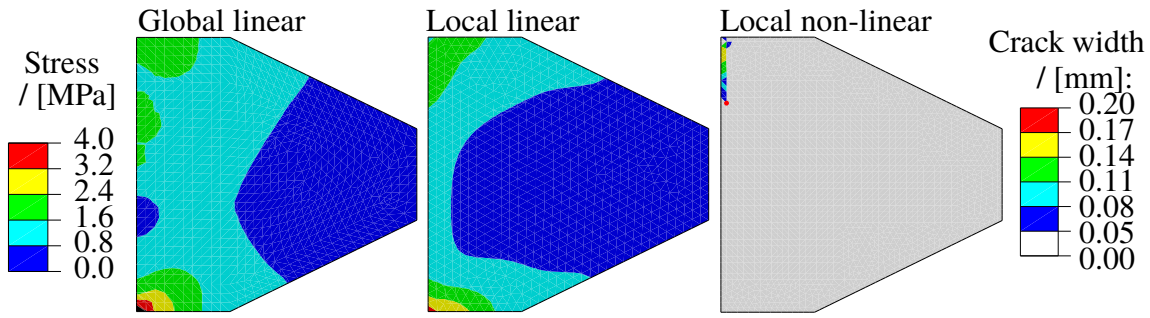

Figure 6.12: Max principal stress contour plot for global and local linear model, and crack pattern with crack width for non-linear local model.

6.2.2 Wing wall H2L1

For wing wall H2L1 it could be seen in Figure 6.13, that the top values match well but for the local model the area with stresses up to 0.8 MPa is bigger than for the global model. The top stress values are about the same as for wing wall H1L1, but there are bigger areas which are reaching the tensile strength of the concrete.

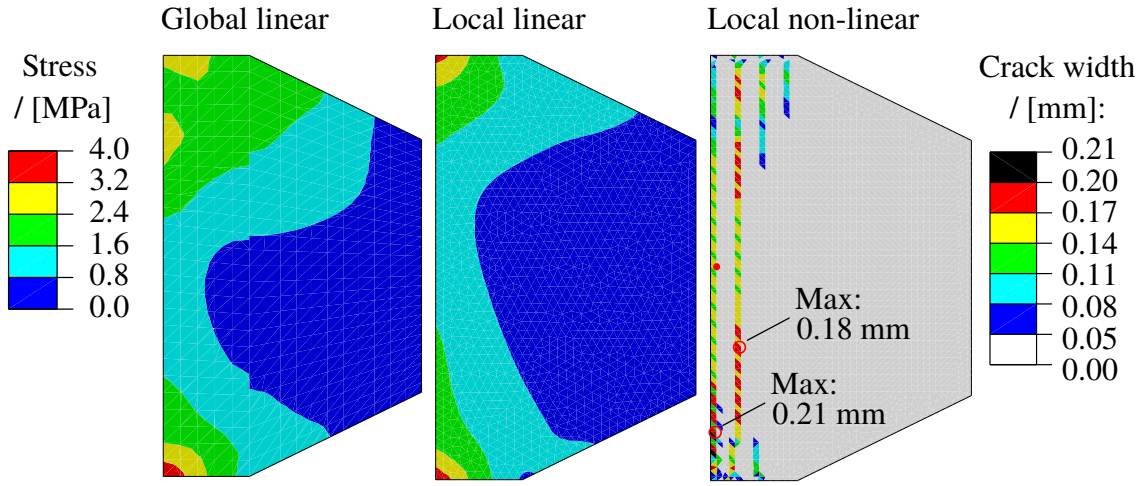

Figure 6.13: Max principal stress contour plot for global and local linear model, and crack pattern with crack width for non-linear local model.

It is noted in Figure 6.13 that there are two cracks going through the whole height of the wing wall. For the first crack at the intersection with the frame leg, the crack width is 0.21 mm and for the second crack the width is 0.18 mm. It is also seen that e.g. the second crack has a pattern, with lower crack width every third element. This pattern follows the distance between the longitudinal reinforcement bars. Except for the crack at the left edge the crack widths are close to the requirements but not exceeding them.

6.2.3 Wing wall H3L1

The contour plots for wing wall H3L1 is seen in Figure 6.14 for SLS high. The contours differ but are more similar at the bottom of the left edge. It is also seen that the top values are about the same as for the two other analyzed wing walls above in Figure 6.13 and Figure 6.12.

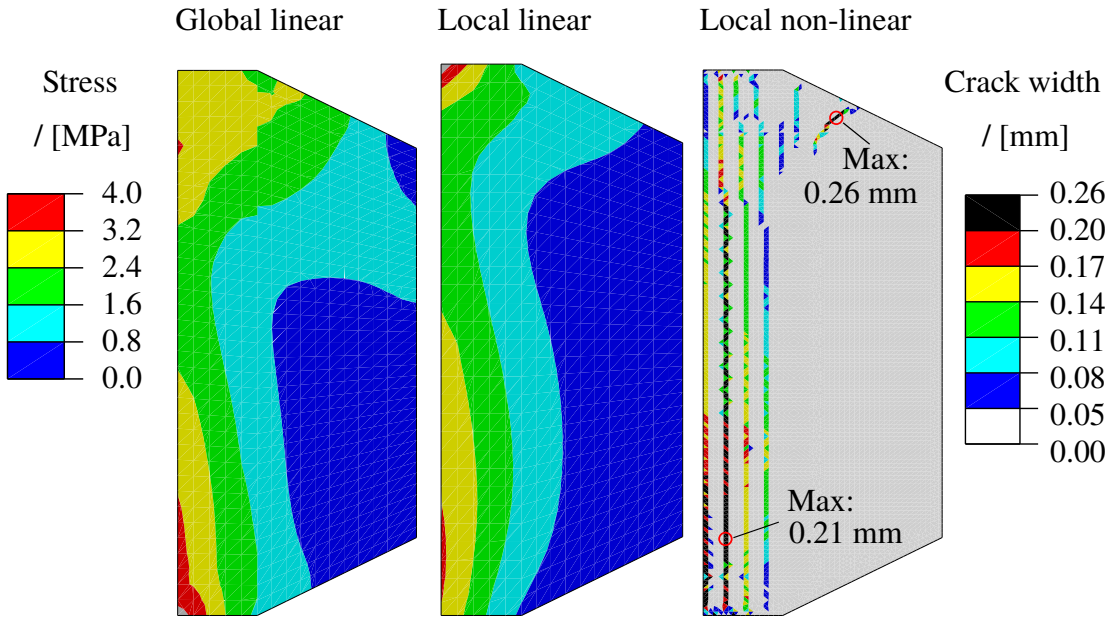

Figure 6.14: Max principal stress contour plot for global and local linear model, and crack pattern with crack width for non-linear local model.

In Figure 6.14 there are four cracks going through the whole height of the wing wall and also one wide inclined crack at the top right not seen in the other two wing walls. The inclined crack is 0.26 mm wide and it should be noted that it propagates where the longitudinal reinforcement is decreased to half the amount. The second largest crack is 0.21 mm wide, where it is as widest.

6.2.4 Comparison

To compare the three wing walls, their largest and second largest cracks are presented in Table 6.2. The requirement in the linear design was determined to 0.2 mm.

It is seen in Table 6.2 that the requirement is exceeded for wing wall H2L3 and H3L1. This could be expected, since the load from load combination SLS high is higher than for earth pressure, which the design of the used reinforcement is based on.

Table 6.2: Max crack widths for the largest and second largest crack.

Wing wall	Largest crack	2:nd largest crack
H1L1	0.15 mm	< 0.05 mm
H2L1	0.21 mm	0.18 mm
H3L1	0.26 mm	0.21 mm

7 Discussion

7.1 Linear design

The required reinforcement from the membrane forces is defined as the difference in the required reinforcement for the entire load combination SLS and for the earth pressure as defined below.

$$A_{SLS} - A_{ep} = A_{membrane} \tag{7.1}$$

This basically means that the only load that is acting directly on the wing wall is the earth pressure. This is however not the entire truth. The self-weight is also present. The self-weight will result in longitudinal reinforcement in the top corner of the wing wall and this will have an increasing effect on the longer and lower wing walls. The self-weight was however neglected but in retrospect it would make the results more precise if the self-weight was to be included.

It must also be noted that the temperature is also acting directly on the wing wall. However, the expansion coefficient for steel and concrete is close to equal and hence the temperature load directly on the wing wall is neglected. However, for the shrinkage it is different since it is only acting on the concrete. The shrinkage acting directly on the wing wall has though also been neglected. The reason for this was to make the calculations faster.

It should also be noted that the global FE-model has its approximations regarding modeling of supports and connections between the different structural parts. Different designers would make different choices for this and another result could be obtained. Also a FE-model will not be exactly the same as the reality, whatever the choices are made.

7.2 Non-linear analysis

When modeling the wing wall non-linearly the goal is basically to achieve the exact same stresses in the local wing wall as in the global model. This is checked by introducing a linear local model with the same applied loads that are applied in the non-linear model. The differences are illustrated in Section 6.2 and it is clear that the stresses do not correlate exactly.

One thing that can affect this is the surface function of the stresses from the earth pressure and the function of the deformation pattern. These functions are approximated with regard to the data points extracted from the global model. However, it is just an approximation and some of the information is lost. Also the deformation pattern only considers deformations in the wing wall's plane. The deformation out of plane at the frame leg intersection could cause bending and thereby stresses which are not considered in the non-linear local model.

The crack safety factor of 1.5 introduced to the loads in the non-linear analysis contributes to cracks in areas where the stress would not exceed the tensile strength without the factor. However the cracks will become wider due to the factor and this is not the purpose of the crack safety factor. But to achieve conservative results and since the approximations introduced in the local model give lower stresses than in the global model, it was decided to be applied to the loads anyway. It is therefore estimated that the crack width is overestimated for the non-linear analysis of the wing walls.

The verification of the non-linear FE model showed that the model has some difficulties with predicting the crack width. The results were conservative for the lower load with about twice the crack width, but for failure load the crack width was underestimated as seen in Table 4.3. The failure load for the FE-model were lower than in the experiment, which could explain that the crack width is underestimated for the failure load.

The SLS combinations used in the non-linear analysis for the wing walls are below the failure load so one could argue for that the non-linear model will rather overestimate the crack width than underestimate it. Also, there are more reinforcement, controlling the crack widths, in the wing wall analysis than for the ACI experiment, which would decrease the variation and difference in crack width.

It was seen in the analysis that the crack widths were changing with element sizes and a comprehensive study of this for the wing walls would be needed to ensure high reliability for the results.

8 Final remarks

In this chapter the final remarks of the report are presented. The first section summarizes the conclusions of the report. The second section presents suggestions for further studies.

8.1 Conclusions

The purpose of this report is to investigate the impact of membrane forces when designing wing walls. One part of the report focuses on how the membrane forces behave for different height and length of the wing wall. This is analyzed with linear FE models. Another part of the report focuses on how great impact the membrane forces has on the cracking of the wing wall. This is mainly treated with non-linear FE models. The conclusions of this report are summarized below.

To make the final remarks easier to follow some denotes are defined.

Critical area	Area that enclosure the top 10 % highest demand of reinforcement.
$A_{\mathrm{m,top10\%}}$	Amount of required reinforcement caused by membrane forces in the critical area [mm^2/m]
$A_{\mathrm{ep,top10\%}}$	Amount of required reinforcement caused by earth pressure in the critical area [mm^2/m]
$A_{\mathrm{m,top10\%rel}}$	The ratio of the amount of required reinforcement caused by membrane forces and earth pressure. $A_{\mathrm{m,top10\%rel}} = \frac{A_{\mathrm{m,top10\%}}}{A_{\mathrm{ep,top10\%}}}$ [-]
$A_{\mathrm{m,tot}}$	Amount of required reinforcement caused by membrane forces over the entire area. $[\mathrm{kg_{steel}/m^3_{conc}}]$
$A_{\mathrm{ep,tot}}$	Amount of required reinforcement caused by earth pressure over the entire area. $[\mathrm{kg_{steel}/m^3_{conc}}]$
$A_{\mathrm{m,totrel}}$	The ratio of the amount of required reinforcement caused by membrane forces and earth pressure over the entire win wall. $A_{\mathrm{m,totrel}} = \frac{A_{\mathrm{m,tot}}}{A_{\mathrm{ep,tot}}}$ [-]

- Based on all the plots in Appendix D it can be noted that the membrane forces mainly cause a need for reinforcement in the corners for the longitudinal direction.

- For the critical area in the wing wall there is a tendency that the absolute amount of required vertical reinforcement caused by membrane forces, $A_{\mathrm{m,top10\%}}$, is decreasing with constant height and increasing length. This is in accordance with Figure 6.7.
- For the critical area in the wing wall there is a tendency that the relative amount of required reinforcement caused by the membrane forces, $A_{\mathrm{m,top10rel\%}}$, decreases with increasing height and length. This tendency is true for both longitudinal and vertical reinforcement. This is in accordance with Figure 6.8.
- There is no clear relationship regarding the total amount of longitudinal reinforcement caused by membrane forces, $A_{\mathrm{m,tot}}$, and the geometry of the wing wall. This is in accordance with Figure 6.10.
- The total relative amount of required reinforcement caused by membrane forces, $A_{\mathrm{m,totrel}}$, is decreasing with increasing length and height. This is in accordance with Figure 6.11.
- If the wing wall is to be designed for only earth pressure there must be extra amount of attention regarding shorter wing walls. $A_{\mathrm{m,top10\%}}$ is increasing for shorter wing walls. For longer wing walls the earth pressure gets more dominant in relation to the membrane forces and hence the membrane forces make less of difference.
- The main cause of the membrane forces in the wing wall is the deformation of the frame leg. The deformation of the frame leg varies with the load on the bridge and the stiffness of the frame leg where the wing wall is connected. In the critical area of the wing wall the absolute amount of reinforcement caused by membrane forces, $A_{\mathrm{m,top10\%}}$, clearly increases for constant height and decreasing length. This indicates that the length of the wing wall is important regarding the stiffness of the frame leg. The longer the wing wall is, the stiffer the frame leg gets and hence, less membrane forces arise in the wing wall.
- From the linear design of wing wall H1L1 it was seen in Figure 6.2 that the membrane forces would contribute to more reinforcement. However, the non-linear analysis shows in Figure 6.12 that the crack width requirement is not exceeded for load combination SLS high when using reinforcement designed for only earth pressure. This could indicate that the membrane forces are not a problem for shorter wing walls. But for the higher wing wall H3L1, the opposite is found.
- In wing wall H3L1, Figure 6.14, the cracks are too wide compared with the requirement of 0.2 mm crack width. From the linear design it could be seen in Figure 6.6 that the membrane forces would lead to higher amount of reinforcement at the top edge and in the bottom left corner. It is in these areas too wide cracks were found in the non-linear analysis, see Figure 6.14. This would indicate that there is a problem with the membrane forces. However, this is only the result from two wing walls and more wing walls should be analyzed.

- The validation of the nonlinear FE model showed good accuracy for the crack spacing and conservative crack widths for lower loads. The model showed difficulties predicting crack widths for the brittle shear failure and underestimates the crack width. A dilation angle of $\psi = 38°$ and a fracture energy of $G_f = 141.8$ J showed best correlation with the ACI deep beam experiment.
- The nonlinear analysis is not enough comprehensive to be able to conclude if the membrane forces cause wider cracks and therefore need to be considered.

8.2 Further research

To fully determine whether the membrane forces causes problem in SLS there needs to be conducted a more extensive parametric study. For example, the parametric study can be extended to include more parameters. This report has only treated the length and height of the wing wall. Some other parameters that can be checked are:

- Angle of the wing wall.
- Thickness of the wing wall.
- Slope of the wing wall.
- Different geometries of the bridge.

Further study can also be conducted regarding the local FE model. In chapter 6.2 it is stated that the global model do not absolutely correspond to the local linear model. Here is room for improvement to make the local model behave more similar to the global model.

The stiffness of the wing walls decreases when cracks occur in the wing walls. This stiffness reduction and how this affects the membrane forces could be studied further for different wing wall geometries and slab frame bridges.

Bibliography

Abaqus (2011). *Abaqus theory manual*. Dassualt Systèmes, Providence, RI, USA.

Balazs, György and Adorjan Borosnyói (2003). "Bond between reinforcement and concrete - A survey of characteristics and trends of its development". In: Konferencija Savremena gradevinska praksa.

Bangash, M. Y. H. (2001). *Manual of numerical methods in concrete Modelling and applications validated by experimental and site-monitoring data*. London : Thomas Telford Publishing.

Bažant, Zdeněk and B. Oh (1983). "Crack band theory for fracture of concrete." In: *Materiaux et Constructions* 16.3, p. 155. ISSN: 00255432.

Björnström, Jonas, Tomas Ekström, and Manouchehr Hassanzadeh (2006). *Spruckna betongdammar : översikt och beräkningsmetoder.* Elforsk rapport: 06:29. Stockholm : Elforsk, [2006].

CEN (2004). *Eurocode 2: Design of concrete structures*. European Committee for Standardization, Brussels.

Chen, Wai-Fah (1982). *Plasticity in reinforced concrete.* New York : McGraw-Hill, cop. 1982. ISBN: 0070106878.

Collins, P et al. (2015). "The Challenge of Predicting the Shear Strength of Very Thick Slabs". In: *Concrete International* 37, pp. 29–37.

Cornelissen, HAW, DA Hordijk, and HW Reinhardt (1986). "Experimental determination of crack softening characteristics of normalweight and lightweight". In: *Heron* 31.2, p. 45.

Engström, Björn (2011). *Restraint cracking of reinforced concrete structures*. Göteborg: Gothenburg : Chalmers University of Technology.

Fédération internationale du béton, Task Group 2.5 - Bond Models (2000). *Bond of reinforcement in concrete : state-of-art report*. "August 2000." Lausanne, Switzerland : International Federation for Structural Concrete. ISBN: 2883940487.

Hillerborg, A., M. Modéer, and P.-E. Petersson (1976). "Analysis of crack formation and crack growth in concrete by means of fracture mechanics and finite elements". In: *Cement and Concrete Research* 6.6, pp. 773–781. ISSN: 0008-8846.

Hillerborg, Arne (1983). "Analysis of one single crack". eng. In: ed. by Folker H. Wittmann. Fracture Mechanics of Concrete (Developments in civil engineering). Elsevier, pp. 223–249. ISBN: 0-444-42199-8.

– (1985). "The theoretical basis of a method to determine the fracture energy GF of concrete." In: *Materials and Structures / Materiaux et Constructions* 106, p. 291. ISSN: 1359-5997.

Ian Gilbert, R. (2007). "Tension Stiffening in Lightly Reinforced Concrete Slabs." In: *Journal of Structural Engineering* 133.6, pp. 899–903. ISSN: 07339445.

Karihaloo, B. (2003). "2.10 - Failure of Concrete". In: *Comprehensive Structural Integrity*. Ed. by I. Milne, R.O. Ritchie, and B. Karihaloo. Oxford: Pergamon, pp. 477–548. ISBN: 978-0-08-043749-1.

Krenk, Steen (2009). *Non-linear modeling and analysis of solids and structures. [Elektronisk resurs]*. Cambridge : Cambridge University Press, 2009. ISBN: 9780511602573.

Kwak, HYO-GYOUNG and Filip Filippou (1990). "Finite element analysis of reinforced concrete structures under monotonic loads". In:

Lee, Jeeho and Gregory L. Fenves (1998). "Plastic-damage model for cyclic loading of concrete structures." In: *Journal of Engineering Mechanics* 124.8, p. 892. ISSN: 07339399.

Lubliner, J. et al. (1989). "A plastic-damage model for concrete". In: *International Journal of Solids and Structures* 25.3, pp. 299–326. ISSN: 0020-7683.

Lutz, L.A (1970). "Analysis of Stresses in Concrete near a Reinforcing Bar Due to Bond and Transverse Cracking." In: *ACI Journal* 67, pp. 778–787.

Malm, Richard (2006). *Shear cracks in concrete structures subjected to in-plane stresses.* Trita-BKN: Bulletin 88. Stockholm, 2006.

Model Code 10, fib (2012). *CEP-FIP model code 2010*. Bulletin / Fédération internationale du béton: 65. Lausanne : FIB, 2012. ISBN: 9782883941052.

Model Code 90, fib (1990). *CEB-FIP model code 1990*. Bulletin d'information / Comité euro-international de béton: 195. Lausanne: CEB, 1990. ISBN: 2883940096.

Myrefelt, Per-Henrik and Martin Roswall (1994). *Styvhetseffekter av vingmurar : en studie utförd med BRIGADE - ett nytt dimensioneringssytem för broar*. Examensarbete. Lund.

Ngo, D. and A.c. Scordelis (1967). "Finite Element Analysis of Reinforced Concrete Beams". In: *ACI Journal* 64, pp. 152–163.

Plos, Mario (1996). *Finite element analysis of reinforced concrete strucutres*. Gothenburg: Department of strucutral enginering, Chalmers University of Tecknology.

Rashid, Y.R. (1968). "Ultimate strength analysis of prestressed concrete pressure vessels". In: *Nuclear Engineering and Design* 7.4, pp. 334–344. ISSN: 0029-5493.

Rehm, G. (1961). *Ueber die Grundlagen des Verbundes zwischen Stahl und Beton (On the Basic Laws of Bond Between Steel and Concrete)*. German. Berlin: Schriftenreihe des Deutschen Ausschusses fuer Stahlbeton : Berling.

Rots, J.G. and J. Blaauwendraad (1989). *Crack Models for Concrete: Discrete Or Smeared? Fixed, Multi-Directional Or Rotating?* Faculty of Civil Engineering, Delft University of Technology : Delft.

Suidan, M. and W. Schnobrich (1973). "Finite element analysis of reinforced concrete." In: *J. Struct. Div.* 99, pp. 2109–2122.

Sundquist, Håkan (2008). *Infrastructure structures*. Stockholm: Civil and Architectural Engineering, Kungliga Tekniska högskolan (KTH).

Trafikverket (2008). "Kodförteckning och beskrivning av Brotyper". In: URL: `https://batman.trafikverket.se/batinfo/Batman/BiblioteketPDF/01_Dokument%20Batman/Kodfoerteckning%20och%20beskrivning%20av%20brotyper.pdf`.

– (2011a). *Trafikverkets föreskrifter om ändring i Vägverkets föreskrifter (VVFS 2004:43) om tillämpningen av europeiska beräkningsstandarder*. Swedish. Trafikverket, Borlange.

– (2011b). *TRVR Bro 11*. Swedish. Trafikverket, Borlange.

Zhao, Zhifang, Seung Hee Kwon, and Surendra P. Shah (2008). "Effect of specimen size on fracture energy and softening curve of concrete: Part I. Experiments and fracture energy." In: *Cement and Concrete Research* 38, pp. 1049–1060. ISSN: 0008-8846.

A Bridge drawing

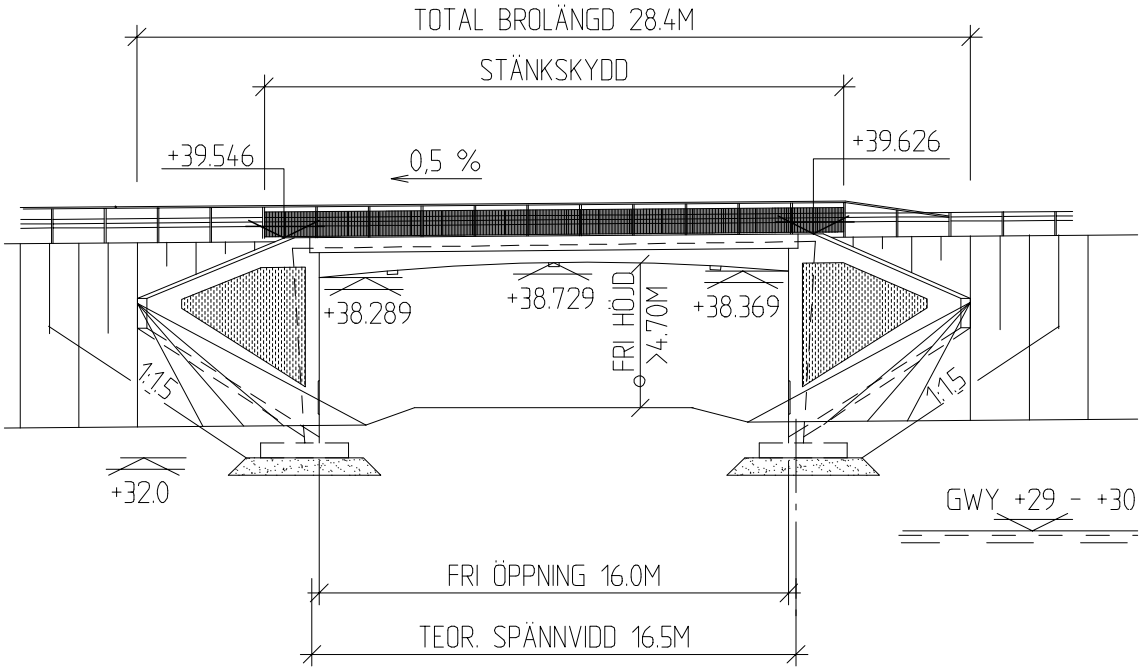

Figure A.1: Elevation of analyzed bridge.

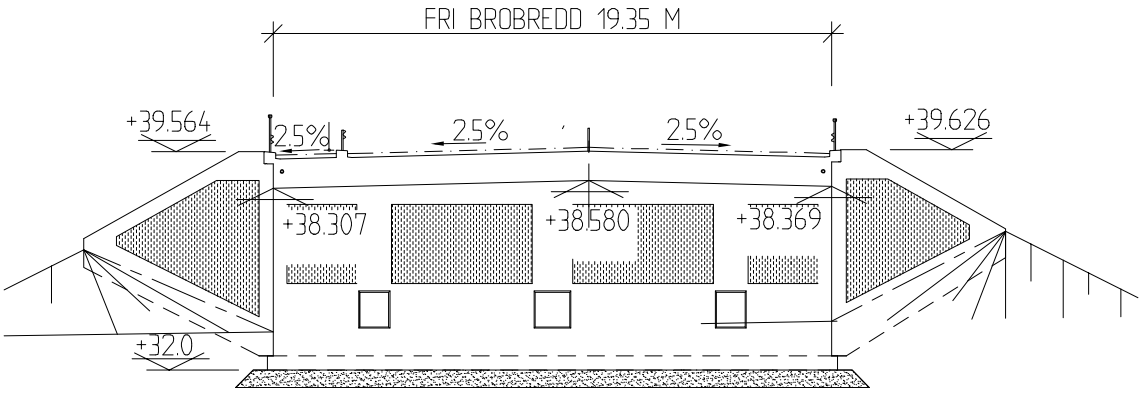

Figure A.2: Section of analyzed bridge.

B Crack patterns for convergence study

B.1 Dilation angle

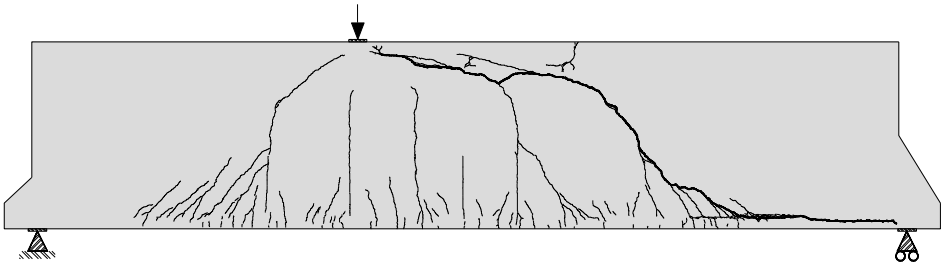

(A) Crack pattern for experiment

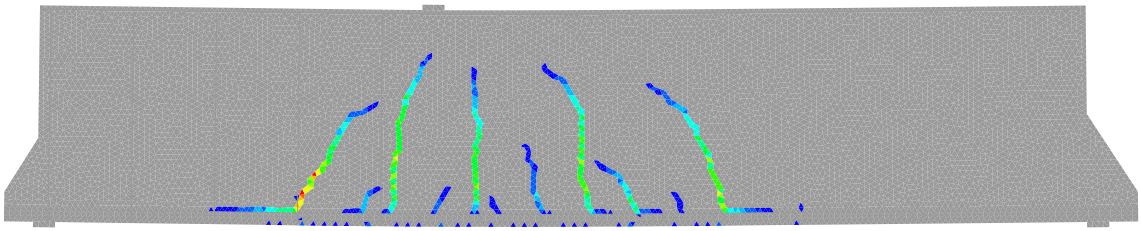

(B) Crack pattern for $\psi = 30°$

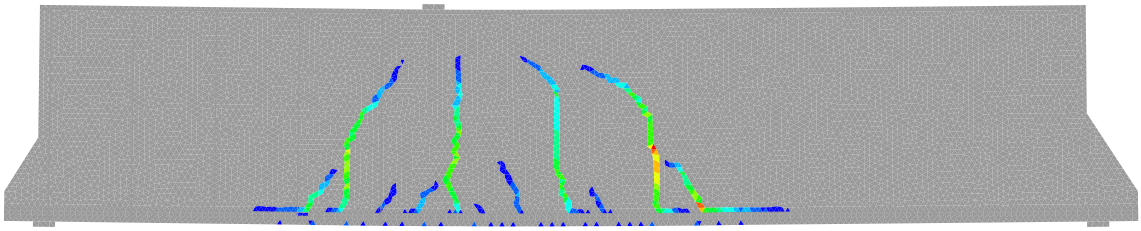

(C) Crack pattern for $\psi = 35°$

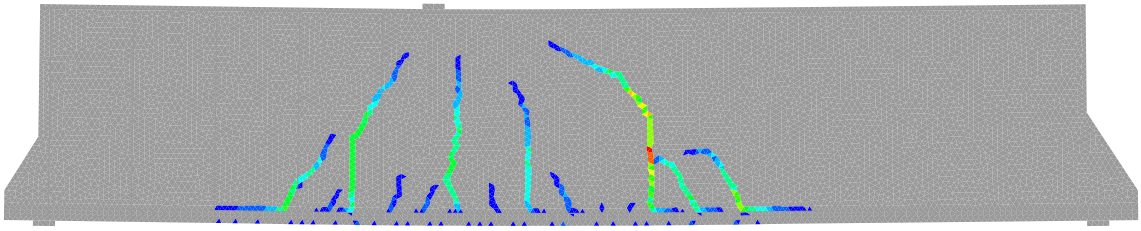

(D) Crack pattern for $\psi = 38°$

FIGURE B.1: Illustrations for crack patterns at failure for different dilation angles and for the ACI experiment.

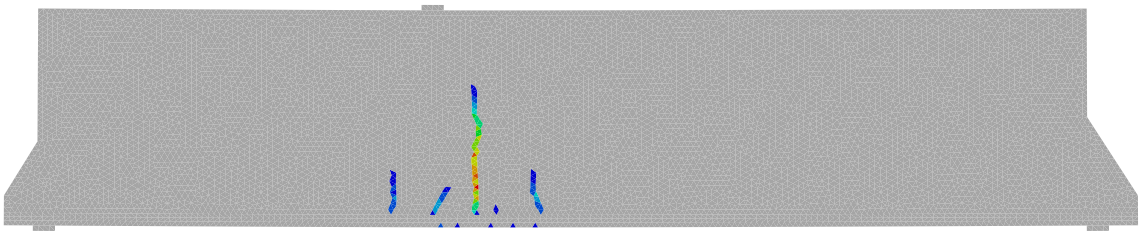

(A) Crack pattern for $\psi = 30°$

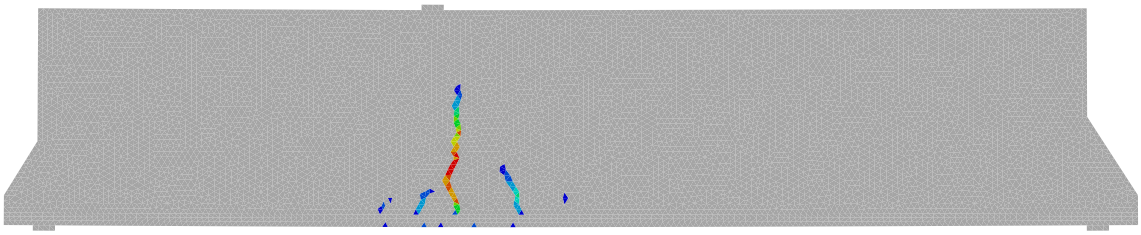

(B) Crack pattern for $\psi = 35°$

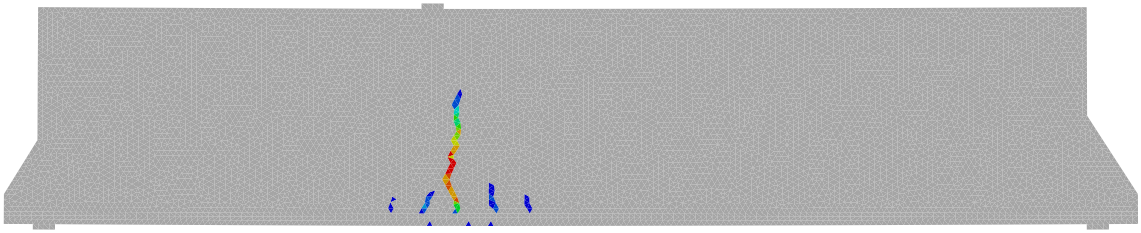

(C) Crack pattern for $\psi = 38°$

FIGURE B.2: Illustrations for crack patterns at $P = 375$ *kN for different dilation angles and for the ACI experiment.*

B.2 Fracture energy

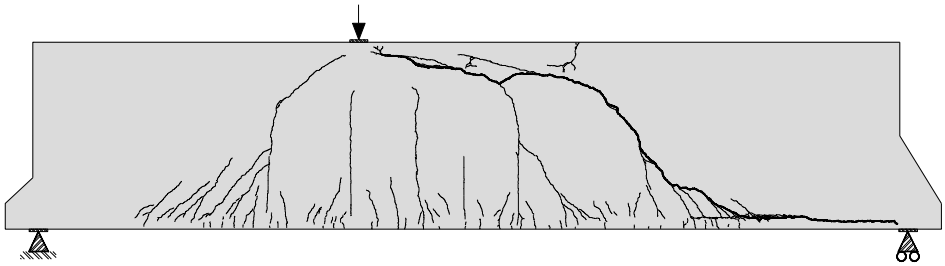

(A) Crack pattern for experiment

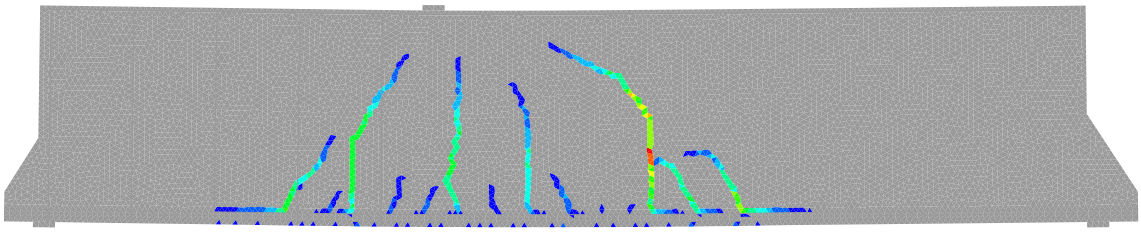

(B) Crack pattern for G_f=141.8 Nm/m^2

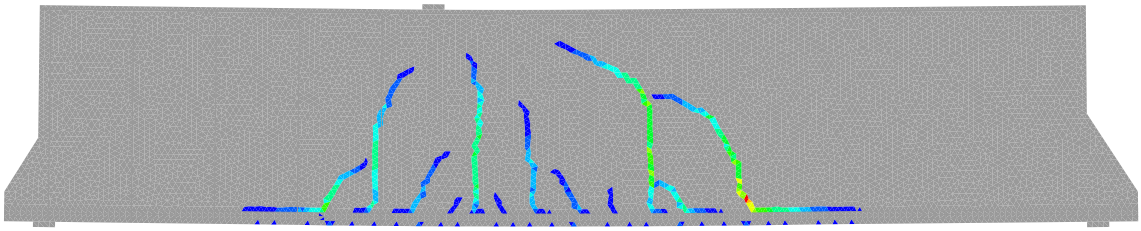

(C) Crack pattern for G_f=85 Nm/m^2

FIGURE B.3: Illustrations for crack patterns at failure for different fracture energies and for the ACI experiment.

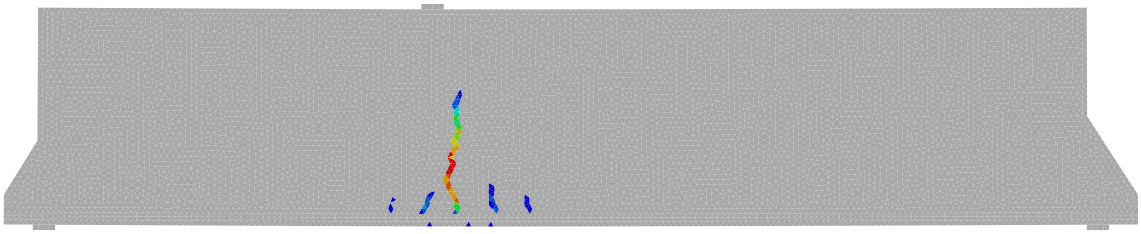

(A) Crack pattern for G_f=141.8 Nm/m^2

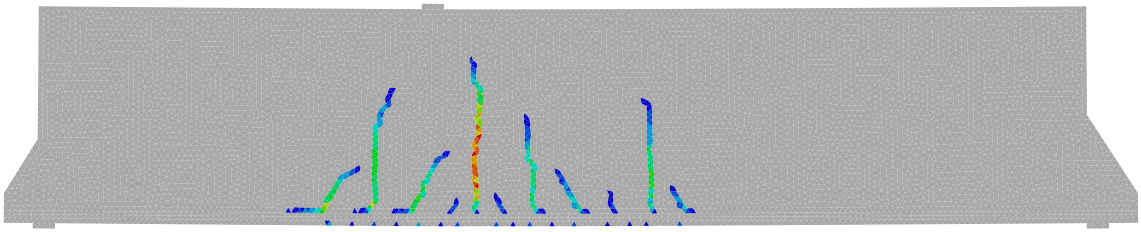

(B) Crack pattern for G_f=85 Nm/m^2

FIGURE B.4: Illustrations for crack patterns at $P = 375$ kN for different fracture energies.

C Pre-conditions

Pre-conditions for both Bridge 1 and Bridge 2.

C.1 Genereal pre-conditions

Foundation +32.0 m

Gravel +32 - +31.4

Silt +31.4 - +29.0 E_k= 23 Mpa, ϕ=33, λ=19 kN/m^3, λ'=11 kN/m^3

Moraine +29 E_k= 40 Mpa, ϕ=38, λ=19 kN/m^3, λ'=12 kN/m^3

Concrete C35

C.2 Permanent loads

TABLE C.1: Permanent loads

Load	Value	Unit
Self weight concrete	24	kN/m^3
Surfacing	3.24	kN/m^2
Railing (on edge beam)	0.5	kN/m

C.3 Earth loads

Filling soil γ_k/γ'_k= 22/12 kN/m^3

Angle of friction ψ=45

coefficient of lateral earth pressure K_0=0.39

C.4 Creep

Creep according to EC2-1-1

Reduction factor short term $a_{c,short}$=0.79

Reduction factor long term $a_{c,long}$=0.42

Coefficient of deformation f=2.655

C.5 Shrinkage

Total shrinkage $\varepsilon_{cd} + \varepsilon_{ca} = 1.665 \cdot 10^{-}4 + 6.25 \cdot 10^{-}5 = 2.29 \cdot 10^{-}4$

Equivalent temperature difference $\Delta T = -22.93°$

C.6 Rotational stiffness

$k_{\theta,weak} = 0.867$ GNm/rad

$k_{\theta,stiff} = 5.711$ GNm/rad

C.7 Support yield

Horizontal and vertical yield of 10 mm according to TRVR Bro 11, B.3.1.4.3.

C.8 Temperature

According to EK1-1-5.

$T_{e,max} = 35°$

$T_{e,min} = -15°$

$T_0 = 10°$

$\Delta T_{M,heat} = 10.5°$

$\Delta T_{M,heat} = -8°$

Increased earth pressure due to temperature. Assumed triangular load. Maximum pressure Δp=27.172 kN/m^3.

D Reinforcement requirement plots

Plots of need of reinforcement are shown below. Here all the wing walls are shown that concerns the master thesis.

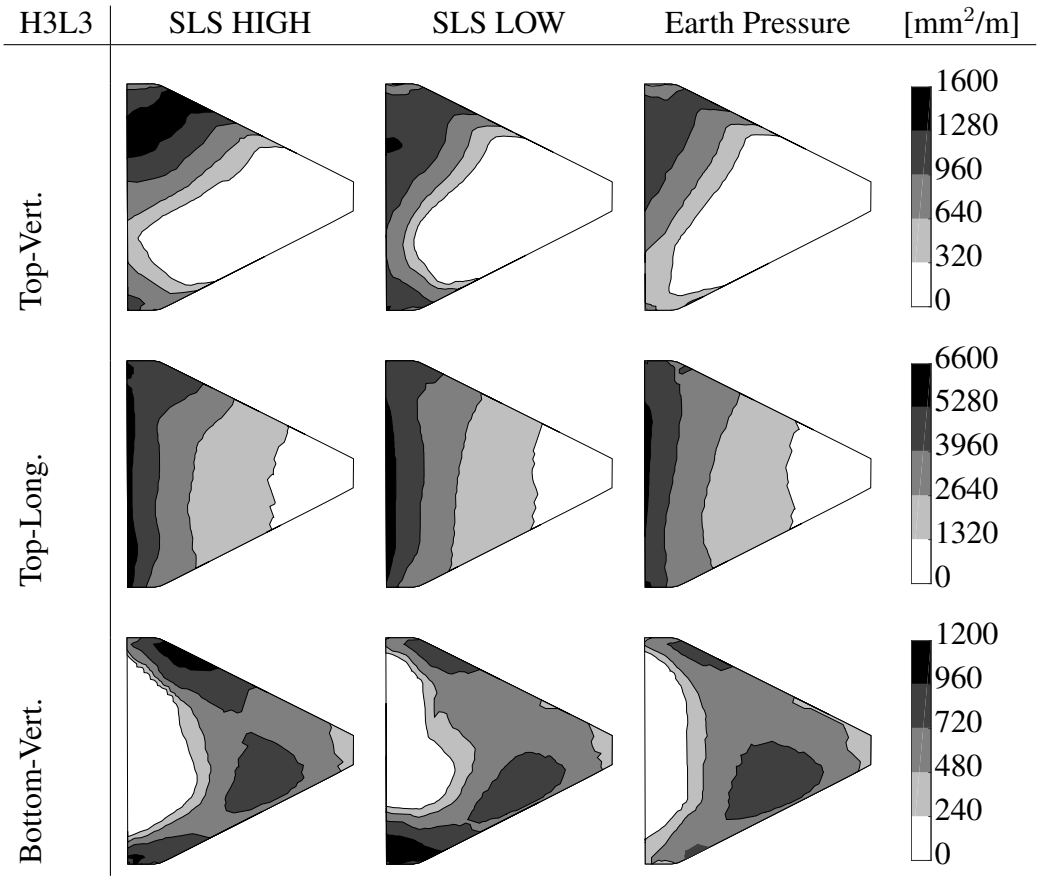

FIGURE D.1: Longitudinal and vertical reinforcement for top and bottom side of wing wall H3L3.

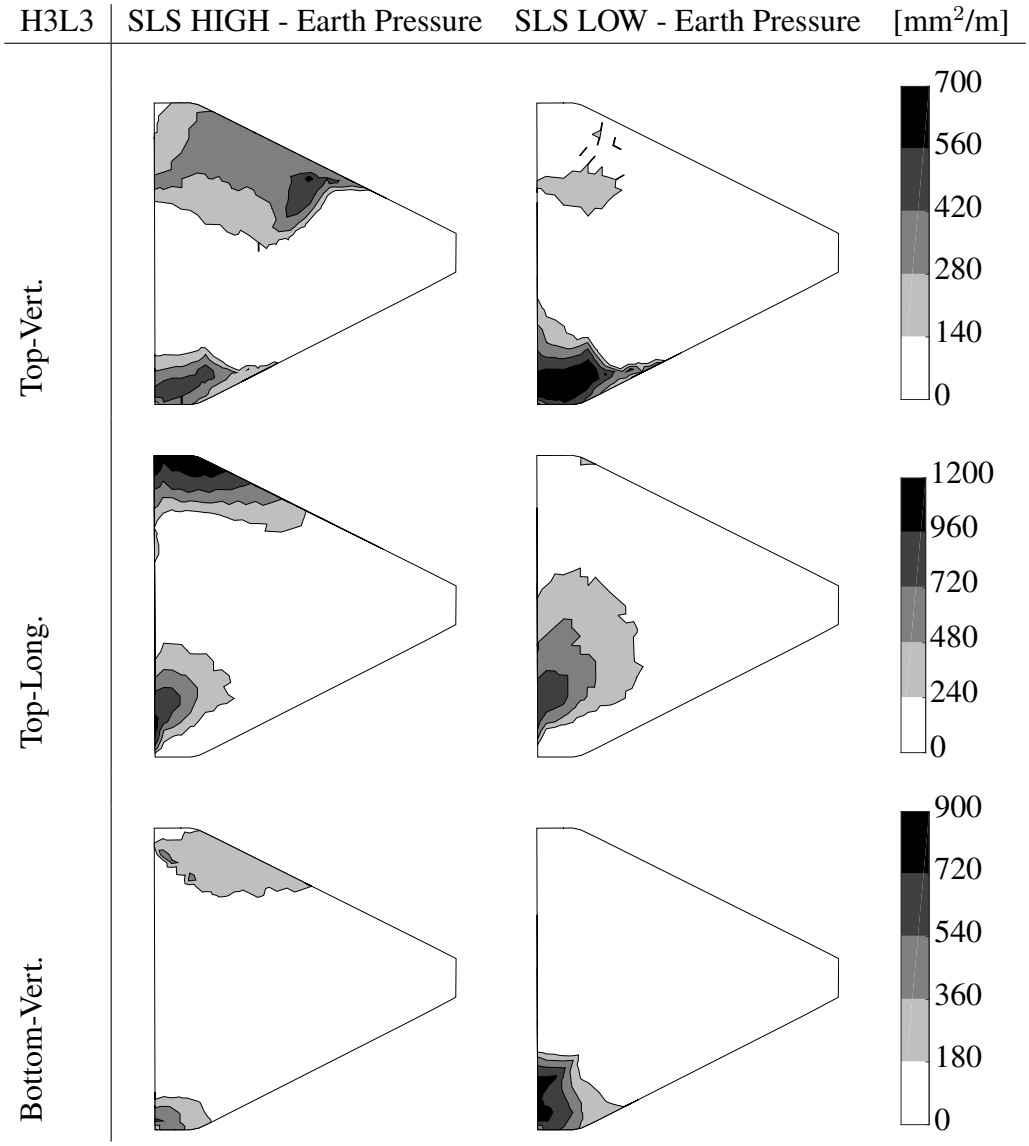

FIGURE D.2: Reinforcement caused by only membrane forces for H3L3.

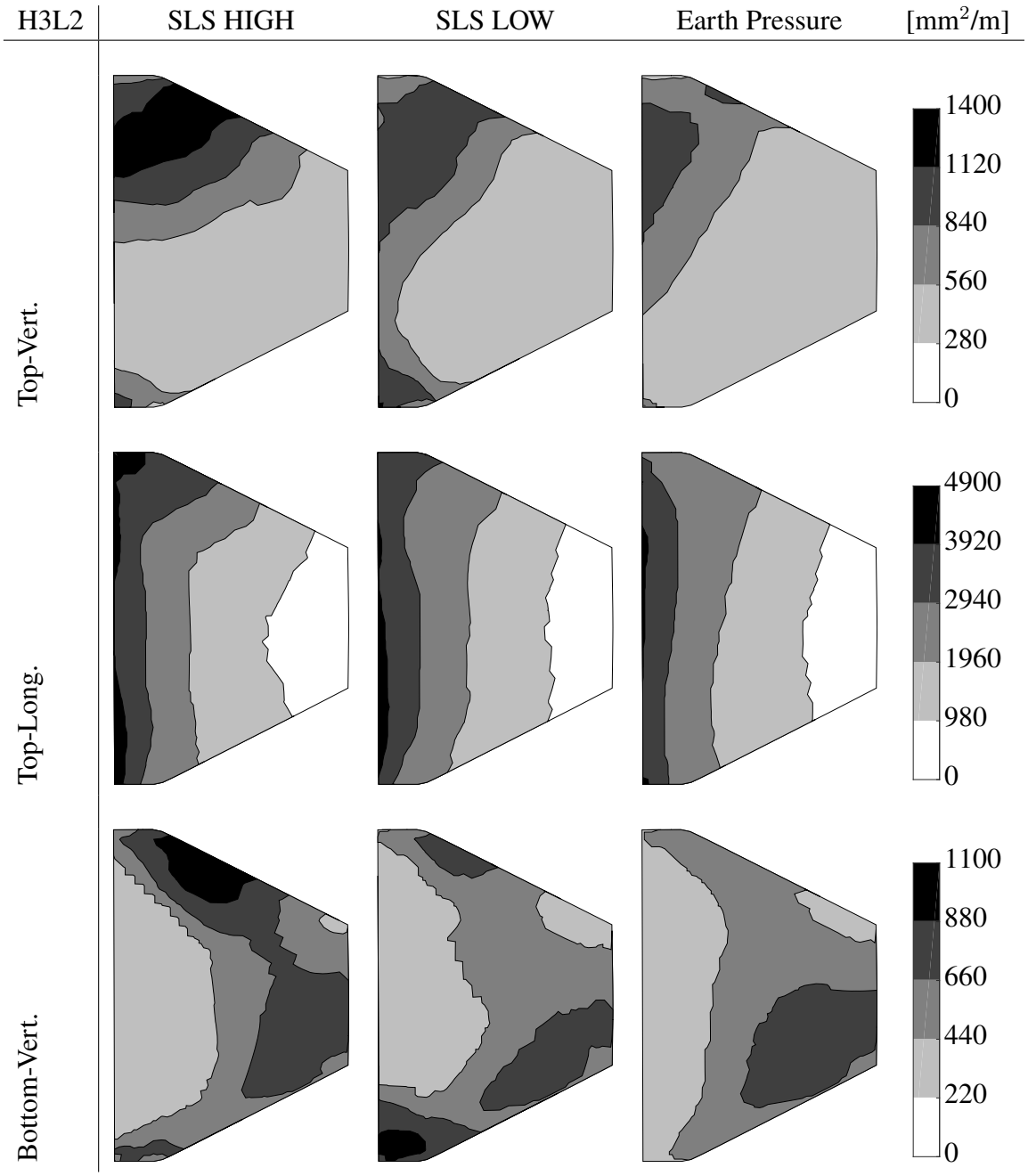

FIGURE D.3: Longitudinal and vertical reinforcement for top and bottom side of wing wall H3L2.

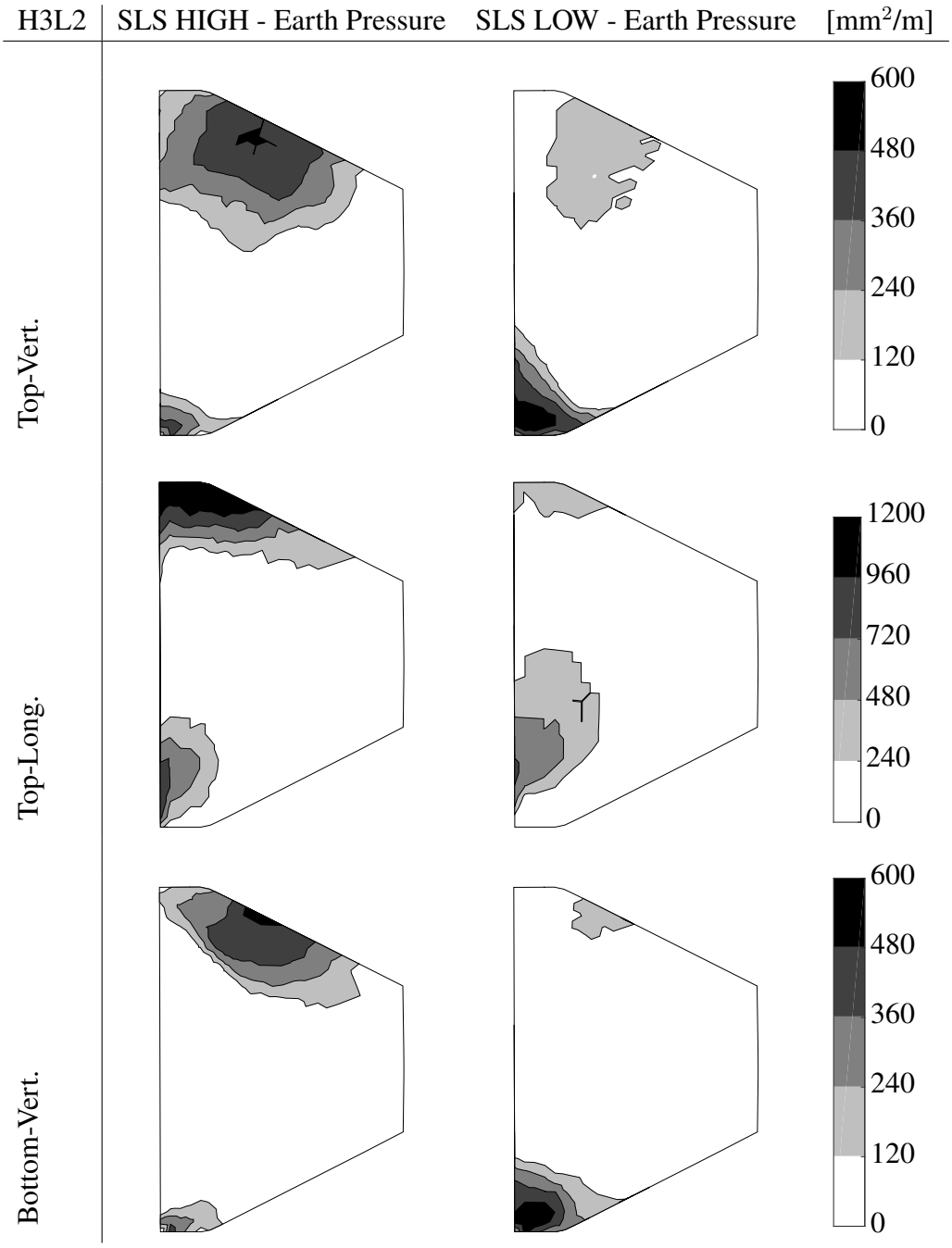

FIGURE D.4: Reinforcement caused by only membrane forces for H3L2.

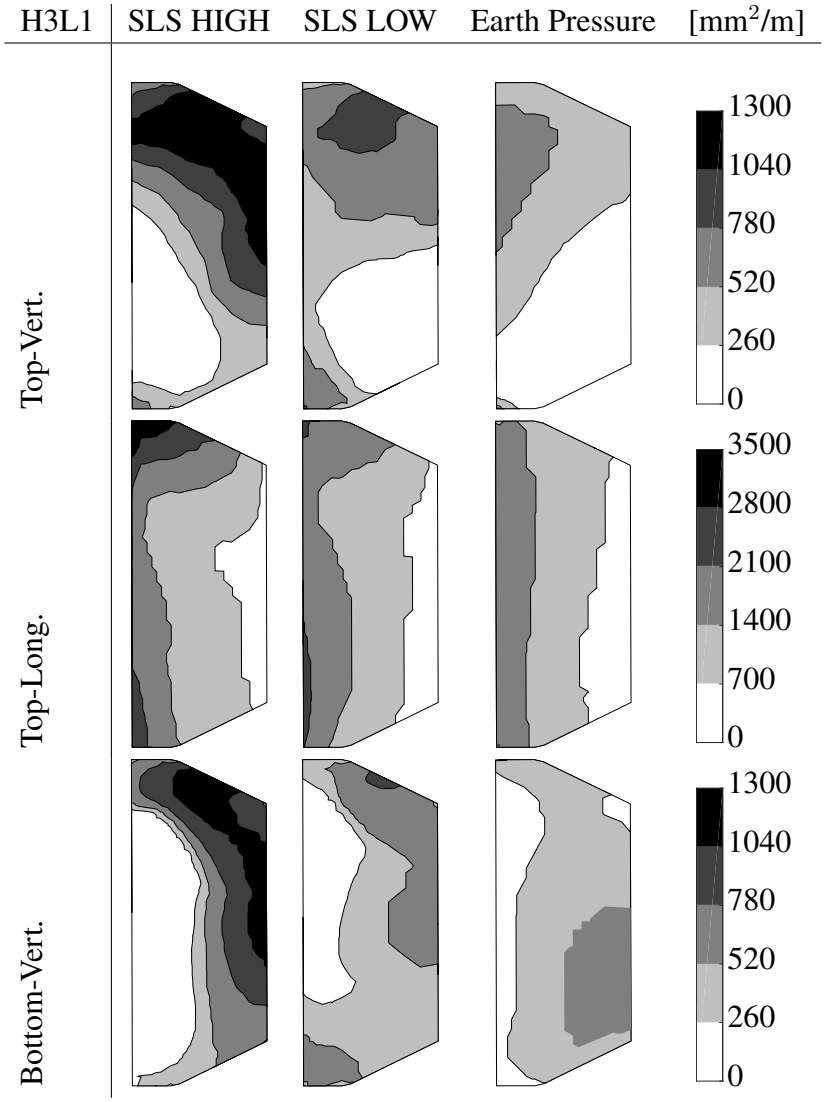

FIGURE D.5: Longitudinal and vertical reinforcement for top and bottom side of wing wall H3L1.

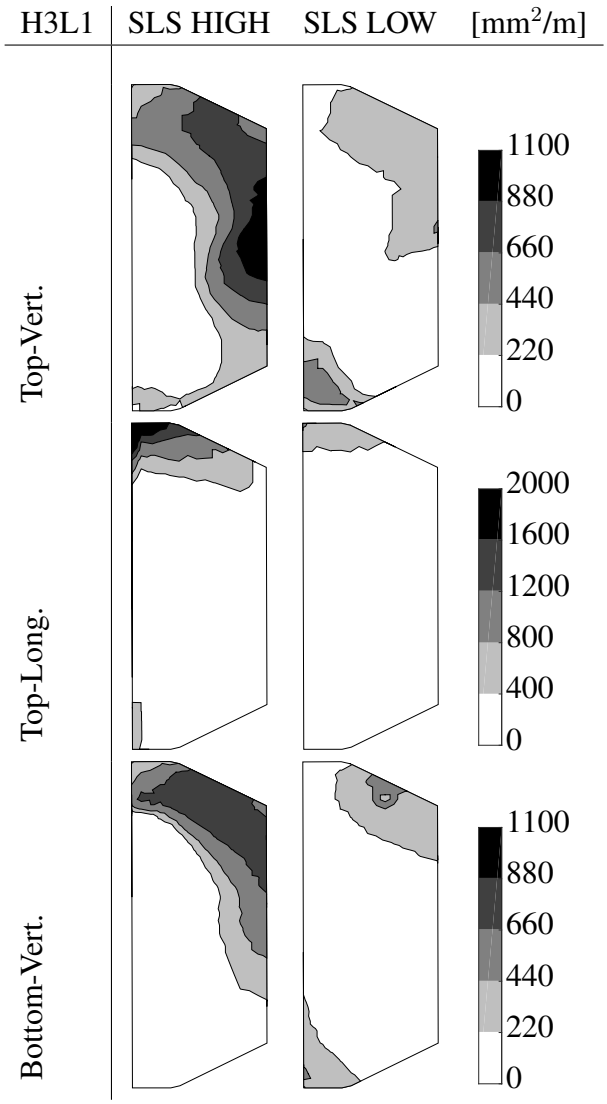

FIGURE D.6: Reinforcement caused by only membrane forces for H3L1.

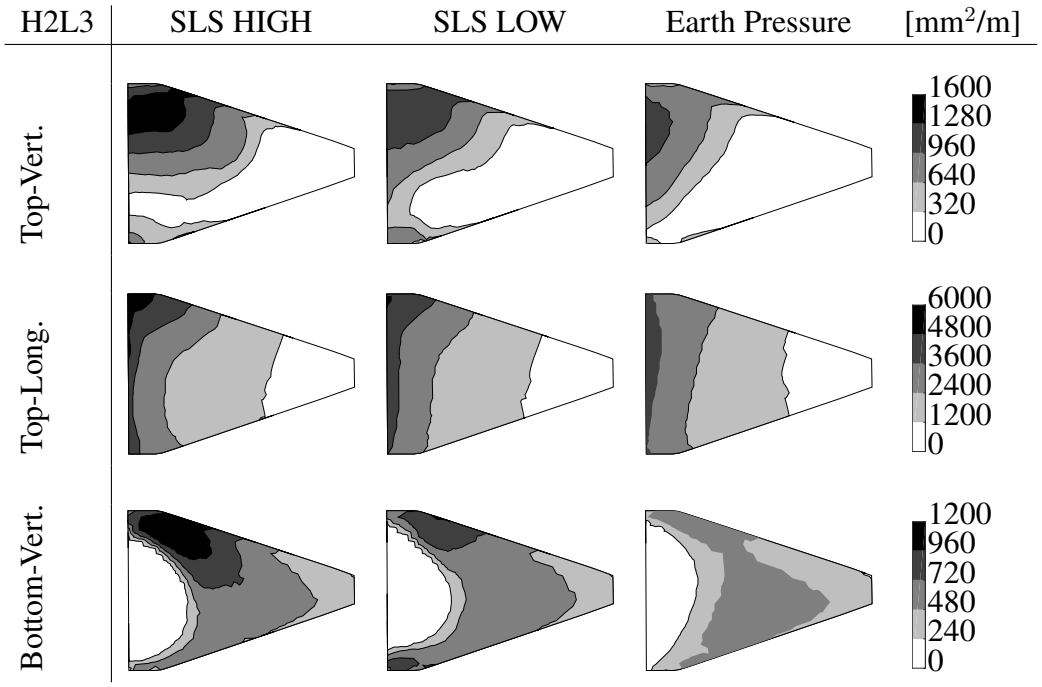

FIGURE D.7: Longitudinal and vertical reinforcement for top and bottom side of wing wall H2L3.

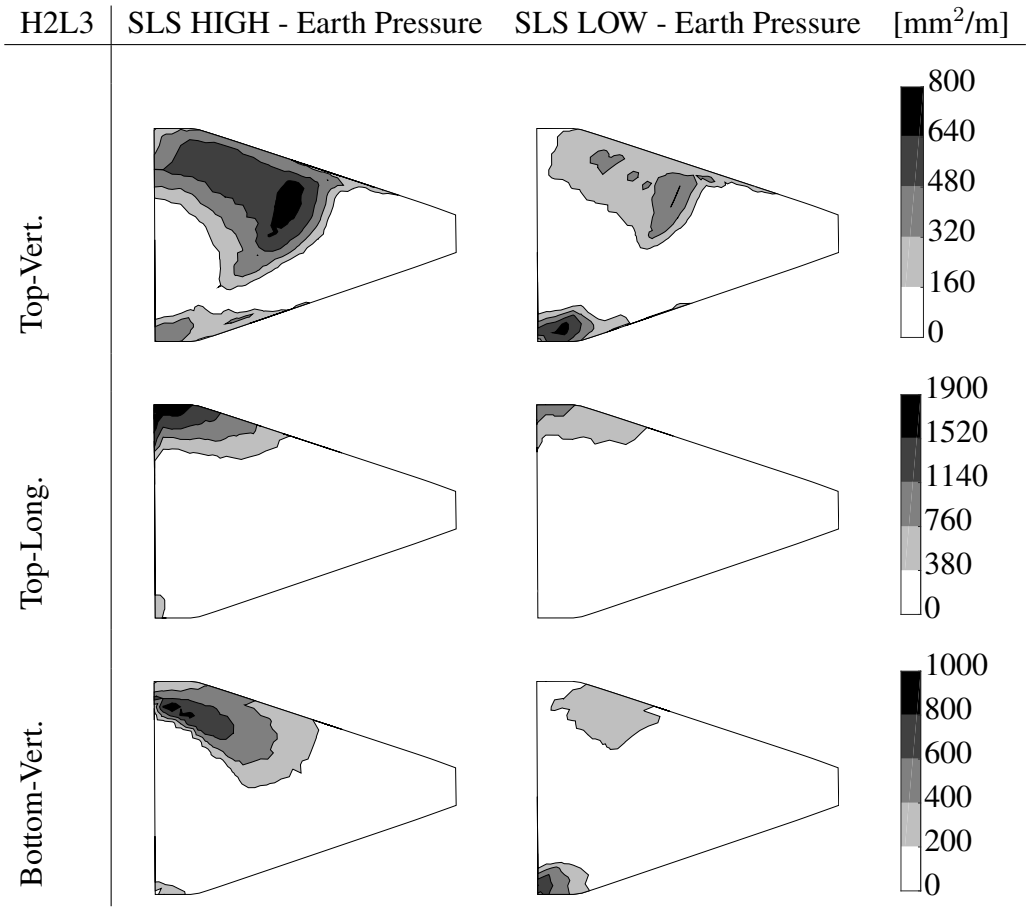

FIGURE D.8: Reinforcement caused by only membrane forces for H2L3.

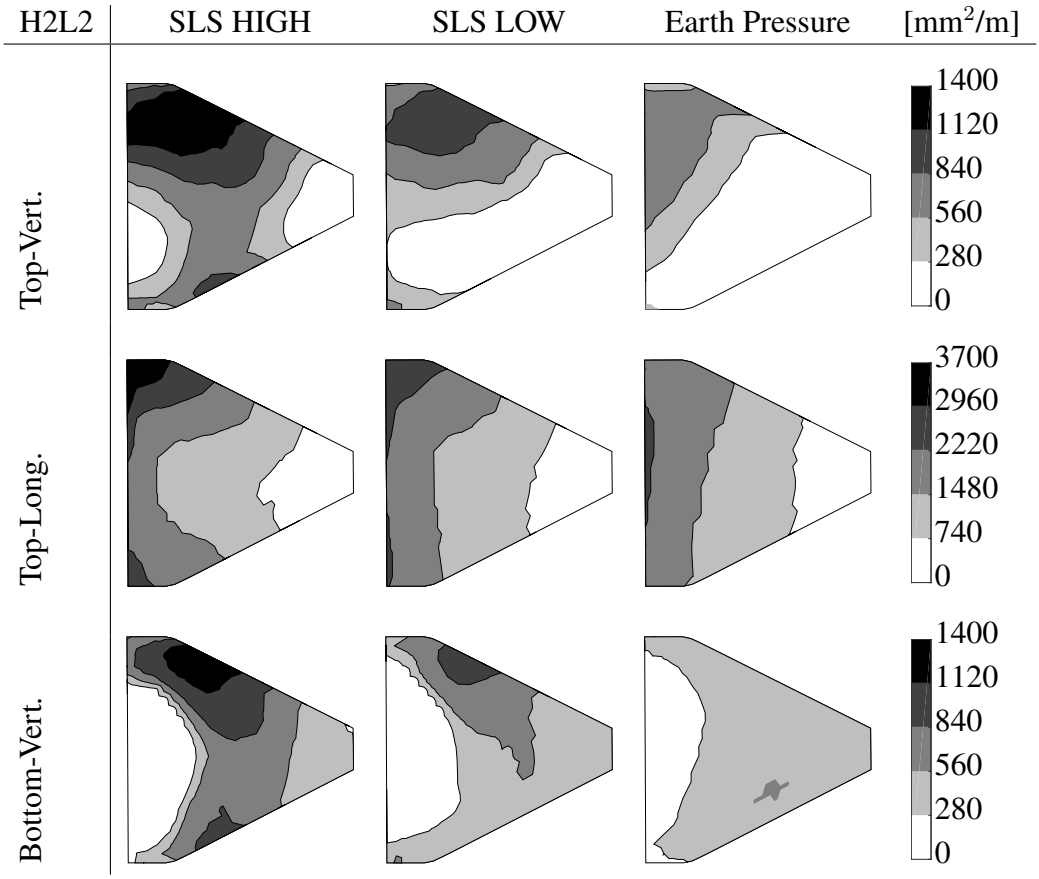

FIGURE D.9: Longitudinal and vertical reinforcement for top and bottom side of wing wall H2L2.

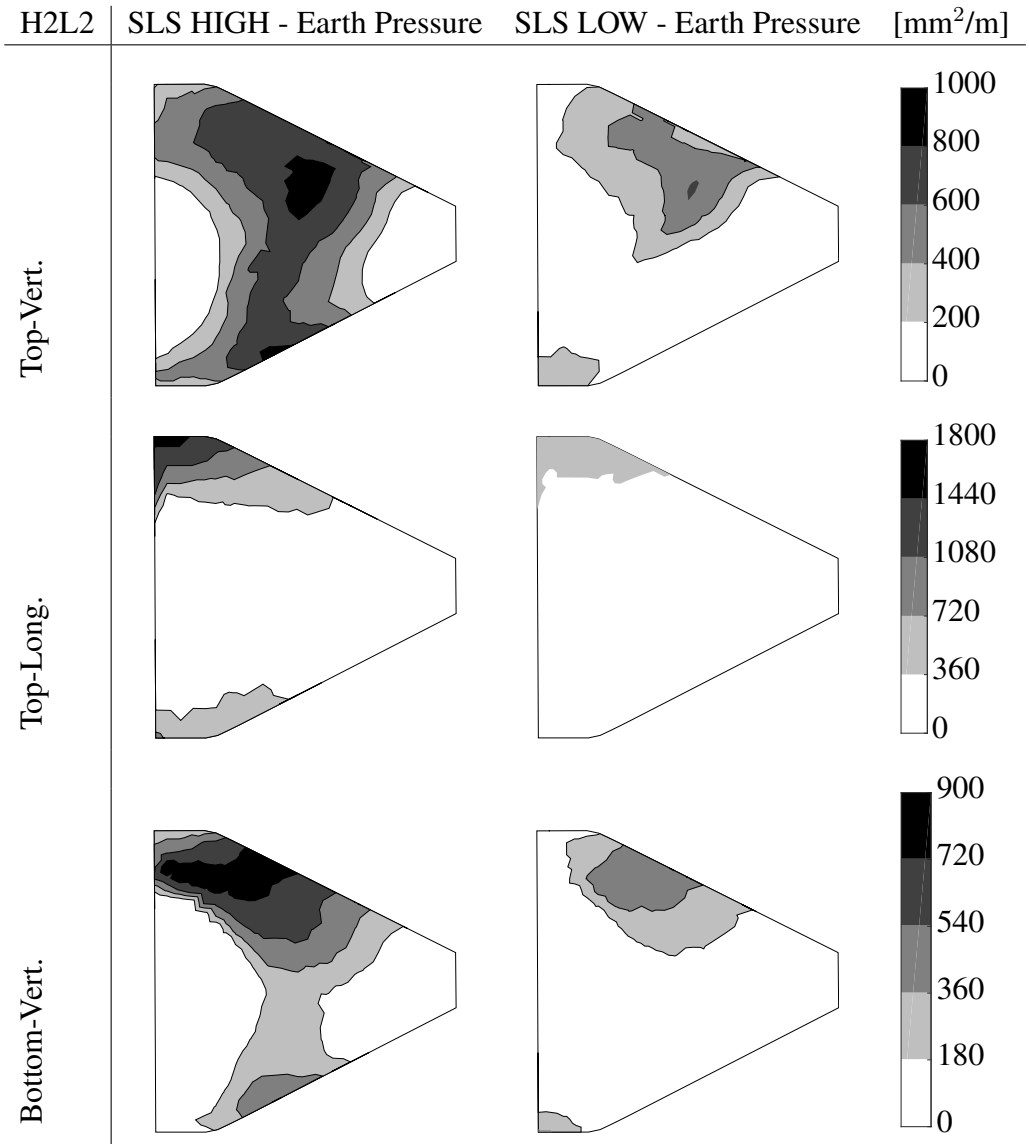

FIGURE D.10: Reinforcement caused by only membrane forces for H2L2.

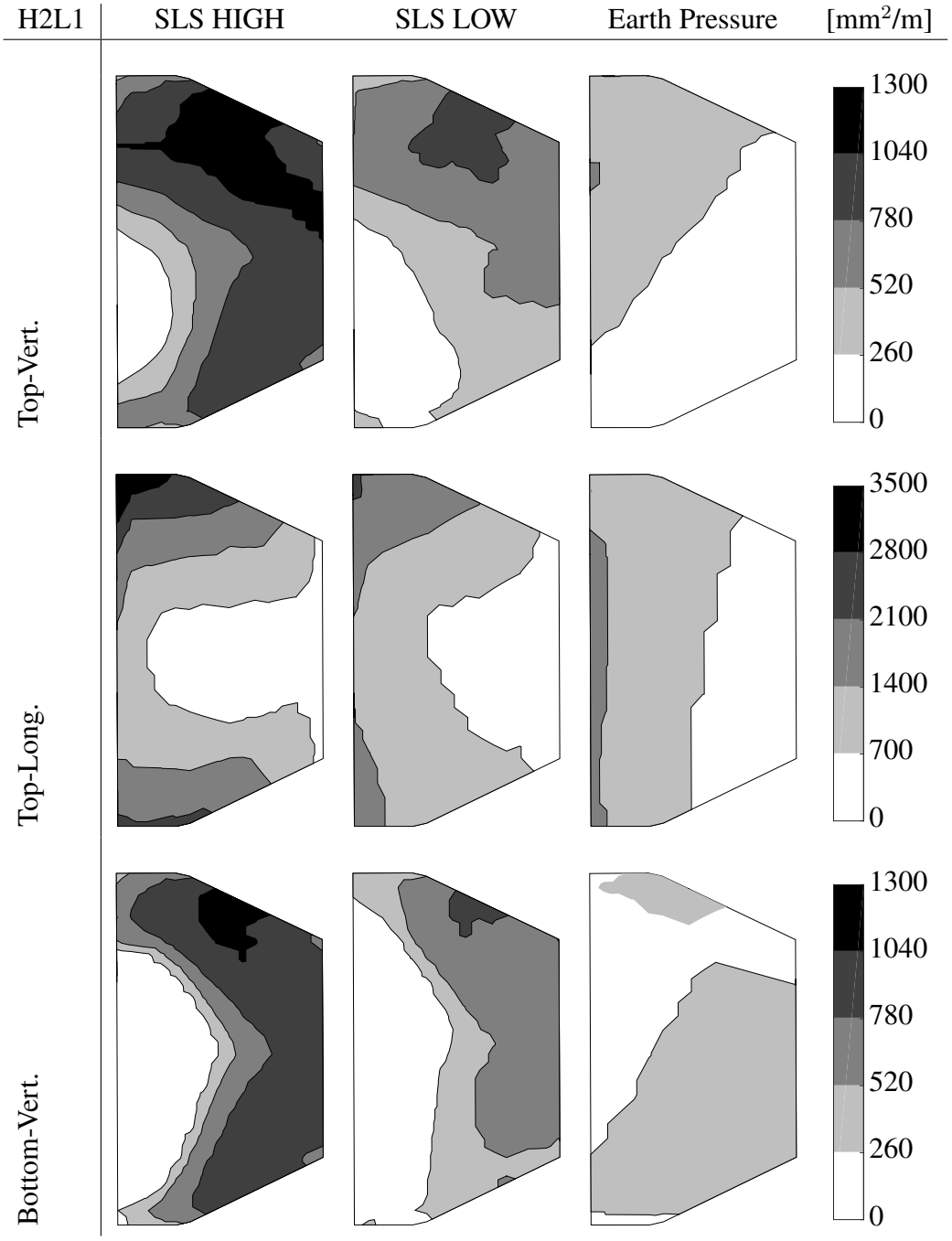

FIGURE D.11: Longitudinal and vertical reinforcement for top and bottom side of wing wall H2L1.

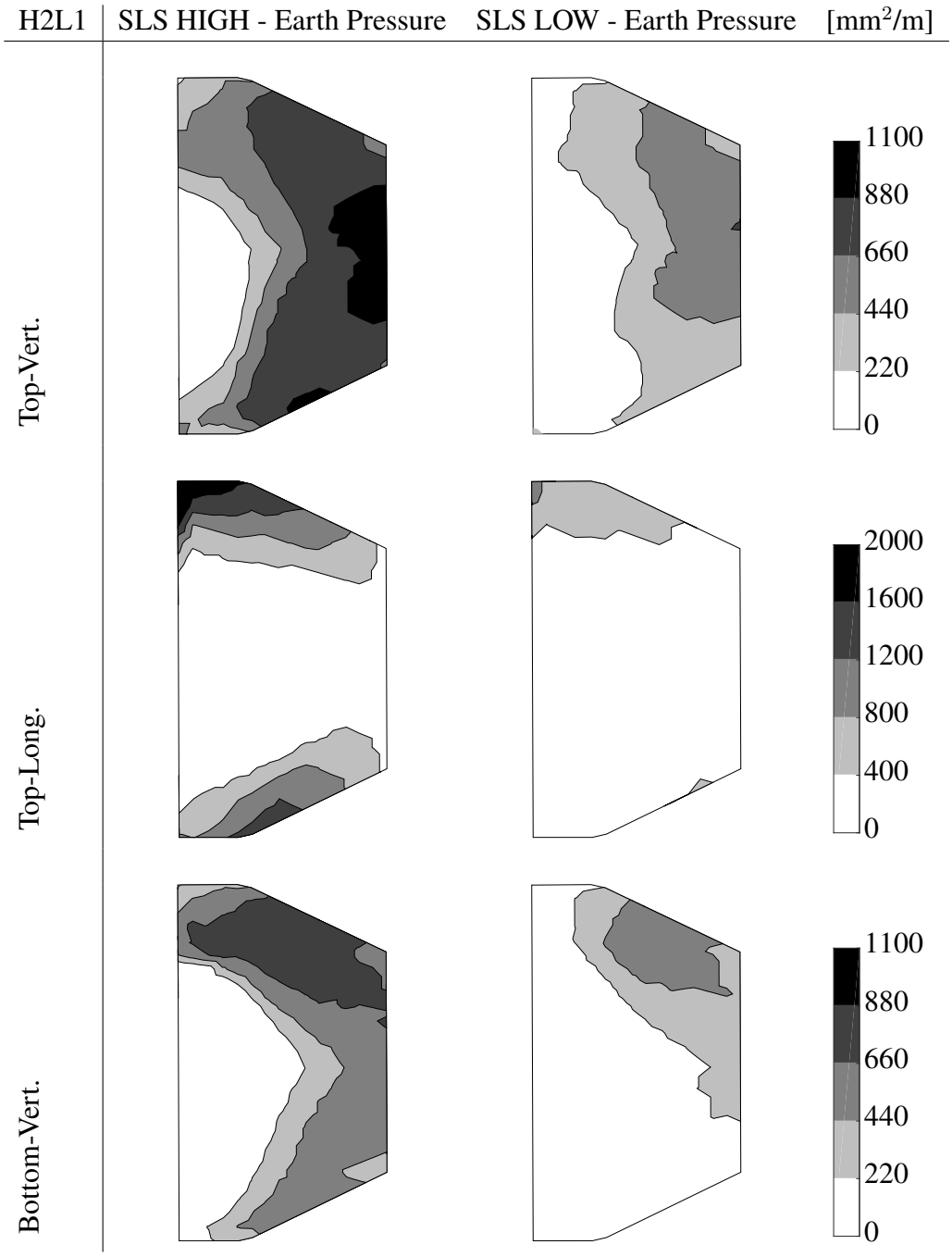

FIGURE D.12: Reinforcement caused by only membrane forces for H2L1.

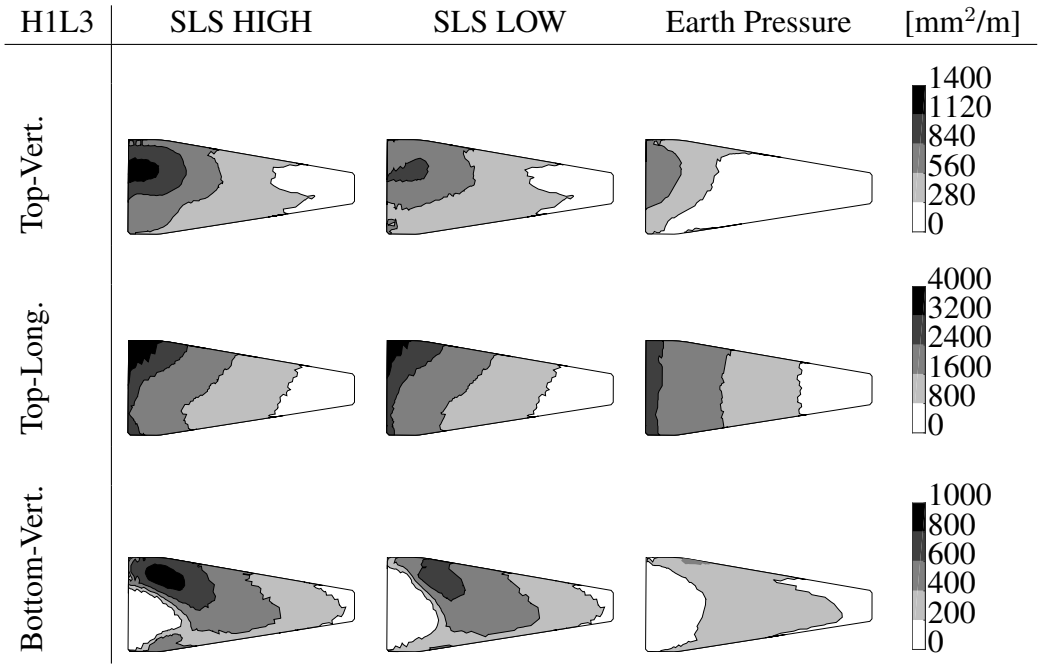

FIGURE D.13: Longitudinal and vertical reinforcement for top and bottom side of wing wall H1L3.

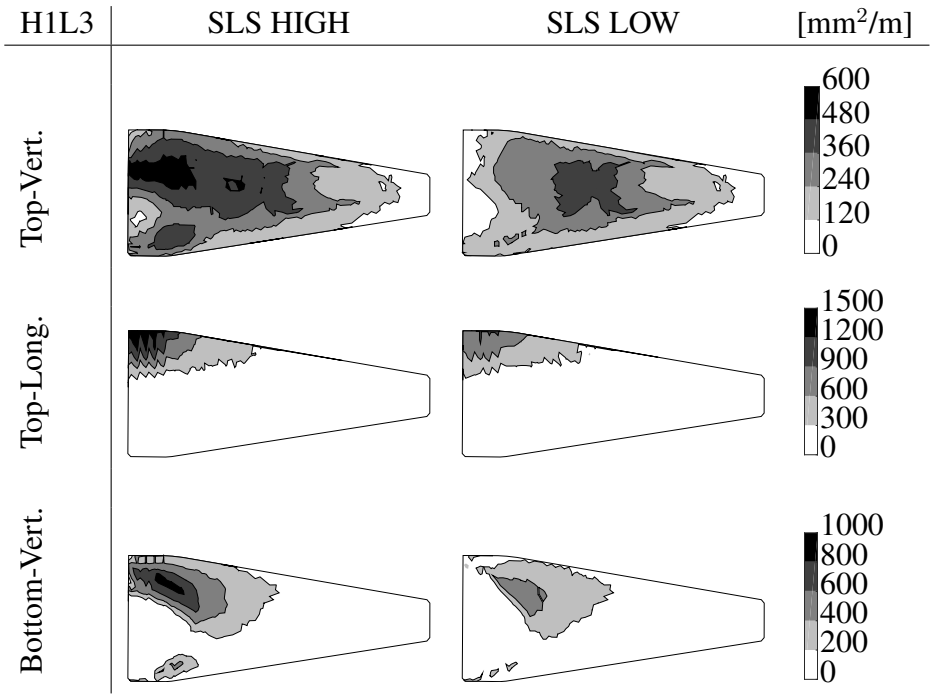

FIGURE D.14: Reinforcement caused by only membrane forces for H1L3.

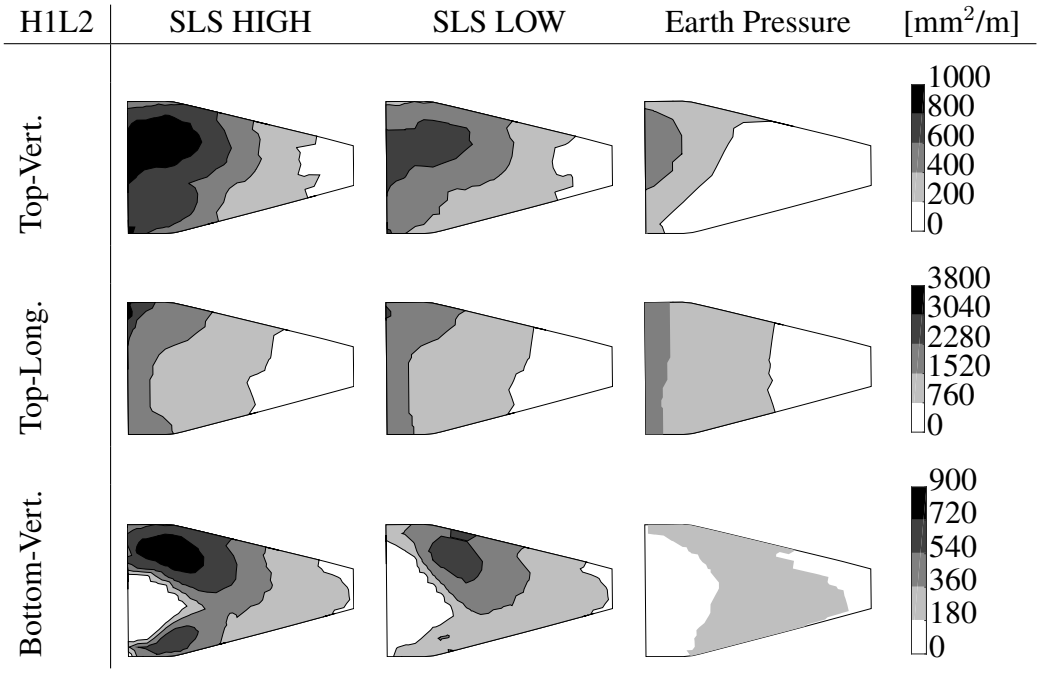

FIGURE D.15: Longitudinal and vertical reinforcement for top and bottom side of wing wall H1L2.

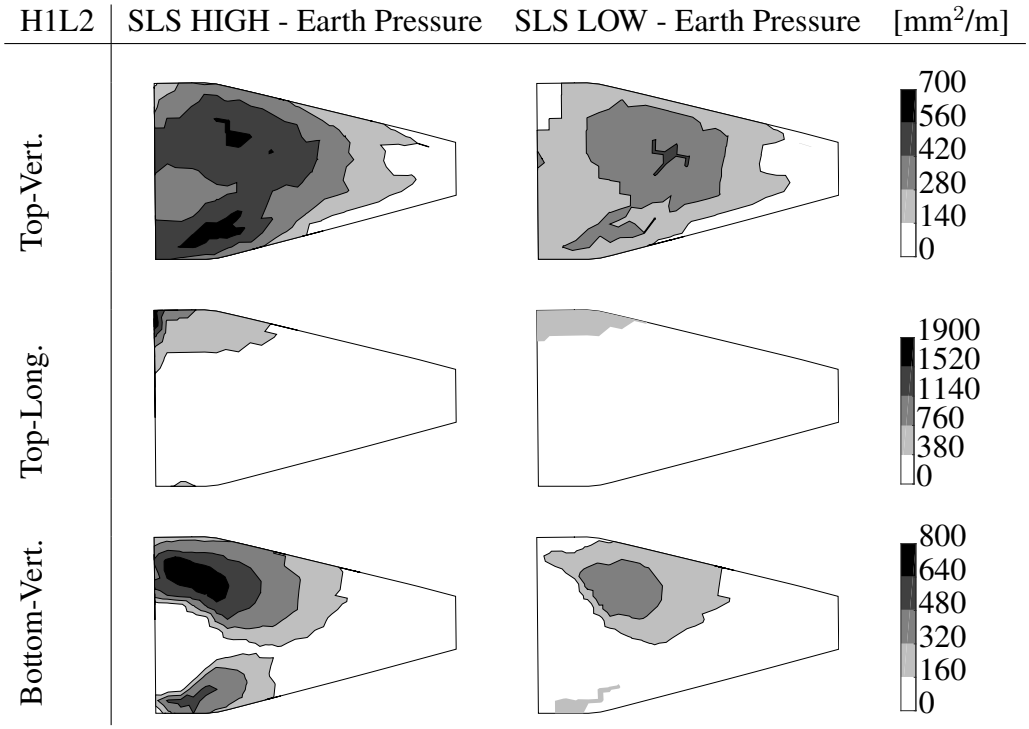

FIGURE D.16: Reinforcement caused by only membrane forces for H1L2.

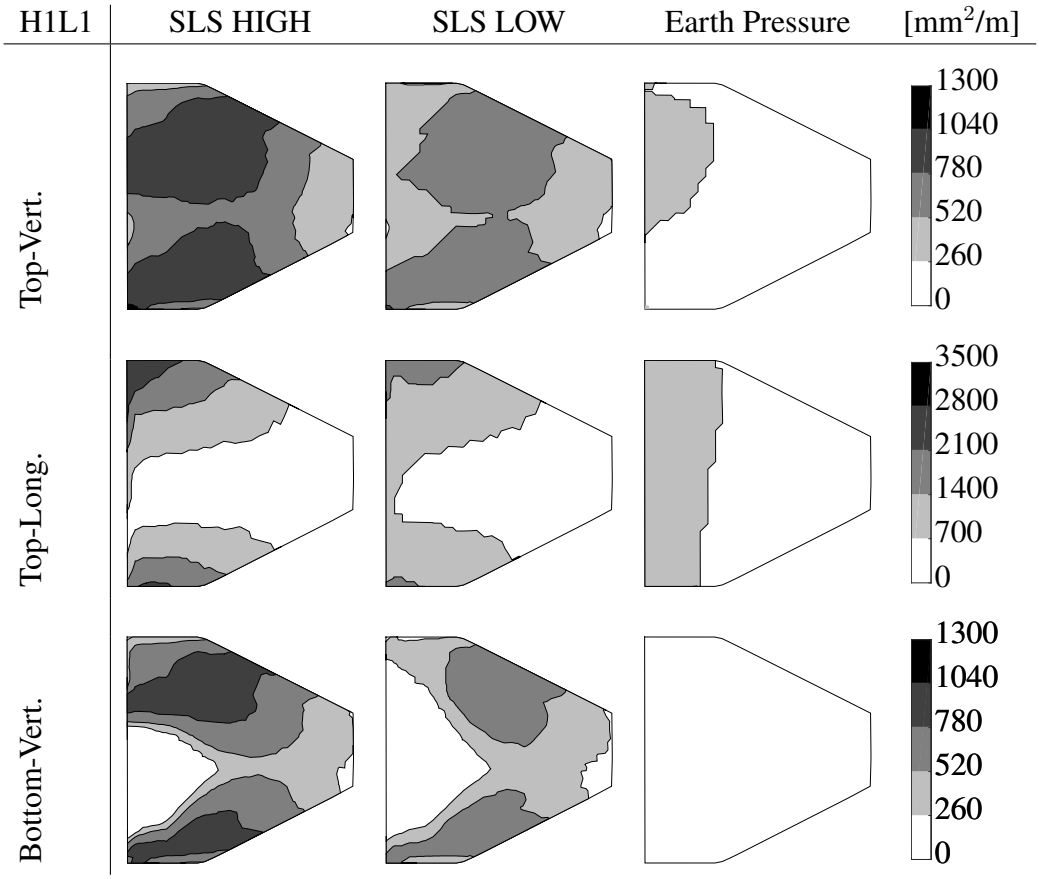

FIGURE D.17: Longitudinal and vertical reinforcement for top and bottom side of wing wall H1L1.

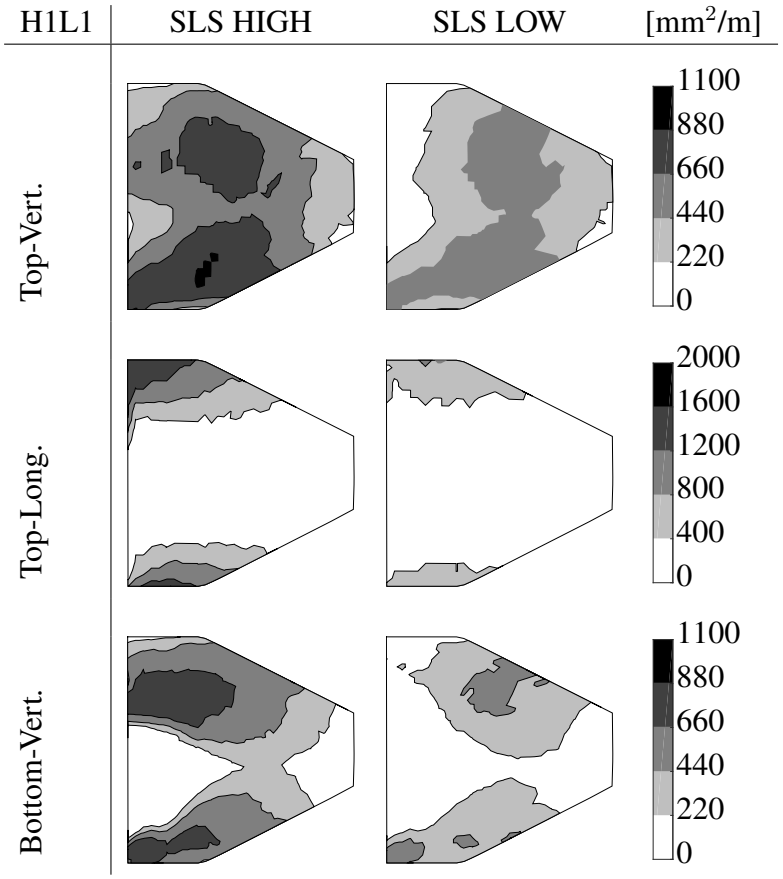

FIGURE D.18: Reinforcement caused by only membrane forces for H1L1.